ULTRAFAST PUMP PROBE SPECTROSCOPY OF SINGLE-WALL CARBON NANOTUBES

By

Zipeng Zhu

Dissertation

Submitted to the Faculty of the

Graduate School of Vanderbilt University

In partial fulfillment of the requirements

for the degree of

DOCTOR OF PHILOSOPHY

in

Physics

August, 2008

Nashville, Tennessee

Approved:

Professor Tobias Hertel

Professor Richard Haglund

Professor Charles Brau

Professor James Dickerson

Professor Eva Harth

To my parents, Linghao Zhu and Liangying Wu

ACKNOWLEDGEMENTS

I am grateful for the helps I have received from many people in this work. First I want to thank my committee members. It has been a privilege to work for my advisor Prof. Tobias Hertel, who has provided me, among numerous benefits, the opportunity to work on an advanced research object - carbon nanotube, with an advanced technology - ultrafast pump probe spectroscopy, both of which I have been very interested in; whose generosity provided me the opportunity to attend the 1st Workshop on Nanotube Optics and Nanospectroscopy (WONTON 2005) in Telluride Colorado, where besides enjoying the beautiful mountain scenery of Telluride, I had the opportunity to meet the most prestigious scientists in the research field and to listen and learn from their talks; who was always available and never hated to be interrupted when I needed his help in time of difficulty in the experiment, and whose patient explanations from fundamental optics to sophisticated theory on carbon nanotube photo physics helped me to grow from literarily knowing nothing in the field to being bold enough to insist on a new mechanism in the SWNT transient spectra that is completely different from the interpretations in most prior reports.

I also want to thank other committee members, Prof. Richard Haglund, Prof. Charles Brau, Prof. James Dickerson and Prof. Eva Harth, for their service on my committee, whose teaching and criticism as well as patient encouragement and clement understanding have helped to move this PhD program forward.

Secondly, I want to thank the colleagues and collaborations I have worked with in this program. I appreciate the help from a former postdoctor Hendrik Ulbricht in our

group, who patiently educated me on the basics of setting up an optical experiment. It has been a delight to work with a group member Jared Crochet, the discussion with whom frequently yields insightful and constructive ideas on the issues of my research topic. It has been a privilege to collaborate with Michael Arnold and his colleagues in Northwestern University, who provided the highly purified (6, 5) SWNT and the metallic SWNT samples which have been used in most experiments presented in this dissertation.

Thirdly, I want to thank my former advisor professor Lewis P. Fulcher and other professors in Bowling Green State University, where I did a masters' program that provided a solid foundation for this PhD program.

Last but not least, I want to thank all members in the Physics and Astronomy Department at Vanderbilt University, who provided a friendly and supportive atmosphere that made my challenging PhD study more enjoyable. I appreciate a VINSE (Vanderbilt Institute for Nanoscale Science and Engineering) fellowship I received from the department that substantially enhanced my study in the experimental condensed matter field. I am grateful for the financial support in the OPA (optical parametric amplifier) upgrading project by National Science Foundation (DMR0606505).

TABLE OF CONTENTS

Page

DEDICATION..... iii

ACKNOWLEDGEMENTS..... iv

LIST OF TABLES..... viii

LIST OF FIGURES……..... ix

Chapter

I. INTRODUCTION..... 1

II. PHYSICAL, ELECTRONIC STRUCTURE AND EXCITON THEORY OF SINGLE WALL CARBON NANOTUBES..... 6

2.1 Physical and electronic structure of graphene..... 7
2.2 Physical and electronic structure of SWNTs..... 12
2.3 Fundamentals of excitons in semiconductors…….. 21
2.4 Exciton states in SWNTs……. 26

III. EXPERIMENTAL SETUP AND AUTOMATION OF OPA (OPTICAL PARAMETRIC AMPLIFIER)..... 34

3.1 Configuration and operational principle of the ultrafast laser system…….. 35
3.2 Upgrading of OPA for automatic wavelength tuning..... 42
3.2.1 Principle of operation of OPA and method of automation……. 43
3.2.2 Implementation of the OPA automation……. 48
3.3 Setup and basic principle of the pump probe experiment……. 55
3.4 Sample preparation and characterization…….. 58

IV. ULTRAFAST SPECTROSCOPY OF (6, 5) SEMICONDUCTING SWNTS…. 63

4.1 Excited state dynamics of (6, 5) SWNTs in pump probe spectroscopy…... 65
4.1.1 Background…… 65
4.1.2 Pump power dependence…… 70
4.1.3 Pump wavelength dependence-pump probe excitation spectrum….. 72
4.1.4 Separation of excited state dynamics from ground state dynamics… 78
4.2 Transient spectra of (6, 5) SWNTs in pump probe spectroscopy…… 85
4.2.1 Background…… 85
4.2.2 Pump power and wavelength dependence……. 87
4.2.3 Spectral transients for resonant excitation of the E_{11} and E_{22} states... 90

4.2.4 Hypothesis for the origin of the photoinduced absorption: phonon assisted carrier scattering to the E_{ii} states…… 94
4.2.5 Variation of probe dynamics and transient spectrum narrowing effect…….. 99
4.2.6 Investigations on the photo bleach to photo induced absorption amplitude ratio…… 105

V. PRELIMINARY RESULTS ON THE ULTRAFAST SPECTROSCOPY OF METALLIC SWNTS……. 112

5.1 Metallic tube ultrafast spectroscopy…… 112
5.2 Coherent effect in pump probe signals…… 118

VI. SUMMARY…….. 120

CONCLUSION…… 123

LIST OF TABLES

Table		Page
2.1	Absorption spectra and Sommerfeld factor of semiconductors in a three dimensional system……	24
4.1	Summary of carrier dynamics in prior reports……	68
4.2	Summary of PA observations in prior reports……	86

LIST OF FIGURES

Figure		Page
2.1	Atomic orbitals in the calculation of graphene band structure.....	8
2.2	Illustration of the graphene band structure…….	12
2.3	Illustration of the formation of a (4, 2) SWNT from a graphene lattice…….	13
2.4	Classification and identification of SWNTs……...	14
2.5	Illustration of the band structure and density of states within the tight binding calculation……...	17
2.6	Derivation of SWNT band structure features from the conical energy dispersion relation…….	18
2.7	Schematic of a Wannier exciton and exciton states……	21
2.8	Comparison of the screening effect and the band edge absorption spectra with and without the Coulomb interaction in three, two and one dimensional systems……	25
2.9	Illustration of splitting of single particle excitations due to the electron-electron interaction……..	27
2.10	Illustration of the one and two photon allowed states in the two-photon excitation experiment…….	28
2.11	Dark exciton states with spin interactions……..	29
2.12	Schematic of exciton states in SWNTs……..	30
3.1	Schematic of the femtosecond laser system……..	35
3.2	Illustration of the mode locking principle……..	37
3.3	Ultrafast laser head in Vitesse……	38
3.4	Kerr lens effect……...	38
3.5	RegA optical schematic……..	39
3.6	Schematic of OPA and method of automation……...	43

3.7 Separation of light by a birefringent crystal……... 45

3.8 Momentum conservation in SHG and OPA crystals…….. 46

3.9 Actions of downhill simplex method……. 49

3.10 Algorithm with the downhill simplex method……... 50

3.11 Labview VI front panel of the automated OPA……. 52

3.12 Tuning curves with automated OPA…….. 53

3.13 Setup of the pump probe experiment…….. 55

3.14 Pump and probe technique……. 56

3.15 Absorption spectra of different fractions of the (6, 5) tube enriched sample…. 59

3.16 Comparison of absorption spectra of different SWNT samples……. 60

4.1 General procedure of pump probe measurements…….. 64

4.2 (A) Photoluminescence excitation- and (B) ground state absorption-spectra of a (6, 5) enriched nanotube suspension…… 66

4.3 (A) Linear absorption spectrum of a CoMoCAT @ SDBS sample. (B) Cross-correlations for resonant excitation of the E_{22} exciton in (6, 5) tubes at 572 nm……... 67

4.4 Pump power dependence of the E_{11} state relaxation of the (6, 5) tube…….. 70

4.5 Excitation spectroscopy of the (6, 5) SWNT across E_{22} resonance…… 73

4.6 Variation of the E_{11} relaxation with largely separated pump wavelengths…… 76

4.7 Extraction of the E_{11} state dynamics…….. 79

4.8 Tentative non-radiative relaxation scheme from E_{11} state……. 81

4.9 Illustration of the influence of exciton-phonon coupling to the carrier dynamic in SWNTs…….. 83

4.10 (A) False color plot of differential transmission signal as a function of pump -probe delay and probe wavelength of the (6, 5) tube in the E_{11} region for excitation of the E_{22} exciton. (B) Transient spectrum at 0.2 ps pump probe delay time ……..... 85

4.11 Pump power and pump wavelength dependence of transient spectrum in the E_{11} region of the (6, 5) tube…… 88

4.12 Spectra transients with the (1) E_{11} pump and (2) E_{22} pump……... 91

4.13 (A) PLE map of the SC dispersed sample. (B) Schematic of the mechanism of the PA in the transient spectra…… 95

4.14 Dynamics variation and transient spectrum narrowing effect in the E_{11} region. 99

4.15 (A-E) Wavelength dependence of the E_{11} transients after excitation of the E_{22} exciton. (B-E) Traces at wavelengths intermediate to those at the PB and PA extrema can be described by an incoherent superposition of PB and PA signals……. 101

4.16 Transient spectra can be decomposed into a superposition of a PB and PA Voigt profile…… 104

4.17 Investigation on PA/PB ratio…….. 106

5.1 Dynamics investigation of the metallic SWNT…….. 113

5.2 Spectra transients of the metallic SWNT sample……... 115

5.3 Interference from a coherent effect in the cross correlation signals……... 118

CHAPTER I

INTRODUCTION

A carbon nanotube is a layer of graphite lattice rolled into a seamless cylinder. The diameter of a carbon nanotube is on the order of one nanometer and the length of it can be several micrometers. Carbon nanotubes have many unique physical properties, they are much smaller in diameter than the most advanced semiconductor devices made so far; their tensile strength is about 20 times that of high- strength steel alloy; their electric current carrying capacity is estimated to be three orders of magnitude higher than that of copper; their heat transmission capacity is predicted about two times that of a nearly pure diamond; and they have a great resilience that they can be bent at large angles and re-straightened without damage. All these novel properties hold a great potential for future applications of carbon nanotubes [1].

The carbon nanotube is also a fascinating one dimensional object that is suited for studying the fundamental aspects of optical and electrical properties processed by low dimensional systems. The carbon nanotube has a unique association between its physical structure and its conductivity in that the twist of a carbon nanotube (chirality) determines whether it is metallic or semiconducting, and the band gap energy of semiconducting single wall carbon nanotubes (SWNTs) decreases as the diameter of the tube increases [2].

The booming of the carbon nanotube research field began in 1991, when Dr. Iijima made a historical observation of multi-wall carbon nanotubes with an electron

microscope at the NEC fundamental research laboratory in Japan [3]. Today this field has grown into a broad area where people from different countries and disciplines, with different experimental approaches, study many properties and applications of the carbon nanotube. This dissertation is focused on one of the experimental approaches to study the photo-physics of carbon nanotube and its exploration - ultrafast pump-probe spectroscopy.

Ultrafast spectroscopy is suited for investigation of fast processes, such as radiative or collision-induced decays of the excited levels, the relaxation of an optically pumped system towards thermal equilibrium etc., and it is an important approach to study in detail the dynamic properties of excited atoms and molecules [4]. By using ultrashort laser pulses, a high time resolution (~femtoseconds) can be achieved in pump-probe spectroscopy to facilitate a thorough knowledge of the dynamic processes, which is of fundamental importance for many branches of physics, chemistry or biology.

Although many experiments using ultrafast pump-probe spectroscopy have been carried out on SWNTs in the last five years, there are still quite some debates in the fundamental issues in the SWNT spectroscopy due to the complexity of the problem, among which the excited state dynamics and the photo induced absorption are two focuses lacking a thorough investigation and a satisfactory interpretation. Part of the debates may due to the difficulty to identify features from individual tube species in a transient spectrum made with polydisperse SWNT samples that have been used in most prior investigations.

Pump-probe spectroscopy of polydisperse nanotube suspensions and films has allowed to characterize intriguing properties of excited state dynamics in SWNTs [5-17].

However, difficulties with the overlap of photobleaching (PB) and photoabsorption (PA) signal components in spectrally congested samples remain, making the determination of the E_{11} exciton decay time and other components from pump-probe data difficult. Identification of the PA signal with specific tube types has likewise been complicated by the occurrence of such signals more or less throughout the entire range of transient spectra. Lastly, the long term behavior of optical transients appears to have been skewed by spectral congestion.

One advantage of our experiment is that we use chirality enriched SWNT samples. The investigation of spectral transients in the chirality enriched samples overcomes many problems of polydisperse samples and shed new light onto singlet and triplet exciton dynamics in carbon nanotubes [18]. Another advantage of our experiment is the pump-probe excitation spectroscopy, which provides much richer information on the excited state dynamics of SWNTs than the commonly performed degenerate pump-probe scheme on the bright exciton states of SWNTs.

The two advantages allow us to achieve new observations and to improve our understandings on the SWNT ultrafast spectroscopy. For the excited state dynamics, we achieve a better understanding of the contributions to the probe signal from the excited state population and the ground state population, and we attempt for the first time to extract the E_{11} state dynamics of the (6, 5) SWNT by subtracting the ground state dynamics from the E_{11} probe signal. For the origin of the PA, thanks to the purified chirality enriched SWNT samples used in our experiment, we are able to obtain a very interesting new observation of the similarity of the PA features in the transient spectra and the phonon sideband features in photoluminescence excitation (PLE) spectra, based

on which we propose a new mechanism for the origin of the PA-phonon assisted carrier scattering to the E_{ii} states in SWNTs. These new observations and analyses put insights into the light-carrier interaction mechanism in the quasi 1D SWNT material and provide valuable information for further investigations in this research field.

The rest of this dissertation is divided into five chapters. In chapter II, I introduce the physical and electronic structures and recent exciton theories of SWNTs, the information there provides a ground to understand the SWNT material and to interpret the observations in SWNT ultrafast spectroscopy presented in the later chapters. In chapter III, I introduce our pump-probe experiment setup and SWNT sample preparation procedure, in particular, I introduce the automation upgrading of the optical parametric amplifier (OPA), which is the key instrument used in our pump-probe experiment. In chapter IV, I present the results of a thorough investigation of the pump-probe spectroscopy of the (6, 5) SWNTs, and introduce our new interpretations for the excited state dynamics and the photo induced absorption. In chapter V, I present the first investigation of the pump-probe spectroscopy of a highly purified metallic SWNT sample. In the end in chapter VI, I provide a summary and a conclusion of the dissertation.

Reference:

[1] P. G. Collins and P. Avouris, Scientific American, December 2000, p62-69.
[2] R. Saito, G. Dresselhaus and M. S. Dresselhaus, *Physical Properties of Carbon Nanotubes*, Imperial College Press, London, 1998.
[3] S. Iijima, Nature, **354**, 56 (1991).
[4] W. Demtröder, *Laser Spectroscopy: Basic Concepts and Instrumentation*, 2nd Edition, Springer, 1996.
[5] M. Ichida, Y. Hamanaka, H. Kataura et al., Physica B **323**, 237 (2002).
[6] J. S. Lauret, C. Voison, G. Cassabois et al., Phys. Rev. Lett. **90**, 057404 (2003).
[7] G. N. Ostojic, S. Zaric, J. Kono et al., Phys. Rev. Lett. **92**, 117402 (2004).

[8] O. J. Korovyanko, C. X. Sheng, Z. V. Vardeny et al., Phys. Rev. Lett. **92**, 017403 (2004).
[9] D. J. Styers-Barnett, S. P. Ellison, C. Park et al., J. Phys. Chem. A **109**, 289 (2005).
[10] G. N. Ostojic, S. Zaric, J. Kono et al., Phys. Rev. Lett. **94**, 97401 (2005).
[11] Y. Z. Ma, L. Valkunas, S. L. Dexheimer et al., Phys. Rev. Lett. **94**, 157402 (2005).
[12] C. Manzoni, A. Gambetta, E. Menna et al., Phys. Rev. Lett. **94**, 270401 (2005).
[13] S. G. Chou, M. F. DeCamp, J. Jiang et al., Phys. Rev. B **72**, 159415 (2005).
[14] L. Valkunas, Y. Z. Ma, G. R. Fleming et al., Phys. Rev. B **73**, 115432 (2006).
[15] L. B. Huang and T. D. Krauss, Phys. Rev. Lett. **96**, 057407 (2006).
[16] L. Perfetti, T. Kampfrath, F. Schapper et al., Phys. Rev. Lett. **96**, 027401 (2006).
[17] H. Y. Seferyan, M. B. Nasr, V. Senekerimyan et al., Nano Lett. **6**, 1757 (2006).
[18] V. Perebeinos, J. Tersoff, and P. Avouris, Nano Lett. **5**, 2495 (2005).

CHAPTER II

PHYSICAL, ELECTRONIC STRUCTURE AND EXCITON THEORY OF SINGLE-WALL CARBON NANOTUBES

The physical and electronic structures of single-wall carbon nanotubes (SWNTs) are the key to understand the material and the foundation to interpret their behaviors in the ultrafast spectroscopy. The observation of the multi-wall carbon nanotubes by Dr. Sumio Iijima in 1991 marked the onset of the rapid growth of the carbon nanotubes research field [1]. The booming of this field is partially due to the intriguing unique physical properties of carbon nanotubes that should lead to many fantastic applications in the future [2, 3]; partially due to the excellent one-dimensional object they represent that is ideal for studying fundamental sciences in a low-dimensional system. The research and theory on carbon nanotubes have grown so broad and profound during the last 15 years that only a glimpse can be reviewed in a short chapter like this one. Therefore, I will focus on some of the most fundamental and accepted theories of SWNTs that are closely relevant to the experimental results presented in later chapters.

In the first section of this chapter, I will discuss the atomic and electronic structure of graphene with a calculation in the tight binding approximation. Due to the close relationship between the geometric and electronic structure of graphene and SWNTs, the understanding of graphene electronic structure is helpful for the understanding of the electronic structure of SWNTs, which is the focus of the second section of this chapter. Experimental and theoretical investigations in recent years suggest that the dominant features in the SWNT optical spectra are of excitonic nature. In the third section, I will

briefly introduce the general exciton theories with the focuses on the exciton binding energy and the Coulomb interaction effects on the band edge absorption spectrum. This discussion leads naturally to the more specific exciton theories of SWNTs in the fourth section, where I provide a brief review of the evolution of the SWNT exciton theory over the last a few years with an emphasis on the most current theories.

2.1 Physical and electronic structure of graphene

In this section I review simple band structure calculations of the band structure of graphene (a layer of graphite). Carbon nanotubes are considered as excellent 1D material because of their extremely small diameters. Graphene is considered as the thinnest 2D material in the world and it is also stimulating researchers' inspirations for its electronics applications [4]. The band structure of covalently bound solids is frequently calculated using the tight-binding approximation (TBA) which is based on the linear combination of atomic orbitals (LCAO) [5]. In the following this method will be used for illustrative purposes to calculate a simplified band structure of graphene. The notations in the calculation will mostly follow those in reference [5]. There are mainly five steps in this calculation: 1, decide atomic wave functions that enter the calculation. 2, construct Bloch states as the basis for the expansion of the crystal wave functions. 3, expand single particle eigenstates in the Bloch basis. 4, write down the secular equation and calculate the Hamiltonian matrix elements. 5, solve the secular equation to obtain the band structure.

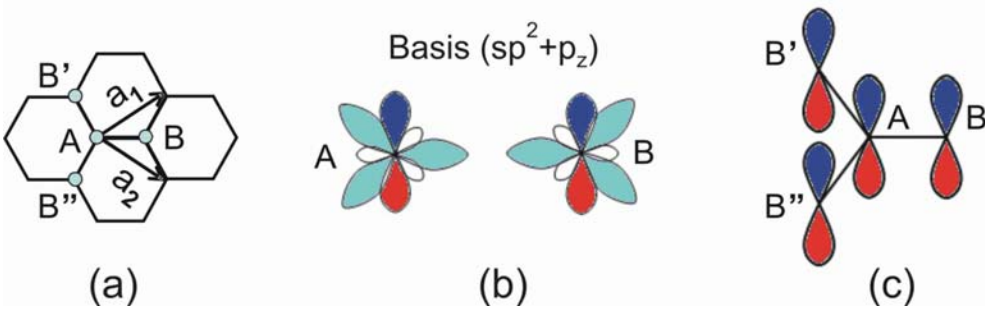

Figure 2.1 Atomic orbitals in the calculation of graphene band structure. (a) A piece of graphene lattice. Atoms B, B' and B" are the nearest neighbors of atom A. a_1 and a_2 are the unit vectors. (b) The orientation of atomic orbitals in the basis atoms A and B. (c) Four p_z orbitals which are considered in the calculation.

Let us start with selecting the appropriate atomic wave functions. Figure 2.1 (a) shows a section of a graphene lattice, the basis of which has two carbon atoms A and B. Atom A has three nearest neighbors, B, B' and B". In the spirit of the TBA, we only consider the interactions with the nearest neighbors. Each carbon atom has four electrons in the outer shell that form three sp^2 hybridized orbitals and one p_z orbital. Figure 2.1 (b) shows the orientation of the orbitals in the basis atoms. The lobes of the sp^2 orbitals lie within the graphene plane and the lobes of the p_z orbitals are oriented perpendicular to the plane. The bands formed by the weakly bound p_z orbitals are closest to the Fermi level and necessary in this calculation. Figure 2.1 (c) shows all the orbitals we need to consider in the calculation, which include p_z orbitals of atom A and its three nearest neighbors. We denote these orbitals with $\phi_{p_z}(r-t_i)$, where t_i designates the position of atom A or B within the primitive unit cell (see figure 2.2(A)).

Step 2 is to construct Bloch states that can be used as the basis for the expansion of the crystal wave function $\chi_{kp_zi}(r)$. The summation runs over all N unit cells in the lattice (the vector R').

$$\chi_{kp_z i}(r) = \frac{1}{\sqrt{N}} \sum_{R'} e^{ik\cdot R'} \phi_{p_z}(r - t_i - R'), \tag{2.1}$$

Step 3, we expand the crystal single particle eigenstates in the above Bloch state basis,

$$\psi_k(r) = \sum_i c_{kp_z i} \chi_{kp_z i}(r), \tag{2.2}$$

where $c_{kp_z i}$ is the coefficient.

Step 4, we write down the secular equation and calculate the on-site and hopping matrix elements. Assume $\psi_k(r)$ is the solution to a single particle equation,

$$H^{sp}\psi_k(r) = \varepsilon_k \psi_k(r) \Rightarrow \sum_i \left[\left\langle \chi_{kp_z j} \middle| H^{sp} \middle| \chi_{kp_z i} \right\rangle - \varepsilon_k \left\langle \chi_{kp_z j} \middle| \chi_{kp_z i} \right\rangle \right] c_{kp_z i} = 0. \tag{2.3}$$

The second expression in the above equation is called the secular equation. The second integral in the secular equation is calculated as,

$$\begin{aligned} \left\langle \chi_{kp_z j} \middle| \chi_{kp_z i} \right\rangle &= \frac{1}{N} \sum_{R',R''} e^{ik\cdot(R'-R'')} \left\langle \phi_{p_z}(r - t_j - R'') \middle| \phi_{p_z}(r - t_i - R') \right\rangle \\ &= \frac{1}{N} \sum_{R',R} e^{ik\cdot R} \left\langle \phi_{p_z}(r - t_j) \middle| \phi_{p_z}(r - t_i - R) \right\rangle \\ &= \sum_R e^{ik\cdot R} \left\langle \phi_{p_z}(r - t_j) \middle| \phi_{p_z}(r - t_i - R) \right\rangle \end{aligned} \tag{2.4}$$

The bracket in the last expression in equation 2.4 is called the overlap matrix elements. The first integral in the secular equation is calculated as,

$$\left\langle \chi_{kp_z j} \middle| H^{sp} \middle| \chi_{kp_z i} \right\rangle = \sum_R e^{ik\cdot R} \left\langle \phi_{p_z}(r - t_j) \middle| H^{sp} \middle| \phi_{p_z}(r - t_i - R) \right\rangle \tag{2.5}$$

The bracket on the right side of this equation is called the Hamiltonian matrix elements. According to the formalism of TBA "orthogonal basis", the overlap matrix elements are non-zero only for the same orbitals on the same atom, namely,

$$\left\langle \phi_{p_z}(r - t_j) \middle| \phi_{p_z}(r - t_i - R) \right\rangle = \delta_{ij}\delta(R) \tag{2.6}$$

The Hamiltonian matrix elements are non-zero if the orbitals are on the same atom, namely,

$$\left\langle \phi_{p_z}(r-t_j)\middle|H^{sp}\middle|\phi_{p_z}(r-t_i-R)\right\rangle = \delta_{ij}\delta(R)\varepsilon_0 \tag{2.7}$$

Where ε_0 is called the on-site energy; or if the orbitals are on different atoms but situated at nearest neighbor sites, denoted as d_{nn} in general,

$$\left\langle \phi_{p_z}(r-t_j)\middle|H^{sp}\middle|\phi_{p_z}(r-t_i-R)\right\rangle = \delta((t_j-t_i-R)-d_{nn})t_{ij} \tag{2.8}$$

where t_{ij} are called hopping matrix elements. In figure 2.1 (a),

$$a_1 = \frac{\sqrt{3}a}{2}\hat{x} + \frac{a}{2}\hat{y}; \qquad a_2 = \frac{\sqrt{3}a}{2}\hat{x} - \frac{a}{2}\hat{y}; \qquad A(0,0); B(\frac{a}{\sqrt{3}},0) \tag{2.9}$$

where a is the length of the vector a_1 and a_2. The hopping matrix element can be calculated as,

$$\begin{aligned}
&\left\langle \phi_{p_z}(r-t_j)\middle|H^{sp}\middle|\phi_{p_z}(r-t_i-R)\right\rangle = \left\langle \phi^A_{p_z}(r)\middle|H^{sp}\middle|\phi^B_{p_z}(r-\frac{a}{\sqrt{3}}\hat{x})\right\rangle \\
&+\left\langle \phi^A_{p_z}(r)\middle|H^{sp}\middle|\phi^{B'}_{p_z}(r+a_2)\right\rangle \exp(-ik\cdot a_2) + \left\langle \phi^A_{p_z}(r)\middle|H^{sp}\middle|\phi^{B''}_{p_z}(r+a_1)\right\rangle \exp(-ik\cdot a_1) \\
&= t\left[1+\exp(-i(k_x\hat{x}+k_y\hat{y})\cdot(\frac{\sqrt{3}a}{2}\hat{x}+\frac{a}{2}\hat{y})) + \exp(-i(k_x\hat{x}+k_y\hat{y})\cdot(\frac{\sqrt{3}a}{2}\hat{x}-\frac{a}{2}\hat{y}))\right] \\
&= t\left[1+e^{-i\left(\frac{\sqrt{3}}{2}k_xa+\frac{1}{2}k_ya\right)} + e^{-i\left(\frac{\sqrt{3}}{2}k_xa-\frac{1}{2}k_ya\right)}\right]
\end{aligned} \tag{2.10}$$

Step 5, we use the results in equation 2.7 and 2.10 to solve the secular equation

$$\begin{vmatrix} \varepsilon_0-\varepsilon_k & t\left[1+e^{i\left(\frac{\sqrt{3}}{2}k_xa+\frac{1}{2}k_ya\right)} + e^{i\left(\frac{\sqrt{3}}{2}k_xa-\frac{1}{2}k_ya\right)}\right] \\ t\left[1+e^{-i\left(\frac{\sqrt{3}}{2}k_xa+\frac{1}{2}k_ya\right)} + e^{-i\left(\frac{\sqrt{3}}{2}k_xa-\frac{1}{2}k_ya\right)}\right] & \varepsilon_0-\varepsilon_k \end{vmatrix}$$

$$= \begin{vmatrix} \varepsilon_0 - \varepsilon_k & t\left[1 + 2e^{i\frac{\sqrt{3}}{2}k_x a}\cos\left(\frac{k_y a}{2}\right)\right] \\ t\left[1 + 2e^{-i\frac{\sqrt{3}}{2}k_x a}\cos\left(\frac{k_y a}{2}\right)\right] & \varepsilon_0 - \varepsilon_k \end{vmatrix} = 0$$

The solution of the above equation gives,

$$\varepsilon_k^{(\pm)} = \varepsilon_0 \pm t\left[1 + 4\cos\left(\frac{\sqrt{3}a}{2}k_x\right)\cos\left(\frac{a}{2}k_y\right) + 4\cos^2\left(\frac{a}{2}k_y\right)\right]^{1/2} \tag{2.11}$$

Equation 2.11 is a simple approximation of the graphene band structure. A band structure that is closer to reality is given as

$$E_{g2D}(\vec{k}) = \frac{\varepsilon_0 \pm tw(\vec{k})}{1 \pm sw(\vec{k})}, \tag{2.12}$$

Where s is the overlap integral between the nearest A and B atoms, and

$$w(\vec{k}) = \left[1 + 4\cos\left(\frac{\sqrt{3}a}{2}k_x\right)\cos\left(\frac{a}{2}k_y\right) + 4\cos^2\left(\frac{a}{2}k_y\right)\right]^{1/2}.$$

In principle, the value of Hamiltonian matrix elements ε_0 and t can be calculated by using the single particle Hamiltonians. However, the corresponding single particle states in solids are more compressed due to the presence of nearby electrons [5], this calculation may not be close to reality. Alternatively, one can guess the values of Hamiltonian matrix elements so that they reproduce important features of band structure, which can be testified with experiments.

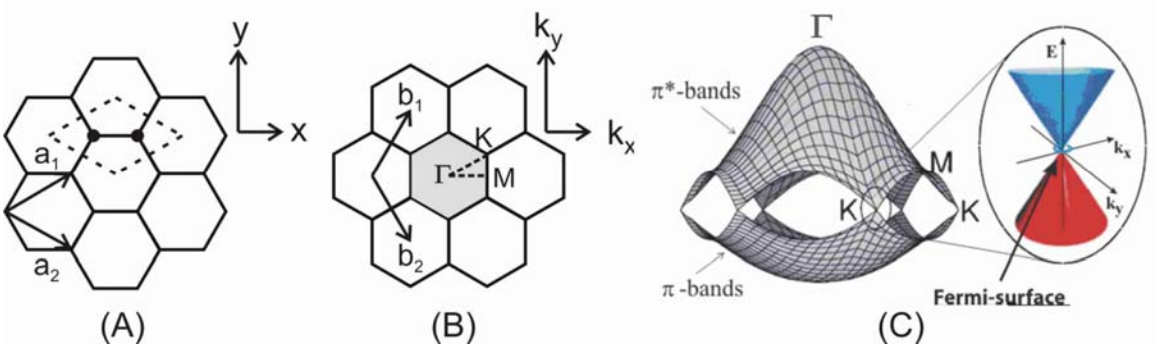

Figure 2.2 Illustration of the graphene band structure. (A) Graphene lattice and its unit cell (dashed rhombus). (B) The Brillouin zones and high symmetry points of graphene. (C) Energy dispersion relations of graphene in the first Brillouin zone.

Figure 2.2 shows the results of the graphene band structure calculation. Figure 2.2 (A) shows the graphene lattice in the real space. The dashed rhombus illustrates the unit cell inside which the two dots represent the basis atoms. Figure 2.2 (B) shows the Brillouin zones in the reciprocal space with the first Brillouin zone shaded. b_1 and b_2 are unit vectors in the reciprocal space. Γ, K, and M are the high symmetry points in the Brillouin zone. Figure 2.2 (C) shows the energy dispersion relation of equation 2.12 in the first Brillouin zone. The π^* bands above Fermi level correspond to the - sign in equation 2.12, and the π bands below Fermi level correspond to the + sign. Two bands connect at K points so that graphene is a zero band gap material. The enlargement shows the conical dispersion relation near the K point.

2.2 Physical and electronic structures of SWNTs

In this section we first discuss the geometrical structure of SWNTs, and then derive the electronic structure of SWNTs from the graphene band structure by a process referred to as zone folding.

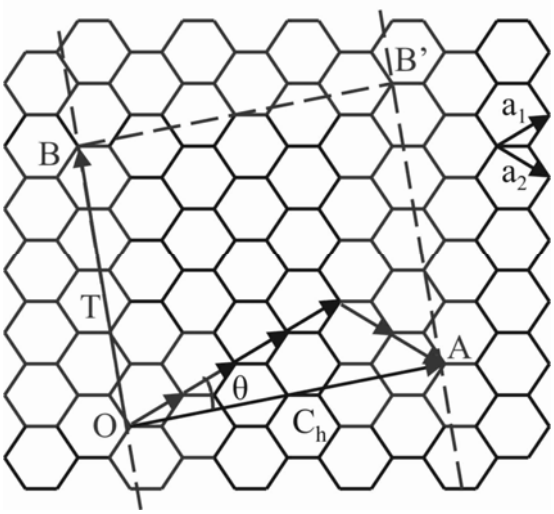

Figure 2.3 Illustration of the formation of a (4, 2) SWNT from a graphene lattice.

Figure 2.3 illustrates the formation of a SWNT species called the (4, 2) tube. If we cut a slice of the graphene sheet along OB and AB' shown in figure 2.3, and then roll it over so that point O (or atom O) overlaps with atom A, and atom B overlaps with B', we obtain a cylindrical roll which is essentially a SWNT. We use a vector C_h(OA) called chiral vector to label this tube. This chiral vector is the sum of four a_1 unit vectors and two a_2 unit vectors of the graphene lattice, we therefore write it as C_h=(4, 2) and name this SWNT (4, 2) tube. The chiral vector has the length of the tube circumference and is perpendicular to the tube axis. The vector T(OB) is called the translational vector, which points along the direction of the tube axis. The rectangle OAB'B gives the outline of the unit cell of this SWNT. The angle θ is called the chiral angle of the SWNT.

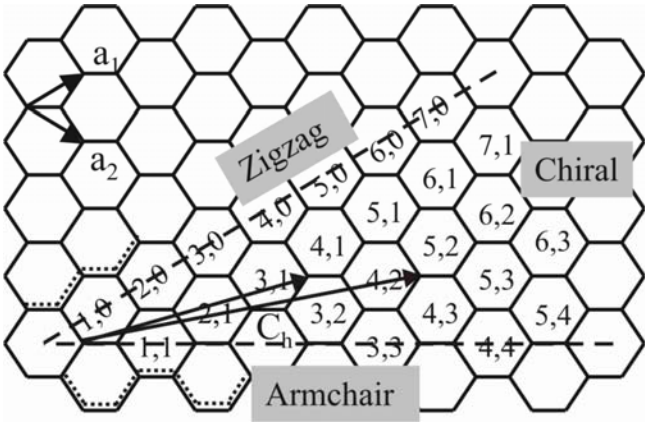

Figure 2.4 Classification and identification of SWNTs.

We obtain different SWNTs if we cut a slice of graphene with different widths or roll it along different directions. In figure 2.4, the chiral vectors of a (4, 2) tube and a (3, 1) tube are shown. The indices in the hexagons show the tube types that will be formed if rolled over to those hexagons. SWNTs are classified into three groups based on their physical structures: 1) The tubes with a chiral vector C_h=(n, 0), where n is an integer, are called zigzag tubes. The chiral angle of the zigzag tubes is 0. As can be seen in figure 2.4, carbon atoms form a zigzag chain (illustrated by a dotted line) along the circumference of the (n, 0) tube family. 2) The tubes with a chiral vector C_h=(n, n) and a chiral angle of $\pi/6$ are called armchair tubes. Carbon atoms along the circumference direction form an armchair shape in the (n, n) tubes. 3) The tubes with the chiral angles between 0 to $\pi/6$ are called chiral tubes.

To derive the SWNT band structure, we calculate the band structure of the stripe of graphene that has the length of a SWNT and the width of the tube circumference, by applying a periodic boundary condition in the circumference direction. This implies that the curvature effect of the SWNT is not considered. The TBA calculation with the consideration of the s electrons [6] and the local density approximation calculation [7, 8]

suggest that the large curvature of the small diameter tubes leads to a hybridization of the π* and σ* orbitals, which causes a small energy gap (on the order of meV). However, the effect of the hybridization is not so great for the large diameter tubes (>0.7nm) [9]. The major tube species investigated in this dissertation have a diameter around 0.8 nm and therefore for simplicity we will neglect the curvature effect in the calculation. The aim of this exercise is not to determine the accurate energy levels of the bands, but to demonstrate the intrinsic connection between the band structures of graphene and SWNTs and to facilitate the understanding of the SWNT band structure by deriving it from the graphene band structure. The underlying physics of the derivation is an important concept in nano-science: the confinement in the real space leads to the energy quantization in the reciprocal space.

The basic idea of the calculation is to replace the graphene reciprocal unit vectors in equation 2.12 with the SWNT reciprocal unit vectors. A detailed discussion of the calculation can be found in reference [9].

The coordinates of the real space unit vectors of graphene can be written as (refer to figure 2.2),

$$\vec{a}_1 = \left(\frac{\sqrt{3}}{2}a,\ \frac{a}{2}\right), \qquad \vec{a}_2 = \left(\frac{\sqrt{3}}{2}a,\ -\frac{a}{2}\right), \tag{2.13}$$

Consequently the coordinates of the reciprocal space unit vectors of graphene are,

$$\vec{b}_1 = \left(\frac{2\pi}{\sqrt{3}a},\ \frac{2\pi}{a}\right), \qquad \vec{b}_2 = \left(\frac{2\pi}{\sqrt{3}a},\ -\frac{2\pi}{a}\right), \tag{2.14}$$

The unit vectors of a SWNT are its chiral vector C_h and translational vector T, and they are expressed as functions of a_1 and a_2,

$$\vec{C}_h = n\vec{a}_1 + m\vec{a}_2, \qquad \vec{T} = t_1\vec{a}_1 + t_2\vec{a}_2, \tag{2.15}$$

where m, n, t_1 and t_2 are integers. To calculate the reciprocal unit vectors of a SWNT, we use the relation $\vec{R}_i \bullet \vec{K}_i = 2\pi\delta_{ij}$, where $\vec{R}_i$ represents C_h and T, and $\vec{K}_i$ represents $\vec{K}_1$ and $\vec{K}_2$ with $\vec{K}_1$ in the direction of the tube circumference and $\vec{K}_2$ along the tube axis. $\vec{K}_1$ and $\vec{K}_2$ can be expressed as a function of $\vec{b}_1$ and $\vec{b}_2$,

$$\vec{K}_1 = \frac{1}{N}(-t_2\vec{b}_1 + t_1\vec{b}_2),\ \vec{K}_2 = \frac{1}{N}(m\vec{b}_1 - n\vec{b}_2), \tag{2.16}$$

where N is the number of hexagons in a SWNT unit cell,

$$N = \frac{\left|\vec{C}_h \times \vec{T}\right|}{\left|\vec{a}_1 \times \vec{a}_2\right|}, \tag{2.17}$$

The 1D SWNT energy dispersion relations is written as,

$$E_\mu(k) = E_{g2D}(k\frac{\vec{K}_2}{\left|\vec{K}_2\right|} + \mu\vec{K}_1),\ \ (\mu = 0,\cdots,N-1,\ and\ -\frac{\pi}{T} < k < \frac{\pi}{T}) \tag{2.18}$$

Along the tube axis $\vec{K}_2$ direction, energy is continuous if the tube is infinite long. If the length of a tube is L_t, the wave vector spacing is $2\pi/L_t$. Along the tube circumference $\vec{K}_1$ direction, wave vector $K_1=2\pi/C_h$. Since C_h is on the order of 1nm and L_t is on the order of 1μm for SWNTs, we consider that the energy is quantized along the K_1 direction due to the confinement of the circumference. Since μ runs from 0 to N-1, there are N π bands to hold 2N p_z electrons of the 2N carbon atoms in the SWNT unit cell.

Equation 2.18 is a general expression of the band structure of a SWNT species. For highly symmetric tubes with small unit cells such as the armchair (n, n) family the calculation can be very simple. The circumference of a (n, n) tube is $\sqrt{3}an$, and the boundary condition is,

$$\sqrt{3}nak_x = 2\pi q, \qquad (q = 1,...,2n) \tag{2.19}$$

If we substitute equation 2.19 into equation 2.11, we obtain the band structure of the (n, n) SWNT,

$$E_q^a(k) = \pm t\left[1 \pm 4\cos\left(\frac{\pi q}{n}\right)\cos\left(\frac{a}{2}k\right) + 4\cos^2\left(\frac{a}{2}k\right)\right]^{1/2}, \quad (2.20)$$
$$(q = 1,...,2n), \quad (-\pi < ka < \pi),$$

Another case of highly symmetric SWNTs is the zigzag (n, 0) family, the band structure of which can be similarly calculated as:

$$E_q^z(k) = \pm t\left[1 \pm 4\cos\left(\frac{\sqrt{3}ka}{2}\right)\cos\left(\frac{q\pi}{n}\right) + 4\cos^2\left(\frac{q\pi}{n}\right)\right]^{1/2}, \quad (2.21)$$
$$(q = 1,...,2n), \quad (-\frac{\pi}{\sqrt{3}} < ka < \frac{\pi}{\sqrt{3}}),$$

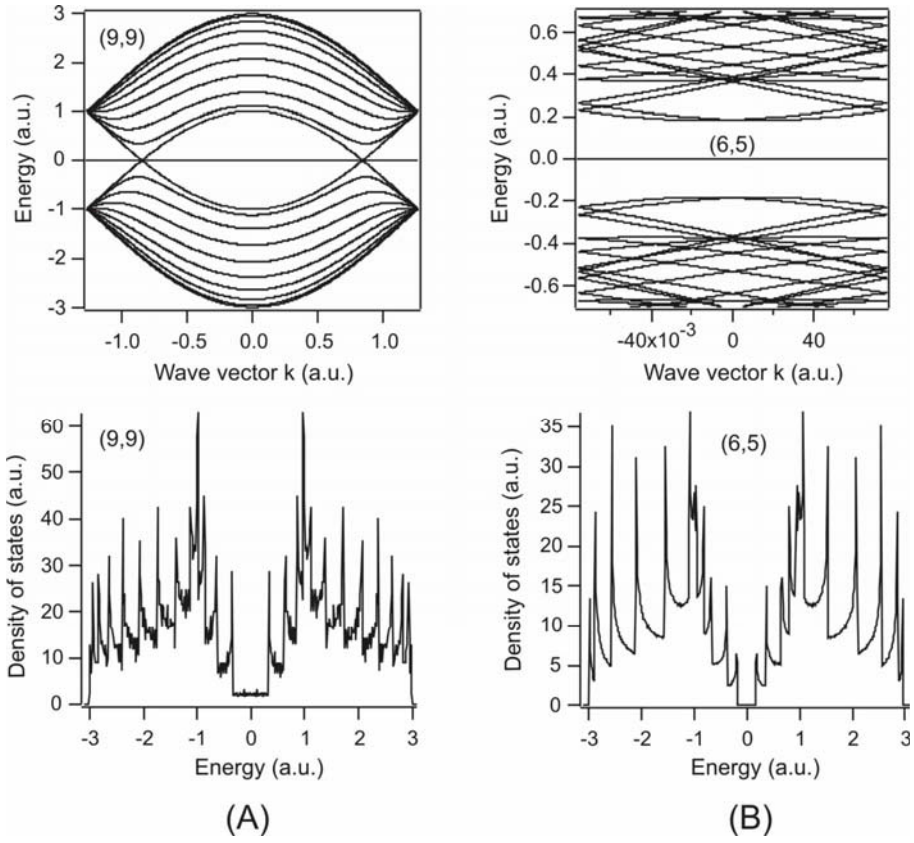

Figure 2.5 Illustration of the band structure and density of states with TBA calculation. (A) The (9, 9) tube. (B) The (6, 5) tube.

Figure 2.5 shows the band structure and density of states (DOS) of the (9, 9) tube and the (6, 5) tube by the TBA for illustrative purposes. For the (9, 9) tube, the valence bands and the conduction bands connect at Fermi level and DOS is not zero at energy E=0, therefore it is metallic; for the (6, 5) tube, the valence bands and the conduction bands separate at Fermi level and DOS is zero at energy E=0, therefore it is semiconducting. The sharp spikes in the DOS in figure 2.5 are referred to as van Hove singularities which are considered as a signature of a 1D material [10, 11].

We may also use the conical dispersion relation near the K point to simply the calculation. We demonstrate this method with the investigation of the band structure features of the zigzag (n, 0) tubes near the Fermi level.

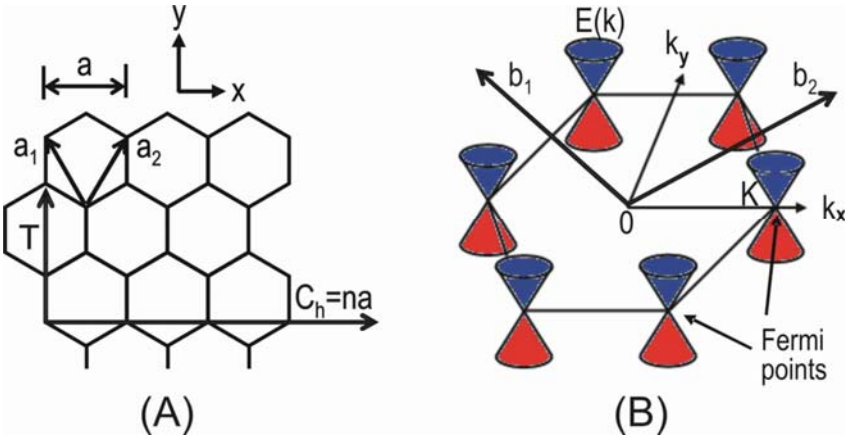

Figure 2.6 Derivation of SWNT band structure features from the conical energy dispersion relation. (A) The chiral and translational vectors of a (n, 0) tube on a graphene lattice. (B) The first Brilloin zone of the graphene showing the conical energy dispersion near K points.

In figure 2.6 (A), the unit vectors of graphene are:

$$\vec{a}_1 = -\frac{a}{2}\hat{x} + \frac{\sqrt{3}}{2}a\hat{y}; \qquad \vec{a}_2 = \frac{a}{2}\hat{x} + \frac{\sqrt{3}}{2}a\hat{y} \tag{2.22}$$

The reciprocal lattice vectors of the graphene shown in figure 2.6 (B) are:

$$\vec{b}_1 = -\frac{2\pi}{a}\hat{k}_x + \frac{2\pi}{\sqrt{3}a}\hat{k}_y; \qquad \vec{b}_2 = \frac{2\pi}{a}\hat{k}_x + \frac{2\pi}{\sqrt{3}a}\hat{k}_y \tag{2.23}$$

Consequently, the coordinate of the K point in k-space is ($\frac{4\pi}{3a}$, 0). Near the K point, the band structure of graphene can be approximated by a conical dispersion relation:

$$\varepsilon = \pm\hbar v_F \left|\vec{k} - \vec{K}\right|, \tag{2.24}$$

where v_F is the Fermi velocity, and $\vec{K}$ is the vector of the K point along k_x direction in figure 2.6.

Next we calculate the wave vectors of the (n, 0) SWNT and substitute them into equation 2.24 to obtain the band structure of the tube near the K point. Shown in figure 2.6(A), the circumference of a (n, 0) tube is na, consequently the amplitude of the unit vector in the reciprocal space k_x direction is $\frac{2\pi}{na}$. In the y direction (along the tube axis) we take the tube as infinite long, therefore the amplitude of unit vector in the k_y direction is very small and we can think that energy is continuous in the k_y direction. With these considerations equation 2.24 becomes,

$$\varepsilon = \pm\hbar v_F \left| v_1 \frac{2\pi}{na}\hat{k}_x + v_2 \Delta k_y \hat{k}_y - \frac{4\pi}{3a}\hat{k}_x \right| \tag{2.25}$$

where v_1 and v_2 are integers. Equation 2.25 is essentially the band structure of the (n, 0) SWNT near the Fermi level. If n is a multiple of 3, then we can always find a proper v_1 so that the k_x component is cancelled, we end up with zero gap materials and we call them metallic tubes. If n is not a multiple of 3, we obtain semiconducting tubes. This result clearly demonstrates how the diameter of a SWNT changes the electronic properties of it. Take n=10 as an example, ignore the k_y component, we have,

$$n = 10, v_1 = 7, \varepsilon_{11} = \pm \frac{1}{15} \frac{\pi}{a} \hbar v_F \quad (2.26)$$

$$n = 10, v_1 = 6, \varepsilon_{22} = \pm \frac{2}{15} \frac{\pi}{a} \hbar v_F \quad (2.27)$$

Where the + and – signs represent the conduction and valence bands respectively and i represents the ith band in ε_{ii}. We see the transition energy between second valance and conduction bands is twice that between the first valance and conduction bands.

The above TBA calculation provides the most fundamental understanding of the SWNT band structures. The TBA successfully explains that the band gap energy of semiconducting tubes is inversely proportional to the tube diameter [9]; it also successfully explains that the electronic prosperities of a SWNT is determined by its chiral indices (n, m): if the difference of n and m equals to a multiple of 3 or zero, the tube is metallic; otherwise it is semiconducting. Yet discrepancies between the TBA theory and the experimental observations exist. For example the TBA predicts that the optical transition energy between the second valence and conduction bands is two times of that between the first valence and conduction bands. While in 2002, Bachilo et al. observed from the photoluminescence excitation (PLE) spectroscopy that the optical transition energies of the SWNTs substantially differ from this prediction and suggested that the difference may partly due to excitonic effects [12]. Kane et al. referred to this difference as the ratio problem and resolved it in a theory by considering the electron-hole interaction in the photo-excited states [13]. In 2005, Wang et al. carried out the two photon PLE spectroscopy [14] and found that to get the same emission wavelength from the semiconducting SWNTs, the energy of two photon excitation is considerably higher than the energy of one photon excitation. These and many other experimental and

theoretical investigations in the recent years suggest that the dominant features in the SWNT spectroscopy correspond to exciton states.

2.3 Fundamentals of excitons in semiconductors

In this section, I introduce some of the general concepts related to excitons in semiconductors and explain the application and peculiarities of such concepts when we look at SWNTs. The focus of the discussion will be on the exciton binding energy and the Coulomb interaction effect on the band edge absorption.

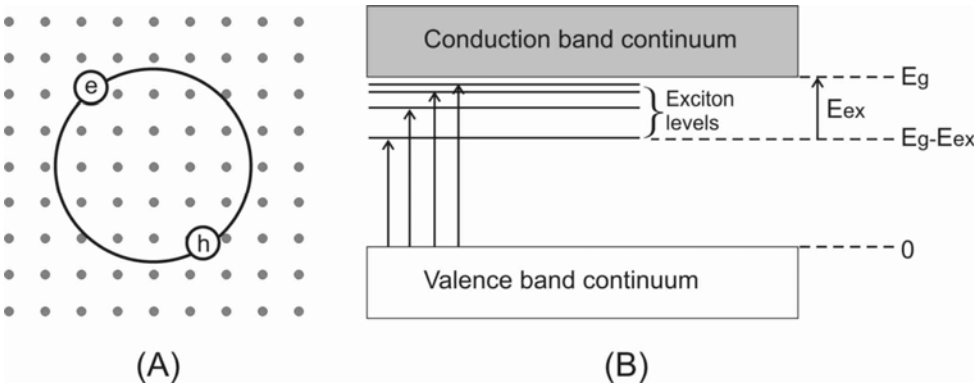

Figure 2.7 Schematic of (A) a Wannier exciton and (B) exciton states.

An exciton is a bound electron-hole pair that can move through a crystal and transport energy [10, 15]. Excitons can be divided into two types corresponding to the two limiting cases of the separation between the electron and hole. When the mean separation of the electron and hole is much greater than the lattice parameter, the exciton is weakly bound and is referred to as a Mott-Wannier exciton, illustrated in figure 2.7 (A). When the separation is less than the lattice parameter and the hole is usually on the

same atom as the electron, the exciton is tightly bound and is referred to as a Frenkel exciton.

The ionization energy needed to separate bound electron-hole pairs is referred to as the exciton binding energy. The resulting exciton states lie below the bottom of the conduction band. Shown in figure 2.7 (B), the exciton binding energy E_{ex} is the energy difference between an exciton level and the bottom of the conduction band. Consequently the energy needed to promote the semiconductor to an exciton state is E_g-E_{ex} where E_g is the band gap energy. The arrows in figure 2.7 (B) illustrate the optical transitions to the exciton levels.

Most results from the theoretical and experimental investigations in the last 4~5 years on the SWNT spectroscopy suggest that the excitons in SWNTs are Wannier type [14, 16, 17] and the following discussion is referred to the Wannier exciton. The formation of excitons in a material has a significant impact on its properties and especially on its absorption spectrum, in which two issues are of fundamental interest in studying the spectroscopy: 1) The binding energies of the exciton states. 2) The role that exciton states play in the absorption spectrum of a material especially near the band edge.

The exciton binding energy of the Wannier exciton can be estimated with the well established Hydrogen atom model. In some respects the Wannier exciton is like a Hydrogen atom with a pair of bound positive and negative charges. Within the continuous medium approximation the interaction between the electron and hole can be described by the screened Coulomb potential $U(r)=-e^2/\varepsilon r$ for the exciton. Solutions to the corresponding Hamiltonian are known from the hydrogen problem and the binding energy is given as [10],

$$E_{ex}(n) = \frac{\mu e^4}{2\hbar^2 \varepsilon^2 n^2}, \qquad \frac{1}{\mu} = \frac{1}{m_e} + \frac{1}{m_h}, \tag{2.28}$$

where μ is the reduced mass, m_e and m_h are the effective masses of electron and hole respectively, n is the principal quantum number, and ε is the dielectric constant. One classical example of exciton states is the cuprous oxide transmission spectrum at 77 K where n=2 to n=5 states were identified [18]. While in the absorption spectrum of SWNTs, the subband edges are not clear and there appears only one bright exciton state below each subband, the determination of the exciton binding energies in SWNTs is more complicated.

The normal Hydrogen model and equation 2.28 are applicable only for the excitons in 3D materials. The SWNT is considered as a quasi 1D material, and we are more interested in solving the hydrogen atom like problem in low dimensionalities. R. Loudon solved the one-dimensional hydrogen atom problem in 1959 [19], and an infinite binding energy was predicted for the 1D hydrogen atom in the ground state. A SWNT is not exactly 1D object because the excitons may move around the circumference of the tube. X.-F. He did an interesting calculation in which the Hydrogen atom like problem was solved in a fractional-dimensional space [20, 21] and the exciton binding energy was predicted for the fractional dimensions from 1 to 3. By applying the Laplace operator in an αD space [22], He constructed a fractional-dimensional Hydrogen atom Schrödinger equation as,

$$\left[-\frac{\hbar^2}{2\mu r \hbar^2} \frac{\partial}{\partial r} \left[r^{\alpha-1} \frac{\partial}{\partial r} \right] + \frac{l^2}{2\mu r^2} - \frac{e^2}{4\pi\varepsilon\varepsilon_0 r} \right] \psi(r,\theta) = (E - E_g) \psi(r,\theta) \tag{2.29}$$

$$where \;\; l^2 = -\frac{\hbar^2}{\sin^{\alpha-2}\theta} \frac{\partial}{\partial\theta} \left[\sin^{\alpha-2}\theta \frac{\partial}{\partial\theta} \right]$$

where μ is the reduced mass of the exciton, r is the relative distance vector, ε is the dielectric constant, E_g is the band gap, E is the exciton energy measured from the top of the valence band, and α is the dimension of a solid (1< α <3). The solution to the above equation gives the binding energy as,

$$E_{ex}(n) = \frac{E_e}{\left[n + \frac{\alpha - 3}{2}\right]^2}, \qquad E_e = \left(\frac{\mu}{\varepsilon^2 m_e}\right) E_H, \tag{2.30}$$

where E_e is the effective Rydberg constant, n=1,2,3…, is the principal quantum number, E_H is the Rydberg constant, and m_e is the free electron mass. Form equation 2.30, the binding energy of 1s exciton is,

$$E_b(1s) = \left[\frac{2}{\alpha - 1}\right]^2 E_e, \tag{2.31}$$

where we see the binding energy increases rapidly as the dimension decreases, in 3D, $E_b(3D)=E_e$; in 2D $E_b(2D)=4E_e$; in 1D $E_b(1D)=\infty$.

Table 2.1 Absorption spectra and Sommerfeld factor of semiconductors in a three dimensional system (after H. Haug and S. W. Koch [11]).

Dimension	Absorption spectra $\alpha(\omega)$ with $\Delta = (\hbar\omega - E_g)/E_0$,	Sommerfeld factor $C(\omega) = \alpha_{cont}/\alpha_{free}$
3D	$\sim \frac{\hbar\omega}{E_0}\left[\sum_{n=1}^{\infty}\frac{4\pi}{n^3}\delta(\Delta + \frac{1}{n^2}) + \Theta(\Delta)\frac{\pi e^{\frac{\pi}{\sqrt{\Delta}}}}{\sinh(\frac{\pi}{\sqrt{\Delta}})}\right]$	$\frac{\frac{\pi}{\sqrt{\Delta}} e^{\pi/\sqrt{\Delta}}}{\sinh(\pi/\sqrt{\Delta})}$

Another important aspect of the exciton theory is the Coulomb interaction effect in the band edge absorption in semiconductors in reduced dimensionalities. Table 2.1 shows the calculated absorption spectrum with Coulomb interaction in 3D semiconducting materials. For simplicity the results of 2D and 1D cases are not shown and they can be found in reference [11]. In table 2.1, $E_0=e^4m_r/[2(\varepsilon_0\hbar)^2]$ is the 3D exciton Rydberg. The spectrum in table 2.1 contains two parts: a continuum due to the ionized states above the band edge; and a series sharp vertical lines corresponding to exciton states with $1/n^3$ decreasing oscillator strengths. The Sommerfeld factor $C(\omega)$ compares α_{cont} and α_{free}, where α_{cont} is the continuum absorption in the spectrum with the Coulomb interaction effects, and α_{free} is the free carrier absorption spectrum. In 3D and 2D cases $C(\omega)>1$ and in 1D case $C(\omega)<1$ near the band edge. The calculation results of 3D, 2D and 1D cases are schematically illustrated in figure 2.8.

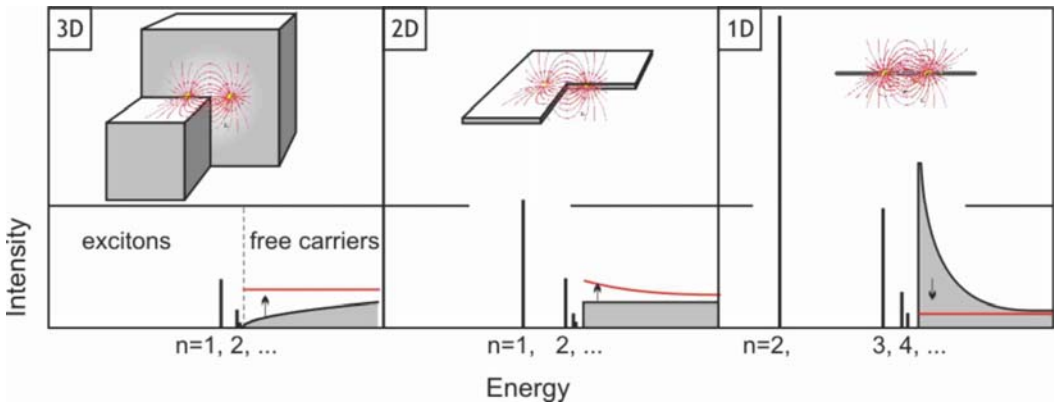

Figure 2.8 Comparison of the screening effect and the band edge absorption spectra with and without the Coulomb interaction in three, two and one dimensional systems.

The upper half of figure 2.8 illustrates the rapid decrease of dielectric screening in the low dimensional systems. In the lower half, the shaded areas illustrate the free carrier absorption spectra; the red lines represent the continuum absorption with Coulomb

interaction; and the discrete vertical lines denote the absorption from exciton states. As the dimensionality decreases, both the exciton binding energy and the exciton state oscillator strength increase rapidly. In 3D, the continuum absorption with Coulomb interaction is constant near the band edge and is higher than the free carrier absorption. In 2D, the continuum absorption is still higher than the free carrier absorption at the band edge and decays with energy. In 1D, on the contrary, the continuum absorption is greatly suppressed and becomes negligible compared with the absorption from the first two exciton states.

The discussion in this section only provides a basic understanding of the general features of the exciton binding energy and the absorption spectrum with the Coulomb interaction effects in the different dimensionalities. The knowledge serves as a ground for us to understand more specific exciton theories of SWNTs in the next section.

2.4 Exciton states in SWNTs

The theory on the exciton states of SWNTs has undergone some important developments during the last 4~5 years and is still under development to correspond to the challenge of new observations from time to time in this vibrant research field. In this section I will review a few representative works on the SWNT exciton theory and prepare us with the information to understand some of the debates in the field.

The following theoretical considerations of the exciton states are associated with the necessity of an interpretation for the low quantum yield (~1%) in SWNTs [23, 24]. If only 1% excitons relax from the E_{11} state to the ground state and give off photons, 99% excitons decay non-radiatively, then there must be some very efficient non-radiative

decay mechanisms, or there may be some optically dark states below the excited state that the excitons go through non-radiatively. The nature and the energy position of these dark states were among the emphases of recent theoretical and experimental investigations.

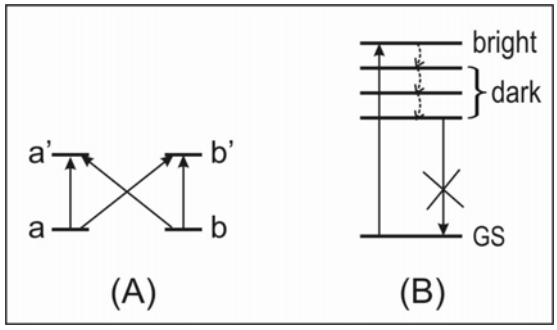

Figure 2.9 Illustration of splitting of single particle excitations due to the electron-electron interaction. (After Zhao et al. [25])

First let us look at the mechanism of the splitting of the single particle excitation spectra with the electron-electron interaction, proposed by Zhao et al. in 2004 [25]. Within the tight binding approximation [9], the highest valence band and the lowest conduction band are both doubly degenerate in zigzag (n, 0) SWNTs, which can be verified in equation 2.21 with the variation of the q value. The degeneracy occurs at different single particle momenta for the chiral SWNTs, as can be seen in figure 2.5 of the (6, 5) tube for the bands crossing. Figure 2.9 illustrates the basic idea of the excitation state splitting. In (A), bands a and b are originally degenerate in the valence band, so are a' and b' in the conduction band, and four degenerate transitions are denoted by the arrows. In (B), when the electron-electron interaction is included, the degeneracy is lifted which leads to four excited states with the top one bright (dipole allowed) and all others dark. Electrons rapidly relax through dark states and the radiative decay is forbidden from

lowest dark state to the ground state. This model only considers the electron-electron interaction and does not include the spin-spin interaction of excitons that is an essential part of some more recent models.

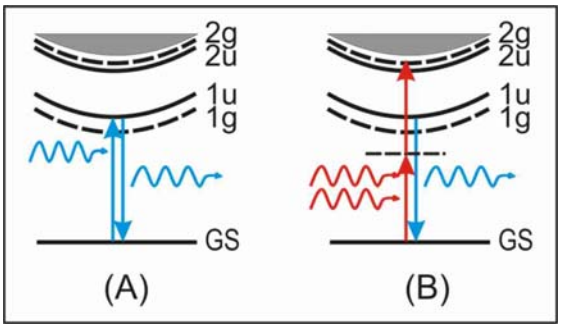

Figure 2.10 Illustration of the one and two photon allowed states in the two-photon excitation experiment. (After Maultzsch et al. [16])

In 2005, a two photon allowed state below the band edge was observed from the two photon excitation spectra on some SWNT species [14, 16] and the observed states were explained with a calculation that was more focused on the symmetry of the exciton wave functions [16]. Shown in figure 2.10, 1u and 1g are one-photon odd and even symmetry states respectively, 2u and 2g are two-photon odd and even states respectively, and only the 1u and 2g states are optically active. The even and odd symmetry are with respect to a π rotation perpendicular to the tube axis. Figure 2.10 (A) shows that the one photon excitation energy is the same as the emission energy at the 1u state. Figure 2.10 (B) shows that the energy of the two photon excitation energy is higher than the emission energy at the 1u state. The enhancement of the 1u state emission at a specific two-photon excitation energy implies the existence of a two-photon allowed state. According to this model, excitons may relax from the 1u state to the 1g state and decay non-radiatively to the ground state. This model still does not include the spin interaction of excitons.

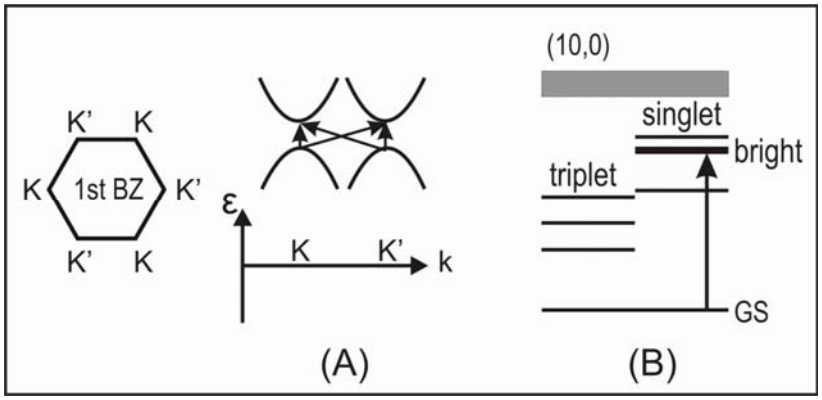

Figure 2.11 Dark exciton states with spin interactions. (A) Illustration of the K-K' inter valley mixing in the single particle picture. (B) Illustration of the lowest spin-singlet and spin-triplet exciton states of the (10, 0) tube (After Spataru et al. [30]).

During 2004 to 2006, Zaric et al. investigated the absorption spectra and photoluminescence (PL) spectra of SWNTs and observed that the E_{11} peak (corresponding to the lowest bright exciton state) of some semiconducting tubes split into two under some high magnetic fields [26-28]. The mechanism for this splitting is explained in detail in Ando's model of the SWNT exciton states in which a 16-fold degeneracy was proposed by considering the K-K' inter valley mixing and electron spin interaction [29]. The basic idea is illustrated in figure 2.11 (A). K and K' are two points at the corners of the first Brillouin zone (1st BZ). Transitions between the bands at K and K' leads to a 4-fold degeneracy. The spin-spin interaction between the electron and the hole leads to another 4-fold degeneracy, combined they make 16 degenerate states in which 4 are singlet states and 12 are triplet states. Two of the singlet states are optical active but only one is bright without the magnetic field; a strong magnetic field splits the two active singlet states and makes both of them bright. The ordering and splitting of these states are associated with the short-range Coulomb interaction and the exciton wave

function. Exciton singlet and triplet states have also been predicted with first principle calculations by Spataru et al. for the (10, 0) tube [30], illustrated in figure 2.11 (B). The singlet states are higher than the triplet states, and the bright singlet state lies between two dark singlet states with the high lying dark state doubly degenerate.

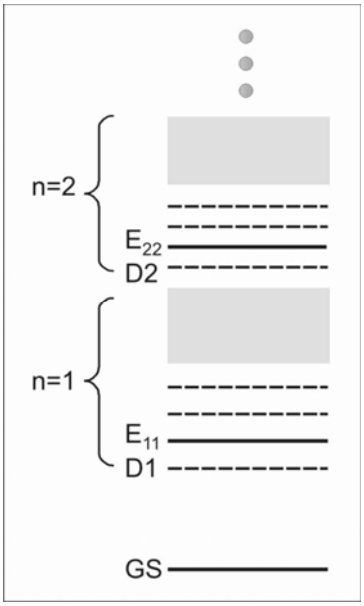

Figure 2.12 Schematic of exciton states in SWNTs.

Let us use the schematic of the SWNT exciton states in figure 2.12 to summarize what we have learned so far to avoid confusion caused by the different schools of theories on the subject. The shaded areas represent the continuum subbands which are truncated for the clarity of the exciton states, and the dashed lines denote the optical dark exciton singlet and triplet states. E_{11} and E_{22} are the bright exciton states observed in the absorption spectrum, each associated with a continuum subband. Between the E_{11} and the band edge of the first subband there is a two-photon allowed state that has been observed experimentally for some tube species (not shown in the figure). The general exciton

theory discussed in the last section as well as the first principle calculation on SWNTs [17] predict that there are more states between E_{11} and the band edge, but so far those states have not been directly observed in either the absorption spectrum or the ultrafast transient spectrum. When the electron and hole spin interaction is considered, the E_{11} state is the bright singlet state. In Spataru's calculation the E_{11} of the (10, 0) tube is surrounded by two dark singlet states, while the generic model by Ando suggests that the ordering of the singlet and triplet states are contingent on the exciton wave function and the Coulomb interaction in different SWNT species. Nevertheless, the general agreement is that there are dark singlet states around the bright singlet state and the triplet states are probably in lower energy levels which may act as the non-radiative decay channels for excitons. The arguments about singlet and triplet states in the E_{11} range also apply to the E_{22} range.

The number and the energy positions of the dark singlet and triplet states are still in debate so far. Spataru et al. predicted an energy difference of about 30 meV between the E_{11} and the low lying dark singlet states in the (10, 0) SWNTs. While Mortimer et al. investigated the energy splitting between the bright and dark exciton states with a temperature dependent photoluminescence study [31]. For a dozen SWNTs with the diameters from 0.78 nm to 1.17 nm, they claimed that the energy separation were from 5.5 meV to 1 meV, which is considerably smaller than the predicted value by Spataru et al.

All the models on the SWNT exciton states discussed in this section are valuable and it is not hard to see the resemblance of these theories in some respects. The discrepancies among them come from different interaction factors included in the

calculation and different emphases they were targeted to. The subtlety of the ordering and separation of the exciton states awaits further experiments to resolve.

In summary, this chapter has been focused on the understanding of the electronic structure of SWNTs from the fundament concepts to the current debates. For the time being, many aspects of the electronic structures of SWNTs are still unclear, such as the exciton binding energy, the position of the continuum band edge, the positions of the dark exciton states, the non-radiative decay channels, etc. The theories on the electronic structures of the SWNTs are still under developing, the difficulty for a breakthrough lies in the lack of a convincing way to directly probe the dark states. The discussion given in this chapter provides a background of the theoretical considerations of SWNT exciton states when we look at the experimental data in the later chapters.

Reference:

[1] S. Iijima, Nature, **354**, 56 (1991).
[2] P. G. Collins and P. Avouris, Scientific American, (December 2000).
[3] M. S. Dresselhaus, G. Dresselhaus and Ph. Avouris, *Carbon Nanotubes: Synthesis, Structure, Properties and Applications*, Springer, New York, 2001.
[4] A. K. Geim and A. H. MacDonald, Phys. Today, p35, (August 2007).
[5] E. Kaxiras, *Atomic and Electronic Structures of Solids*, Combridge University Press, Combridge, 2003.
[6] T. Hamada, M. Furuyama and T. Tomioka et al., J. Mater. Res. **7**, 1178 (1992).
[7] X. Blase, L. X. Benedict and E. L. Shirley et al., Phys. Rev. Lett. **72**, 1878 (1994).
[8] S. G. Louie. In *Progress in Fullerene Research: International Winter School on Electronic Properties of Novel Materials*, edited by H. Kuzmany, J. Fink and M. Mehring et al., page 303, 1994. Kirchberg Winter School, World Scientific Publishing Co. Ltd., Singapore.
[9] R. Saito, G. Dresselhaus and M. S. Dresselhaus, *Physical Properties of Carbon Nanotubes*, Imperial College Press, London, 1998.
[10] C. Kittel, *Introduction to Solid State Physics*, 8th ed., John Wiley & Sons, Inc., 2005.
[11] H. Haug and S. W. Koch, *Quantum Theory of the Optical and Electronic Properties of Semiconductors*, 4th ed., World Scientific Publishing Co., 2004.
[12] S. M. Bachilo, M. S. Strano and C. Kittrell et al., Science, **298**, 2361 (2002).
[13] C. L. Kane and E. J. Mele, Phys. Rew. Lett. **90**, 207401 (2003).

[14] F. Wang, G. Dukovic, and L. E. Brus et al., Science, **308**, 838 (2005).
[15] D. L. Dexter and R. S. Knox, *Excitons*, Interscience Publishers, New York, 1965.
[16] J. Maultzsch, R. Pomraenke and S. Reich et al., Phys. Rew. B, **72**, 241402 (2005).
[17] C. D. Spataru, S. Ismail-Beigi, and L. X. Benedict et al., Appl. Phys. A, **78**, 1129 (2004).
[18] P. W. Baumeister, Phys. Rev. **121**, 359 (1961).
[19] R. Loudon, Am. J. Phys. **27**, 649 (1959).
[20] X.-F. He, Phys. Rev. B, **43**, 2063 (1991).
[21] X.-F. He, Phys. Rev. B, **42**, 11751 (1990).
[22] F. H. Stillinger, J. Math. Phys. **18**, 1224 (1977).
[23] L. Huang, H. N. Pedrosa and T. D. Krauss, Phys. Rew. Lett. **93**, 017403 (2004).
[24] J. Crochet, M. Clemens, and T. Hertel, J. Am. Chem. S. **129**, 8058 (2007).
[25] H. Zhao and S. Mazumdar, Phys. Rew. Lett. **93**, 157402 (2004).
[26] S. Zaric, G. N. Ostojic and J. Kono et al., Science **304**, 1129 (2004).
[27] S. Zaric, G. N. Ostojic and J. Shaver et al., Phys. E **29**, 469 (2005).
[28] S. Zaric, G. N. Ostojic and J. Shaver et al., Phys. Rev. Lett. **96**, 016406 (2006).
[29] T. Ando, J. Phys. Soc. Japan, **75**, 024707 (2006).
[30] C. D. Spataru, S. Ismail-Beigi, and R. B. Capaz et al., Phys. Rew. Lett. **95**, 247402 (2005).
[31] I. B. Mortimer and R. J. Nicholas, Phys. Rev. Lett. **98**, 027404 (2007).

CHAPTER III

EXPERIMENTAL SETUP AND AUTOMATION OF OPA

The importance of experiments in scientific researches for acquiring new knowledge and new theories is unquestionable. Take the carbon nanotube research field as an example, the observation of the electron microscope image of multi-wall carbon nanotubes by Dr. Iijima [1] marked the burgeoning of this field; the achievement of isolation of SWNTs in aqueous surfactant suspensions marked the new phase of the research in which spectroscopic properties of specific tube species can be extracted through bulk measurements [2]; and the observation of a second exciton state from the two-photon photoluminescence excitation (PLE) spectra greatly bolstered the exciton picture in SWNTs [3]. These and many other experiments significantly enriched the understanding of carbon nanotubes and fostered new theories on these one dimensional material.

Speaking of experiment, one powerful technique to study the SWNT properties-for example the electronic structure discussed in the last chapter- is the optical pump-probe experiment. Optical pump-probe spectroscopy with ultrashort laser pulses is a powerful tool to study the excited state dynamics, which helps to understand the electronic structure, the carrier relaxation channels, the quantum yield, the electron-phonon interaction and so on, of a material. The main part of this dissertation is on the pump-probe spectroscopy study of SWNTs.

The experimental setup, the principle of the experiment and the sample preparation are particularly important in carrying out the pump-probe experiment on SWNTs and will be discussed in this chapter. The organization of this chapter is as follows. In the first section, I introduce the configuration of our ultrafast laser system; the emphasis is on the mechanism of short pulse generation and modulation in the system. In the second section, I discuss in detail the function of the optical parametric amplifier (OPA) which is the key component in the laser system, and introduce a project we carried out to upgrade the OPA to automatic wavelength tuning. In the third section, I discuss the setup of the pump-probe experiment and its basic principle. In the last section, I briefly introduce the sample preparation procedure we used to make the purified SWNT suspension samples.

3.1 Configuration and principle of the ultrafast laser system

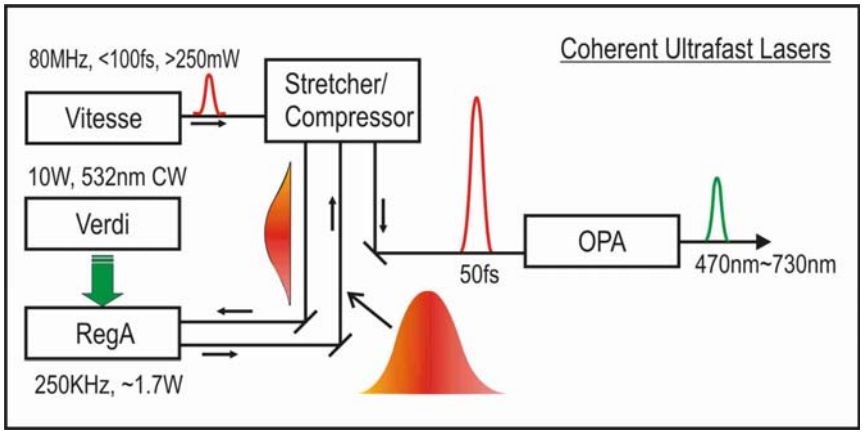

Figure 3.1 Schematic of the femtosecond laser system.

In this section I first provide a brief overall description of the laser system and then discuss in more detail the functions of some key components in the system. Figure 3.1

shows the schematic of the laser system which consists of five main components: Vitesse, Verdi, RegA (regenerative amplifier), Stretcher/Compressor and OPA -all from Coherent Company. The Vitesse is a mode locked Ti:Sapphire laser that generates 100 fs 800 nm laser pulses with a 250 mW output power. The pulses enter the Stretcher and are stretched by a factor of one thousand in order to avoid damage of the crystals in the RegA when the laser power is amplified. The elongated pulses enter the RegA where the power is amplified to about 1.7 W and the repetition rate is adjusted to 250 kHz. The Verdi provides a 10 W 532 nm CW laser as the pumping source for the RegA. The output pulses from the RegA enter the Compressor and are compressed to 50 fs before entering the OPA. Inside the OPA, the 800 nm pulses are used to generate several light sources: a "signal" beam that can be tuned from 470 nm to 730 nm with an about 60 mW output power; an "idler" beam that is tunable from 940 nm to 2400 nm with a few milliwatts output power usually; and a white light continuum that spans from 400 nm to 1600 nm roughly. These light sources are used in the pump-probe experiment.

The Vitesse, RegA and OPA are particularly interesting in terms of the principle of ultrashort pulse generation and modulation. In the following I discuss the functions of Vitesse and RegA in more detail. The function of OPA, combined with a method to upgrade the OPA for automatic wavelength tuning, will be discussed in the next section.

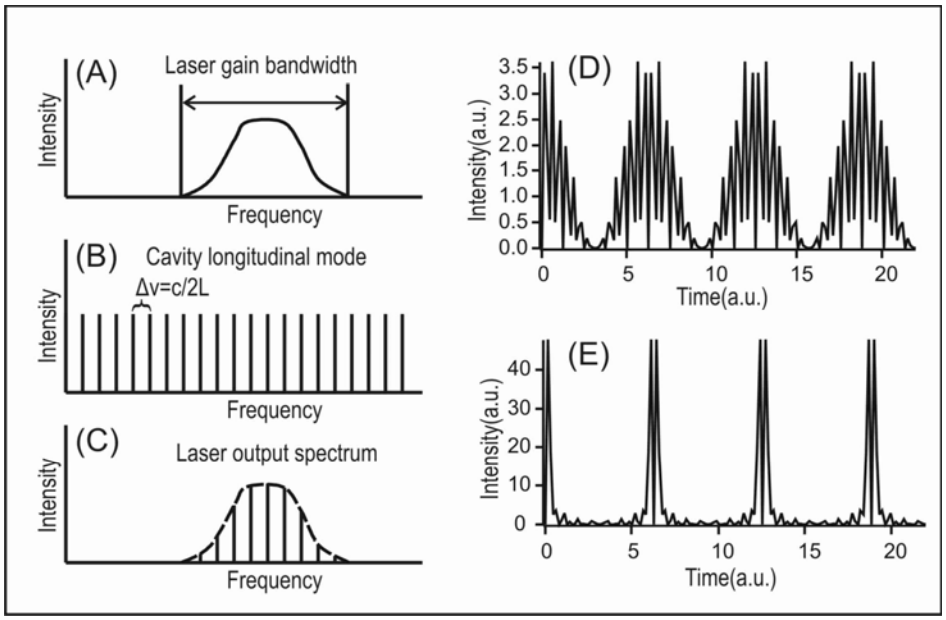

Figure 3.2 Illustration of the mode locking principle

The most important principle to understand in the Vitesse is the method it generates the short pulses-mode locking [4]. Inside the Vitesse, a Ti:Sapphire crystal absorbs pump light and emits lights around 800 nm which then oscillate inside the Vitesse cavity. Figure 3.2(A) shows that the laser gain is greater than the loss only within some frequency range called laser gain bandwidth in the gain medium. Figure 3.2(B) illustrates that there are many possible cavity longitudinal modes (frequencies) with which an electromagnetic wave can oscillate inside the cavity. The longitudinal modes can be considered as the standing wave modes between two end mirrors of the cavity. $\Delta\nu$ is the frequency separation between two adjacent modes, c is the speed of light in the cavity, and L is the length of the cavity. Figure 3.2(C) shows that only the modes under the envelope of the gain profile can maintain. Usually all the modes under the gain profile have random phases to each other and the laser is a continuous wave. If all the modes are managed to be in phase, superposition of all the modes will result in a pulsed laser.

Figure 3.2(D) shows the superposition of two adjacent modes that are in phase, the pulses have a broad pulse width and a low intensity. Figure 3.2(E) shows the superposition of eight adjacent modes when they are in phase, the pulses have a much narrower pulse width with a much higher intensity. This technique is referred to as the mode locking. For simplicity all the modes used in the calculation in figure 3.2(D) and 3.2(E) are sinusoidal waves with the amplitude of 1 for the electric field.

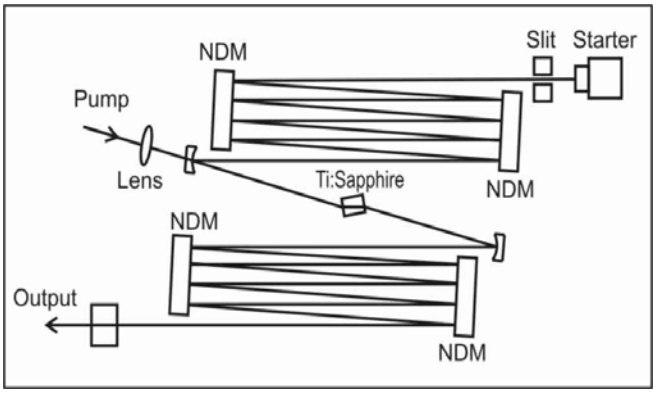

Figure 3.3 Ultrafast laser head in Vitesse

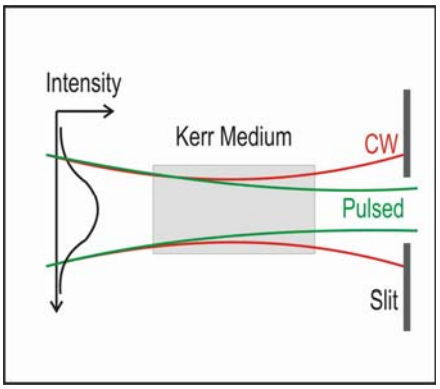

Figure 3.4 Kerr lens effect

The key component to realize the mode locking in the Vitesse is the ultrafast laser head, shown in figure 3.3. The gain medium Ti:Sapphire crystal absorbs the pump light (532 nm from a small Verdi inside the Vitesse) and emits the 800 nm light that oscillates between the two end mirrors of the cavity-the starter and the output coupler. The automatic starter changes the cavity length at a proper speed to trigger the initiation of mode locking. The negative dispersion mirrors (NDM) provide the total negative dispersion compensation to produce sub-100 fs pulses. The CW component in the laser is largely removed by the Kerr lens effect [5], shown in figure 3.4. The pulsed laser has a much higher intensity than the CW laser in the cavity, and this high intensity changes the

index of refraction of the crystal so that the beam diameter of the pulsed laser is smaller than that of the CW laser. A slit is then used to block the CW laser and let the pulsed laser pass. The Kerr lens effect also helps to reduce the pulse width by suppressing the low intensity component in the pulse (wings of the pulse). This concludes our discussion on the Vitesse.

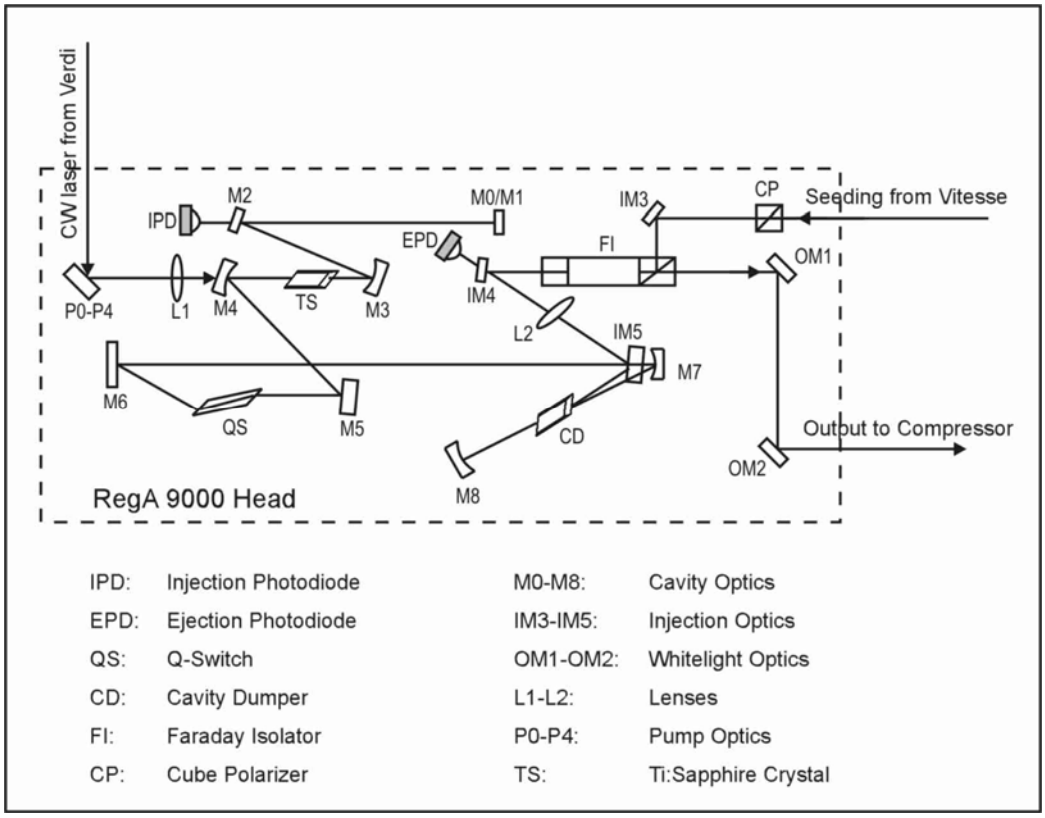

Figure 3.5 RegA optical schematic.

We now discuss the composition and function of the RegA shown in figure 3.5. In our practice, the RegA has to be realigned roughly once in a year to maintain the high output power from it and it is necessary to understand the RegA in order to realign it. The 532 nm CW pump light from the Verdi enters the RegA from the left in figure 3.5. The

beam is steered with P0 to P4 periscope mirrors and focused by L1 lens into a Ti:Sapphire crystal (TS). If alignment in the cavity is good, 800 nm light should start lasing between the two end mirrors M0 and M8. The beam path in the cavity is M0/M1→M2→M3→TS→M4→M5→QS→M6→M7→CD→M8. The Q switch prevents lasing until a pulse from the Vitesse is injected. The 800nm pulse from the stretcher enters the RegA from the right in figure 3.5. The beam goes through the cube polarizer CP, IM3, faraday isolator FI, IM4, L2, IM5 and reaches the cavity dumper CD. The faraday isolator prevents the feedback of the RegA output into the cavity. By an acousto-optic interaction, the cavity dumper helps to inject a Vitesse pulse in the cavity and to eject the pulse out of the cavity after the pulse is amplified.

The Q switch is an acoustic-optic modulator that has a normal angled TeO_2 (Tellurium dioxide) crystal with an acousto-optic transducer matched to respond to 80 MHz RF excitation. The RF excitation generates 80 MHz acoustic waves in the Q-switch to diffract out part of the 800 nm laser inside the RegA cavity. The energy loss from this diffraction prevents lasing in the RegA cavity so as to help store energy in the TS crystal. The principle of the Q-switch is based on the modification of the refractive index of the crystal by the oscillating mechanical pressure of a sound wave. More information on the Q-switch can be found elsewhere [6].

The faraday isolator contains a rod of Faraday material placed in the magnetic field generated by some permanent magnets. When the RegA output 800 nm laser goes through the rod, the polarization of the light is rotated by 45 degrees. A crystal quartz optical rotator next to the rod also rotates the laser polarization by 45 degrees. The polarization rotations of the Faraday rod and the quartz rotator are not symmetric with

respect to the propagation direction of light. When the RegA output laser goes out through the Faraday isolator, the two polarizations cancel and there is no attenuation of the output beam; but when the laser comes back in through the FI, the polarizations add and cause attenuation to prevent a high power feedback into the cavity. More information on the faraday isolator can be found elsewhere [7].

The cavity dumper CD is also an acoustic-optic modulator that has a Brewster angled [6] SiO_2 plate with an acoustic-optic transducer matched to respond to 380 MHz RF excitation. The controller electronics of the RegA provides a sufficiently short RF pulse to create a short acoustic pulse to diffract only one pulse from a 76 MHz pulse chain. To amplify a pulse from the Vitesse, the electronic controller launches two acoustic pulses in the CD. The first acts to inject a Vitesse laser pulse into the RegA cavity soon after the Q-switch is turned off, the second acts to eject this pulse from the cavity after it reaches maximum amplitude. More information on the principle of cavity dumper can be found elsewhere [6].

The repetition rate of the amplified pulses in the RegA is limited only by the laser storage time in the gain medium. The storage time of Ti: Sapphire is about 2.5 μs at the room temperature. The pulse energy does not decrease until we decrease the pulse separation to 3 times of the storage time. With the normal repetition rate of 250 kHz (4 μs pulse separation) of the RegA, the energy per pulse reduces to 80% of its maximum while the average power is relatively high at 50% of the CW average power. The repetition rate of the RegA can be adjusted from 10 kHz to 250 kHz [8].

3.2 Upgrading of OPA for Automatic wavelength tuning

Only the OPA in the ultrafast laser system needs frequent adjustment in order to tune its output wavelength in a wide range and to optimize its output power. Different output wavelengths from the OPA are used as different excitation energies in the pump-probe experiment to verify the SWNT excited state dynamics, this verification plays a key role in examining the existing theories and developing a new interpretation for the excited state dynamics of SWNTs, more details about this investigation will be discussed in the next chapter. The OPA we used originally had to be tuned manually which demanded some practice and made the OPA tuning a little tedious to do. We later upgraded the OPA to tune its wavelength automatically based on our experience on aligning and tuning the OPA. This automation greatly facilitates the usage of the OPA as a source of different wavelengths and hence facilitates the pump-probe experiment. Moreover, upgrading the OPA is only the first step of the automation of the pump-probe spectroscopy, the next step is to combine the automated OPA with the cross correlation signal detection function to make a fully automation instrument for pump-probe spectroscopy, which will be a great tool to study excited state dynamic of SWNTs as well as other materials.

In the first part of this section, I discuss the function and principle of the OPA, and a method to upgrade it to tune wavelength automatically. In the second part of this section, I discuss the detailed procedure to upgrade the OPA and present the wavelength tuning curves from the upgraded OPA.

3.2.1 Principle of OPA and method of automation

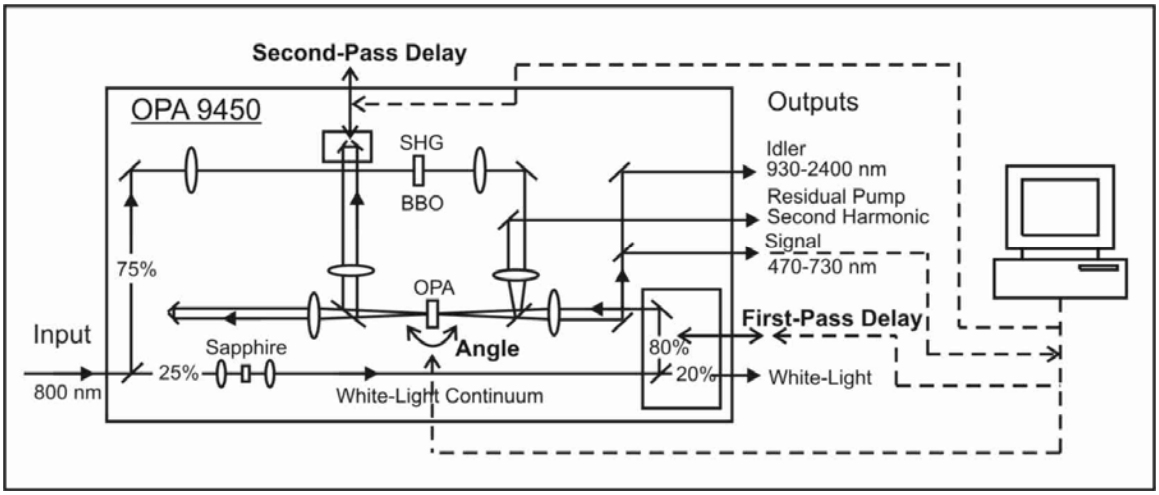

Figure 3.6 Schematic of OPA and method of automation

In this part I first provide an overall description of the function of the OPA shown in figure 3.6, then I discuss the key process in the OPA-the parametric amplification in the OPA crystal- in more detail, in the end I introduce a method to automate the OPA.

The basic function of the OPA is to generate light with tunable wavelengths from the 800 nm pump beam. In figure 3.6, the dashed lines and the computer symbol on the right show the idea of automation that will be discussed later; the rest is the schematic of the OPA. The input of the OPA is the RegA amplified 800 nm 50 fs laser that enters the OPA from the left in figure 3.6. 75% of the light is reflected to a second harmonic generation (SHG) Beta-Barium Borate crystal (BBO) to generate a 400 nm light and 25% of the light goes through a sapphire crystal to generate a white light continuum. Of the white light continuum, 20% leaves the OPA and is used as the source of the probe beam in the pump-probe experiment, and 80% goes through the first pass delay stage and is

then focused in the OPA crystal. The 400 nm beam from the SHG BBO is likewise focused in the OPA BBO crystal. Parametric amplification happens when the focuses of the both pulses (white light and 400 nm) are spatially and temporally overlapped inside the OPA crystal. After the white light and 400 nm pass the OPA crystal the first time, a pair of wavelengths in the white continuum is amplified by the splitting of some of the 400 nm photons. The white light travels through some optical delay, the 400 nm travels through the second pass delay stage, then they go through the crystal the second time to further amplify the same pair of wavelengths (one is called signal and the other idler) which are then reflected out of the OPA with dielectric mirrors.

A detailed explanation of the concept of parametric amplifier can be found elsewhere [9]. In the case of OPA, the parameter should mean the wavelength of the output laser, and the parametric amplifier amplifies particular wavelength components in the white light continuum. In the following we discuss the principle of the OPA process in detail.

When the 400 nm beam passes through the OPA crystal, part of the 400 nm photons split into a pair of photons with one photon in the range from 470 to 730 nm and the other in the range from 930 to 2400 nm roughly. Energy conservation of this process leads to the following equation

$$1/400=1/\lambda_1+1/\lambda_2, \qquad (3.1)$$

where λ_1 and λ_2 are the wavelengths in nm of the two split photons. The specific pair of wavelengths into which the 400 nm photons are to split is determined by the momentum conservation observed in the process, or in practice by adjusting the OPA crystal angle. A little review of the crystal birefringence will help to explain this mechanism.

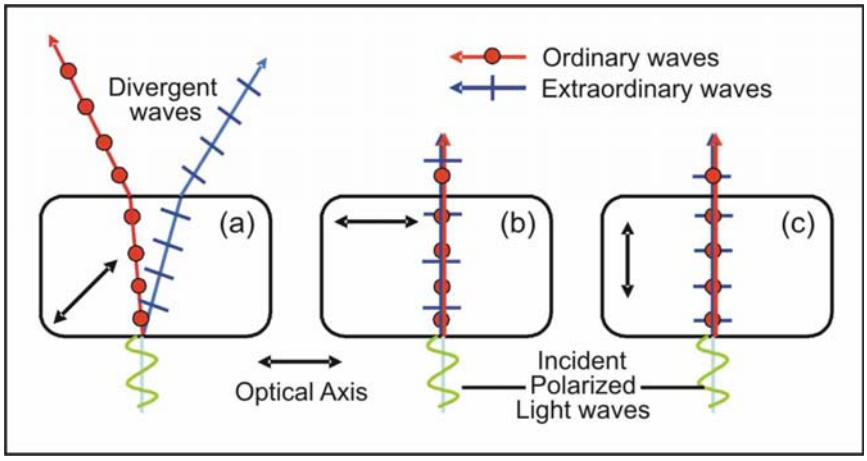

Figure 3.7 Separation of light by a birefringent crystal (after [10])

Figure 3.7 illustrates the propagation of a non-polarized light through a birefringent crystal. In case (a) when the optical axis of the crystal is neither parallel nor perpendicular to the light propagation direction, the light splits into two polarized waves with polarization directions perpendicular to each other. One is called ordinary wave which does not change its propagation direction when the crystal is rotated; the other is called extraordinary wave which changes its direction with the rotation of the crystal. In case (b) when the light propagation direction is perpendicular to the optical axis, the ordinary wave and the extraordinary wave do not separate but there is a phase shift between two waves. And in case (c) when the light propagates along the direction of the optical axis, there is no separation or phase shift between the two waves and the crystal acts like an isotropic material. Birefringence originates from complex molecular and atomic lattice orientations that have varying electrical properties with respect to the crystal axis [10], so that light rays passing through the crystal can experience different refractive indices depending upon the direction of propagation.

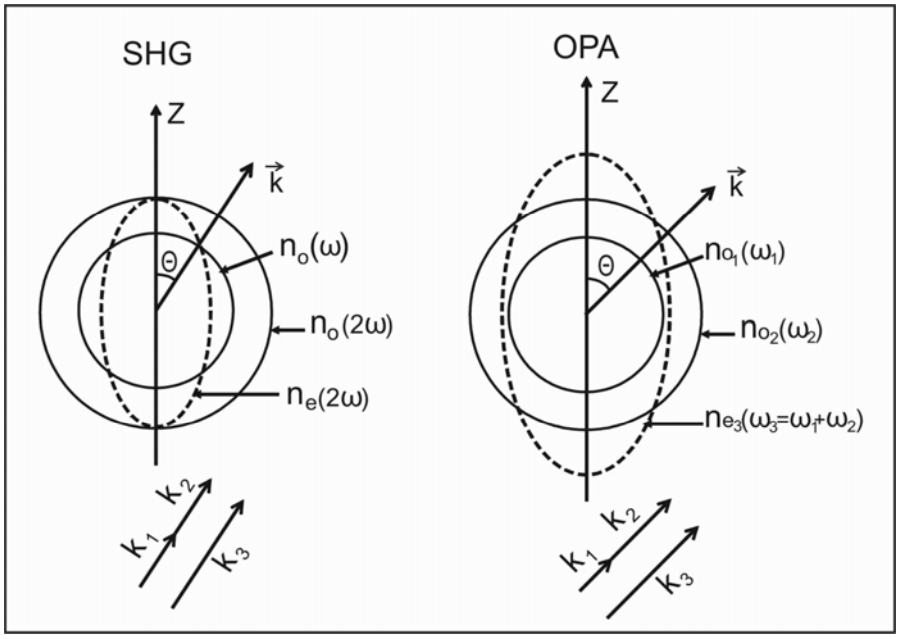

Figure 3.8 Momentum conservation in SHG and OPA crystals

With the revisit of the birefringence concept, we now discuss the momentum conservation of light in the SHG and OPA crystals with the aid of refractive index ellipsoid [5], shown in figure 3.8. First we discuss the second harmonic generation case in which two 800 nm photons merge to create a 400 nm photon, shown in the left of figure 3.8. The two solid spheres represent the refractive index of the ordinary waves with frequencies ω and 2ω, corresponding to 800 nm and 400 nm respectively; the dashed ellipsoid represents the refractive index of the extraordinary wave with a frequency 2ω. The crystal optical axis is along Z direction. The momentum conservation requires

$$k_3(2\omega)=k_1(\omega)+k_2(\omega), \qquad (3.2)$$

where k_1, k_2 and k_3 are the wave vectors of the two 800 nm and one 400 nm photons respectively. Since the three waves propagate collinearly, i.e. $k_3 \parallel k_1 \parallel k_2$, and $c/n = \omega/k$, equation 3.2 leads to

$$n_e(2\omega)*2\omega = n_o(\omega)*\omega + n_o(\omega)*\omega, \text{ or } n_e(2\omega)=n_o(\omega). \quad (3.3)$$

This condition is met when all the waves propagate along the k direction through the intersection of the $n_e(2\omega)$ and $n_o(\omega)$ ellipsoids in figure 3.8 left.

ω_1 is not equal to ω_2 in the OPA crystal case shown in figure 3.8 right, and momentum conservation in the OPA process requires,

$$n_e(\omega_3)*\omega_3=n_o(\omega_1)*\omega_1+n_o(\omega_2)*\omega_2,$$

$$\text{or } n_e(\omega_3) = [n_o(\omega_1)*\omega_1+n_o(\omega_2)*\omega_2]/(\omega_1+ \omega_2). \quad (3.4)$$

Since $\omega_3=\omega_1+\omega_2$ due to energy conservation, $n_e(\omega_3)$ should be a value between $n_o(\omega_1)$ and $n_o(\omega_2)$, as illustrated in the figure 3.8 right. In practice, the 400 nm photon splits into a different pair of photons when the OPA crystal optical axis is tuned to a different angle θ against the propagation direction of the 400 nm laser beam.

The above mentioned OPA process does not incorporate the white light with the 400 nm light. When the 400 nm light is mixed with the white light in the OPA crystal, the signal and idler components in the white light continuum act as the seeding lights which are amplified by the conversion of part of the 400 nm light into them. With these seeding lights, the OPA output power reaches saturation with a shorter travel distance in the OPA BBO crystal and the OPA process obtains a better efficiency of frequency conversion.

After a detailed explanation of the principle of the OPA, we now discuss how to tune the OPA to different wavelengths and how to automate the tuning. Mostly three parameters need to be adjusted when we tune to a new wavelength: the OPA crystal angle

that controls the output wavelength, the first pass delay and the second pass delay that control the temporal overlap of the 400 nm pulses and the white light pulses when they pass through the OPA crystal the first time and the second time respectively, as illustrated with bold words in figure 3.6. Sometimes the spatial overlap of the 400 nm and the white light also needs a fine tuning by adjusting some mirrors or lenses when the wavelength needs to be tuned over a wide range. The original OPA uses manual tuning of micrometer set screws to adjust those three parameters, we replaced the micrometers with computer controlled motor driven actuators (actuator Z625B, motor driver ODC001, Thorlabs) that have a minimum incremental movement of 0.05 μm. We use a pre-calibrated polynomial fit to tune the OPA crystal angle for a new wavelength. A pre- calibrated polynomial fit does not work for tuning the first and second pass delays, because the output power drops considerably even when the position of the first or second pass delay is 1 or 2 μm off, the polynomial fit is not that accurate and from time to time the optimum position of the both delays may offset by more than 1 μm. Therefore we let the computer search for the optimal first and second pass delay positions based on the feedback of the OPA output power with an algorithm called downhill simplex method. This is illustrated schematically by the dashed lines in figure 3.6 where the computer assigns new positions to the OPA crystal angle, the first and second pass delay stages, and accepts the output power of the OPA signal as the feedback in searching and optimizing the positions.

3.2.2 Implementation of the OPA automation

It can be seen from the OPA automation method discussed above that the key to implement the automation is to select an appropriate algorithm with which the computer

searches for the optimal first and second pass delay positions. Many different algorithms to find the maximum or minimum value of a multi-variable function can be used to search for the first and second pass positions, for example, the simplest algorithm is to make one dimensional scan for first pass and second pass positions separately. The algorithm we finally adopted is the so-called downhill simplex method [11] which requires fewer measurements and settles down a new wavelength much faster than the 1D scan.

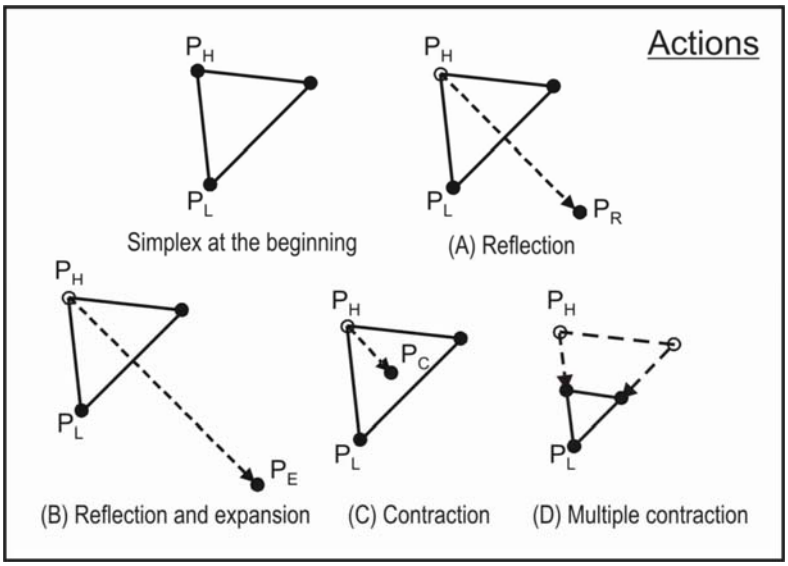

Figure 3.9 Actions of downhill simplex method

A simplex is a geometrical figure consisting of N+1 points (in N dimensions) and all their interconnecting line segments, polygonal faces, etc [11]. In OPA automation we need to vary two variables-the first and second pass delay positions-to find the maximum output power, so the problem is in two dimensions and the simplex is a triangle. Established by Nelder and Mead [12], the downhill simplex method is used to find the minimum of a function in multiple dimensions quickly and effectively by combination of

four types of actions, which are illustrated in a two-dimension case in figure 3.9. At the beginning we measure an unknown function at three points and find the highest value at point P_H and the lowest value at point P_L. The simplex method uses one of four actions to search in the next step. In the reflection action in figure 3.9(A), the next measurement is taken at a point P_R which is a reflection of the highest value point P_H. In the reflection and expansion action in figure 3.9(B), the next point P_E is the reflection and expansion of the point P_H. In the contraction action in figure 3.9(C), the next point P_c is a contraction from P_H. Finally in the multiple contraction action in figure 3.9(D), two new points result from contraction from the two points with higher values. After any of these actions, we obtain a new set of three points (denoted by solid dots in figure 3.9) to start a new action until the stop condition is met. It is straight forward to use the same method to find the maximum value of a function simply by multiplying the measured function value by -1.

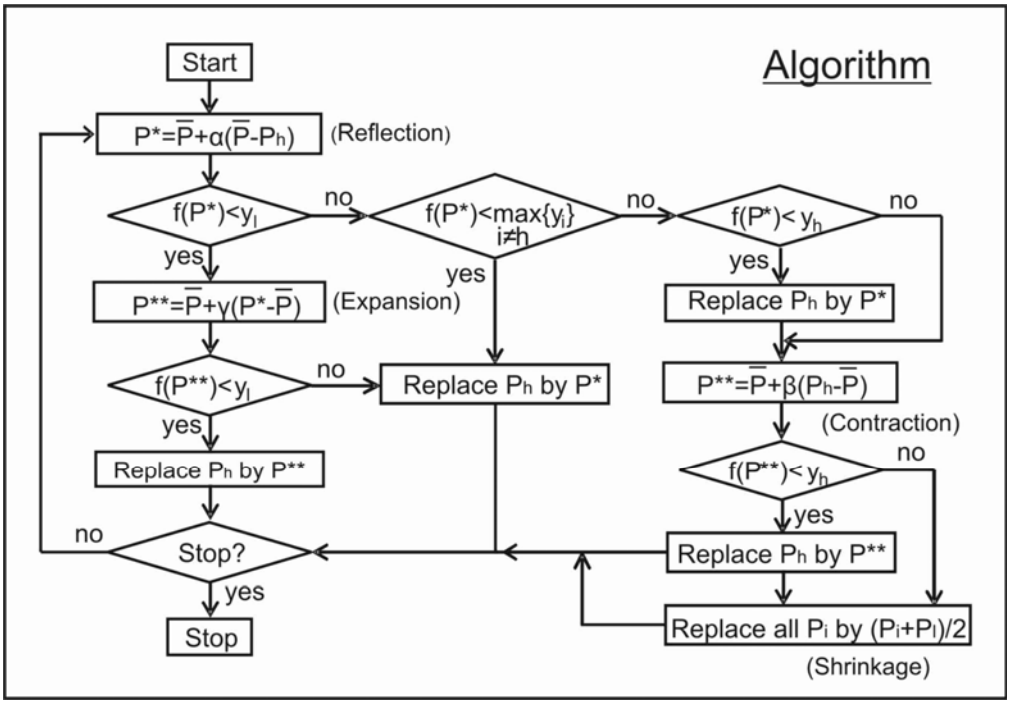

Figure 3.10 Algorithm with the downhill simplex method

Figure 3.10 shows the algorithm we adopted to write a Labview program to search for the best positions of the first and second pass delays with the downhill simplex actions. Take a simplex of three points as an example, to start, we measure the value of an unknown function at three points (in OPA automation we measure the output power at three pairs of the first and second pass positions). Then we use a reflection action to get the next point $P^* = \overline{P} + \alpha(\overline{P} - P_h)$, where $\overline{P}$ is the average position of the initial three points, P_h is the point where the unknown function has the highest value in the initial three points, and α is a characteristic length scale of our guess. If the measured value $f(P^*)$ is smaller than the lowest value y_l of the unknown function at the previous three points, then we use an expansion action to get a new point $P^{**} = \overline{P} + \gamma(P^* - \overline{P})$, where γ is a length scale of guess. If $f(P^{**})$ is still smaller than the previous low value y_l, then we replace the P_h point with P^{**}. Then we check if the value $f(P^{**})$ meets the condition to stop. If yes, the program stops; if no, it will launch a new search with a new set of three points. The above procedure describes the left column of the flowchart in figure 3.10; the rest of the flowchart can be understood in a similar fashion.

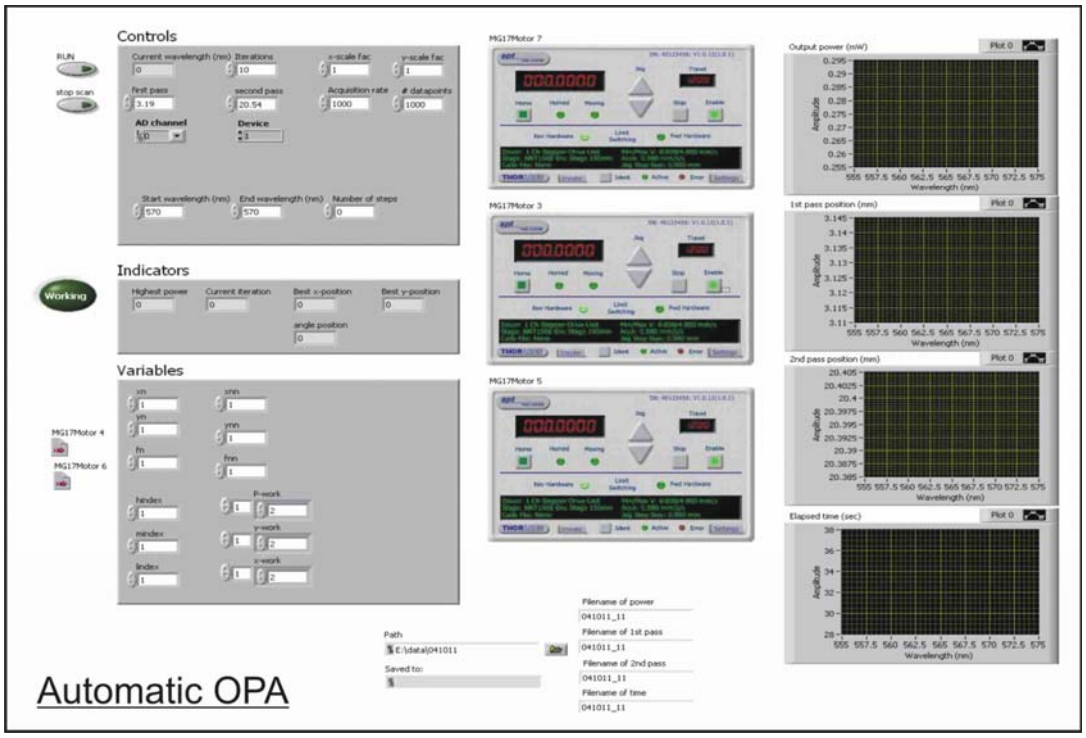

Figure 3.11 Labview VI front panel of the automated OPA

Figure 3.11 shows the front panel of the Labview VI that has incorporated the above mentioned algorithm to automatically tune the OPA wavelength. In the left column, we use the "Controls" panel to input the values of the OPA crystal angle, the first and second pass positions of a starting wavelength, and to specify the scanning range and step size of wavelength tuning. We use the "Indicators" panel to display the current output power, first and second pass positions when the program searches for the best positions in iterations. We use the "Variables" panel to display some intermediate calculated positions to monitor the searching process. In the middle column, there are three instrument panels that come with the motor drivers and display the positions of the actuators (i.e. positions of the angle, first pass and second pass) in real time. These panels are also used to reset the initial positions of the actuators. In the right column, four

display windows show the output power, the first pass, the second pass, and the tuning time as functions of the wavelength. In the middle bottom, we provide filenames and a directory to save the tuning results in the computer.

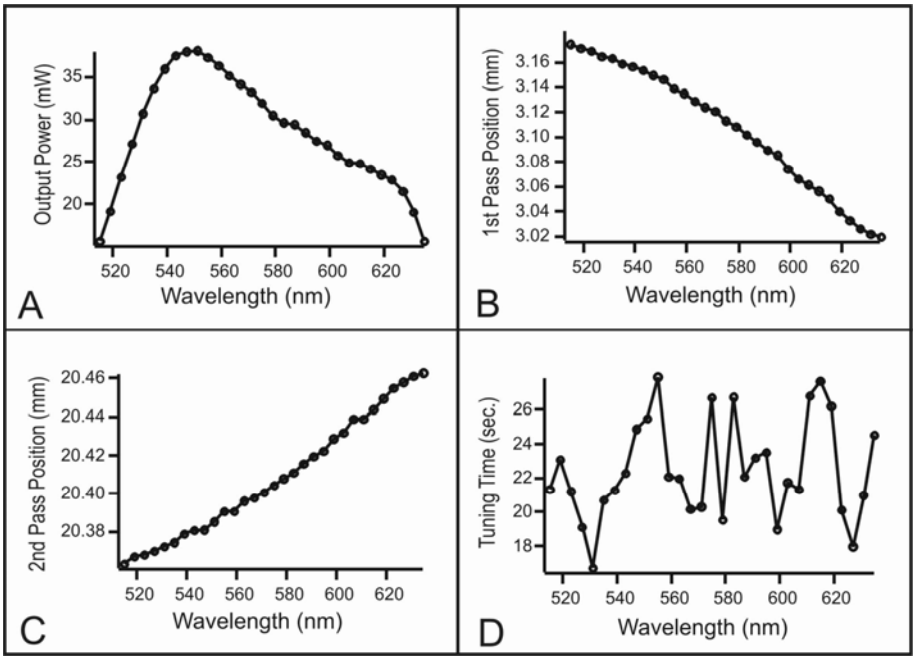

Figure 3.12 Tuning curves with automated OPA

Figure 3.12 shows the tuning curves generated by the automated OPA in which the wavelength was tuned roughly from 520 nm to 630 nm with 4 nm per step. Figure (A) shows the variation of the OPA output power as the wavelength was tuned. The maximum power appears at 550 nm around where the initial spatial alignment in the OPA was optimized. The power drops gradually towards longer wavelength mainly due to deviation from optimal spatial alignment, and the power drops abruptly at shorter wavelength side mainly due to the dielectric mirror of the output laser, whose normal measure range is from 550 nm to 650 nm. Figure (B) shows the variation of the position of the first pass delay stage as the wavelength was tuned. Roughly the first pass delay

stage moves 5 micrometers for every 4 nm wavelength change. Figure (C) shows the variation of the position of the second pass delay stage as the wavelength was tuned. Roughly the second pass delay stage moves 3 micrometers for every 4 nm wavelength change. Figure (B) and (C) intuitively explain the considerable drop of the output power when the first or second pass position is even 1 μm off the optimal. With 10 μm the smallest scale on the hand tuning micrometer, it needs more patience to optimize the power by hands than to optimize it with the computer controlled actuator with 0.05 μm minimum incremental movement. Figure (D) shows the variation of the time to tune to each new wavelength. It takes fewer than 30 seconds to settle down to a new wavelength with the automated OPA, which is very fast compared with the hand tuning.

To summarize this section, we explained the function of the OPA and the detailed principle of the optical parametric amplification process in the OPA. We proposed a method to automate the wavelength tuning of the OPA with detailed information on hardware and computer program algorithm for the upgrading. The upgraded OPA tunes the wavelength expeditiously, which not only reduce the human effort and avoid human errors in hand tuning, but also reduce the reliability on the stability of the femtosecond laser system in the pump-probe experiment. Once incorporated with the cross-correlation function in our experiment, it will become an even more powerful tool to carry out ultrafast spectroscopy of SWNTs and other materials.

3.3 Setup and basic principle of the pump-probe experiment

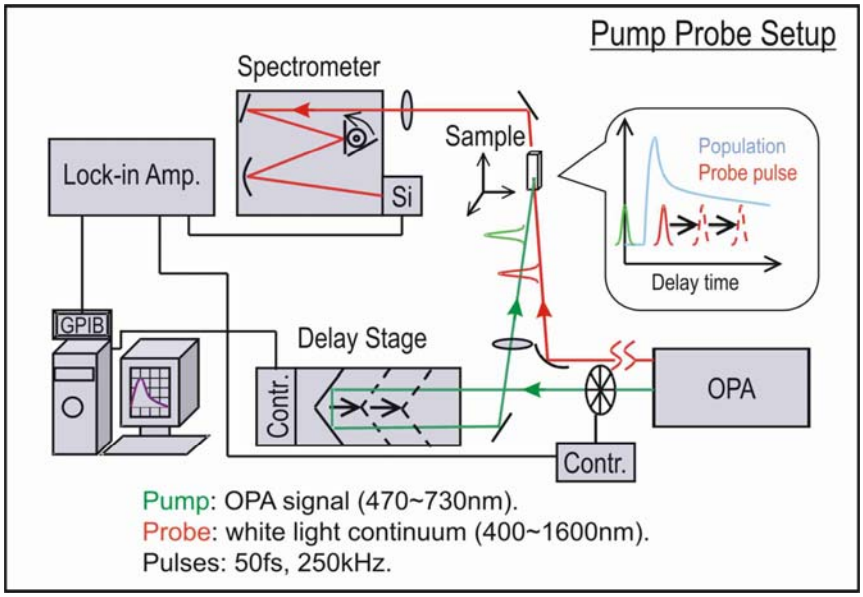

Figure 3.13 Setup of the pump-probe experiment.

Figure 3.13 shows the setup of our pump-probe experiment. Both the pump and probe pulses are generated in the OPA and have a 50 fs pulse width and a 250 kHz repetition rate. The pump beam (green) is taken from the "signal" of the OPA which is tunable from 470 nm to 730 nm with pulse fluences of up to 0.3 μJ. A computer controlled delay stage (Physik Instrumente, PI-M521.DD) adjusts the pump beam delay with a bi-directional reproducibility of positions of 0.1 μm=0.66 fs. The time resolved information is collected by scanning the delay stage to vary the pump pulse and the probe pulse separation, as shown in the inset in figure 3.13. After the delay stage, the pump beam is focused into a 1*1*5 cm spectrophotometer cell by using a lens of 100 mm focal length. The probe beam (red) is taken from the white light continuum with a broad band from 400 nm to 1600 nm roughly. It goes through some optical delay and then is also

focused into the cell by using a spherical reflective optics with 100 mm focal length. Both the pump and probe beams at the focus are estimated to be roughly 100 μm in diameter. For alignment purposes the sample cell is put on a XYZ stage on which a pinhole with a 100 μm diameter can be attached to facilitate alignment of the spatial overlap of the pump and probe beams. The broad band probe beam is dispersed in a spectrometer (Jobin Yvon, triax 320) and detected by a thermoelectrically cooled Si/InGaAs sandwich detector. Optical transients $\Delta T/T_0$ or $\Delta I/I_0$ (differential transmission), or $\Delta\alpha$ (differential absorption) can be recorded in a computer with a sensitivity of up to $2*10^{-6}$ by using phase sensitive detection of a lock in amplifier by chopping the pump beam at 1 kHz.

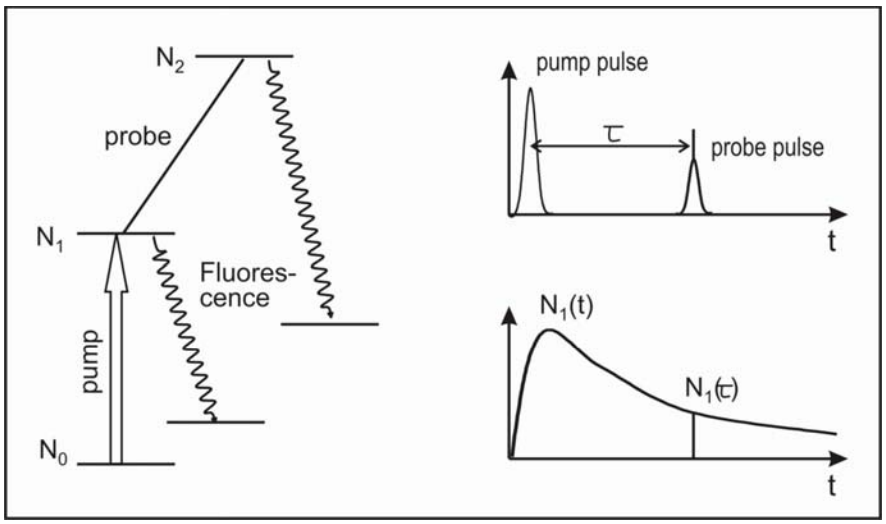

Figure 3.14 Pump and probe technique (after Demtröder [5]).

Figure 3.14 illustrates the pump-probe technique with a detection scheme for a molecular system [5]. The pump pulse excites charged carriers from N_0 to N_1 state, and the probe pulse with an energy matching the energy difference between N_1 and N_2 states detects the population density at N_1 state. By varying the probe pulse delay time against

the pump pulse, the time evolution of the population density $N_1(t)$ is probed. The time resolution of the signal is only limited by the width of the pump and probe pulses and is not affected by the instrument detection time constant. Thus pump-probe technique with femtosecond pulses is ideal to study very fast relaxation processes. Different pump-probe scheme investigates different relaxation information in the system, for example the probe signal with a degenerate pump-probe scheme between the N_0 and N_1 state reveals the $N_1(t)$-$N_0(t)$ population density.

The probe signal in the pump-probe experiment is related to the third order polarizability $P^{(3)}(\omega)$ of the material and the amplitude of the probe field $E_T(\omega)$ as follows [4]:

$$\frac{\Delta I(\omega)}{I_0(\omega)} \approx \frac{n\omega L}{\varepsilon_0 c} \mathrm{Im} \frac{P^{(3)}(\omega)}{E_T(\omega)}, \qquad (3.5)$$

where differential transmission $\Delta I/I_0 = e^{-\Delta\alpha(\omega)L}$, L is the optical path length in the probe volume with refractive index n. In the pump-probe experiment with SWNTs, the probe signal resonant with an exciton state probes the difference of population in the ground (g) and the exciton (X) states (ρ_{XX}-ρ_{gg}) without considering the coherent effect [4].

The interpretation of the probe signal on SWNT samples is much more complicated than a textbook two level system in that, the dynamics of relaxation and the repopulation of the ground and excited states may involve a number of additional states such as the triplet states, dark exciton states and trap states that affect the return to the ground state [13, 14]. Investigating the influences from the additional states to the exciton state and estimating the real carrier dynamics of the exciton state is a challenging task in studying the SWNT dynamics and will be discussed in detail in chapter 4.

3.4 Sample preparation and characterization

Sample preparation had a crucial impact on the study of SWNT spectroscopy in the last 4~5 years. Raw SWNT sample soot contains catalyst and ropes that quench the luminescence from SWNTs and broaden absorption spectra [15], and it is estimated that 70 to 90% of the laser-vaporized-grown SWNT raw material consist of ropes [16]. Early efforts on sample preparation were not very successful in that samples were dominated by small bundles [17-23]. Around 2002, O'Connell et al. discovered that micelles formed from SDS surfactant molecules in D_2O can isolate SWNTs after they were broken up from ropes with sonication [15]. Thus prepared samples for the first time allowed extraction of features of specific SWNT species from bulk measurements in absorption spectra and photoluminescence spectra, although the samples still contained a fair amount of impurities. In 2005, Arnold et al. made another revolutionary improvement to the SWNT sample preparation [24]. By ultracentrifugation of DNA wrapped SWNTs in an aqueous density gradients, they not only got rid of the dark impurities but also enriched and separated SWNTs with different diameters that form different color bands in the centrifugation vial.

Our samples are prepared from CVD synthesized CoMoCat material [25] that is enriched in the (6, 5) SWNT. First, we mix 1 mg of the SWNT soot with 2 wt% sodium cholate surfactant in 20 ml water. We then ultrasonically agitate the mixture in an ice bath using a Branson 450 Sonifier with a tapered microtip at 30% duty cycle for about two hours. We obtain a dark suspension in which micelles formed from sodium cholate molecules wrap and separate individual SWNTs. we next put 2 ml of the suspension inside the density gradients prepared with iodixanol in a 10 ml centrifugation vial and

centrifuge it in a Sorvall ultracentrifuge with a swinging bucket rotor at 100,000g for 12 hours. All the dark impurity is then pushed to the bottom of the vial and the (6, 5) tubes form a thin layer of purple band in the vial. We then use a syringe pump to take out 10 to 20 fractions across the purple band with 100~150µl each and analyze the absorption spectra of them to find the best fraction. More detailed information on the sample preparation can be found elsewhere [26, 27].

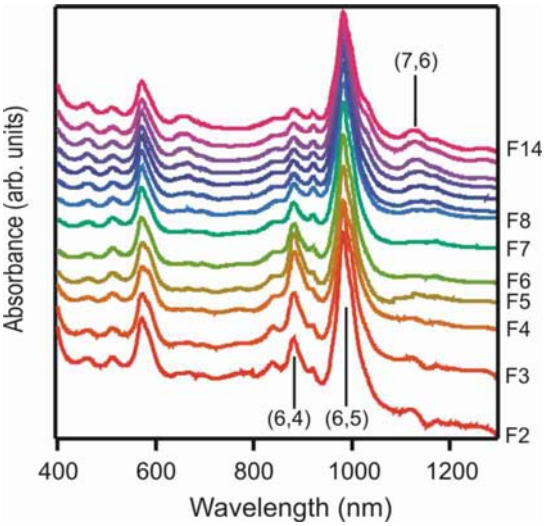

Figure 3.15 Absorption spectra of different fractions of the (6, 5) tube enriched sample

Figure 3.15 shows the absorption spectra of the different fractions that are normalized and offsetted for clearer comparison. We notice that the feature of the (6, 4) tube is more pronounced in the early (low density) fractions (F2~F6) and the feature of (7, 6) tube is pronounced in the later (high density) fractions (F12 ~F14), which suggests that a large diameter tube have a high density in the density gradients. Judged by the real absorption peak amplitude of the (6, 5) tube and the peak ratio of the (6, 5) tube to other

tubes, we decide that fraction 8 and 9 have the highest concentrations of the (6, 5) tubes and are used for the pump-probe experiment.

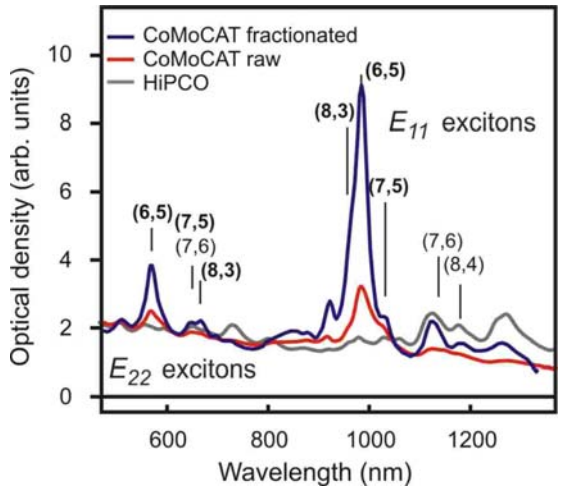

Figure 3.16 Comparison of absorption spectra of different SWNT samples

Before we conclude this section I like to provide a comparison of some SWNT samples used in the ultrafast spectroscopy in the recent years, shown in figure 3.16. Although the SWNTs are separated by surfactant micelles in all these samples, only the fractionated CoMoCat has gone through the density gradients centrifugation process. The HiPCO [28] sample has several SWNT species with competing concentrations and we refer it as a polydisperse sample. CoMoCAT raw sample without fractionation by density gradients shows pronounced features of the (6, 5) SWNT, yet the (6, 5) tube peak height to background ratio is low. The fractionated CoMoCat sample shows greatly enhanced features from the (6, 5) tubes. In pump-probe spectroscopy, the signals from different SWNT species always interact with each other. The (6, 5) tube enriched sample allows us

to greatly reduce the interferences from minority tube species, therefore provides us more confidence to identify true signals of one tube specie.

To summarize this chapter, we first discussed the configuration and function of the ultrafast laser system with emphases on pulse generation and modulation in the Vitesse and RegA, we then explained the function of the OPA and the method to tune its wavelength automatically, after that we discussed the setup of the pump-probe experiment and its basic principle with a prediction of the complexity of the interpretation of the probe signal in SWNT samples, at last we discussed the sample preparation procedure and showed the advantage of our sample with a comparison with some other commonly used samples in the research field.

References:

[1] S. Iijima, Nature, **354**, 56 (1991).
[2] S. M. Bachilo, M. S. Strano and C. Kittrell et al., Science, **298**, 2361 (2002).
[3] F. Wang, G. Dukovic and L. E. Brus et al., Science, **308**, 838 (2005).
[4] C. Rulliere (Ed.), *Femtosecond Laser Pulses: Principles and Experiments*, Springer, 1998.
[5] Wolfgang Demtröder, *Laser Spectroscopy: Basic Concepts and Instrumentation*, 2nd Edition, Springer, 1996.
[6] B. Hitz, J. J. Ewing and J. Hecht, *Introduction to Laser Technology*, 3ed Edition, IEEE press, Inc., New York, 2001.
[7] http://www.dmphotonics.com/Faradays_QA.htm
[8] Regenerative amplifier operator's manual, Coherent, Inc., 11/98.
[9] Amnon Yariv, *Optical Electronics*, 4th edition, Saunders College Publishing, 1991.
[10] http://micro.magnet.fsu.edu/primer/lightandcolor/birefringenceintro.html
[11] W. H. Press, et al., *Numerical Recipes in C*, Combridge Universit Press, 1992.
[12] J. A. Nelder and R. Mead, Computer Journal, **7**, 308 (1965).
[13] H. B. Zhao and S. Mazumdar, Phys. Rev. Lett. **93**, 157402 (2004).
[14] V. Perebeinos, J. Tersoff and P. Avouris, Phys. Rev. Lett. **92**, 257402 (2004).
[15] M. J. O'Connell, S. M. Bachilo and C. B. Huffman et al., Science, **297**, 593 (2002).
[16] A. Thess, R. Lee and P. Nikolaev et al., Science, **273**, 483 (1996).
[17] J. Liu, A. G. Rinzler and H. Dai et al., Science, **280**, 1253 (1998).
[18] M. J. O'Connell, P. Boul and M. Ericson et al., Chem. Phys. Lett., **342**, 265 (2001).
[19] S. Bandow, A. M. Rao and K. A. Williams et al., J. Phys. Chem. B **101**, 8839 (1997).

[20] J. Shen, M. A. Hamon and H. Hu et al., Science **282**, 95 (1998).
[21] G. S. Duesberg, J. Muster and V. Krstic et al., Appl. Phys. A **67**, 117 (1998).
[22] A. B. Dalton, C. Stephan and J. N. Coleman et al., J. Phys. Chem. B **104**, 10012 (2000).
[23] R. Bandyopadhyaya, E. Nativ-Roth and O. Regev et al., Nano Lett. **2**, 25 (2002).
[24] M. S. Arnold, S. I. Stupp and M. C. Hersam, Nano Lett., **5**, 713 (2005).
[25] D. E. Resasco, W. E. Alvarez and F. Pompeo et al., J. Nanoparticle Res. **4**, 131 (2002).
[26] T. Hertel, Z. Zhu and J. Crochet et al., Phys. Stat. Sol. (b) **243**, 3186 (2006).
[27] J. Crochet, M. Clemens and T. Hertel, J. Am. Chem. S. **129**, 8058 (2007).
[28] P. Nikolaev, M. Bronikovski and R. K. Bradley et al., Chem. Phys. Lett., **313**, 91 (1999).

CHAPTER IV

ULTRAFAST SPECTROSCOPY OF (6, 5) SEMICONDUCTING SWNTS

The ultrafast pump-probe spectroscopy of the (6, 5) SWNTs is the main content of this dissertation. During the last five years, numerous time-resolved ultrafast spectroscopy experiments have been carried out on SWNTs; the results and analyses have led to a greatly improved understanding of SWNTs optical and electronic properties. The results have also raised some debates in the SWNT ultrafast spectroscopy that essentially boil down to two fundamental issues: one is the excited state dynamics which studies the carrier relaxation time scale and relaxation channels from the excited states; the other is the origin of the photoinduced absorption features in the transient spectrum. In this chapter, we report some new observations on the two issues through a more thorough investigation that not only resolve some controversial observations in some prior reports, but also lead to a better understanding of the two mechanisms.

The controversial observations and interpretations in some prior reports may partially due to the different samples, laser systems, and experiment schemes used in different research groups. Our experiment has two advantages compared with the prior experiments: first, we do pump-probe excitation spectroscopy, to be specific we vary the pump wavelength continuously across the E_{22} resonance of the (6, 5) tube to verify the dynamics of the E_{11} and E_{22} probe signals, while no pump wavelength dependence of the dynamics has been carried out in the prior experiments. Second, we use chirality-enriched fractionation-purified SWNT samples that help to greatly reduce the signal influence

from minority tube species to the main (6, 5) species, while polydisperse samples were used in most prior experiments the spectra of which show competing features from different tube species. These two advantages provide us the possibility to study the ultrafast spectroscopy with unprecedented details.

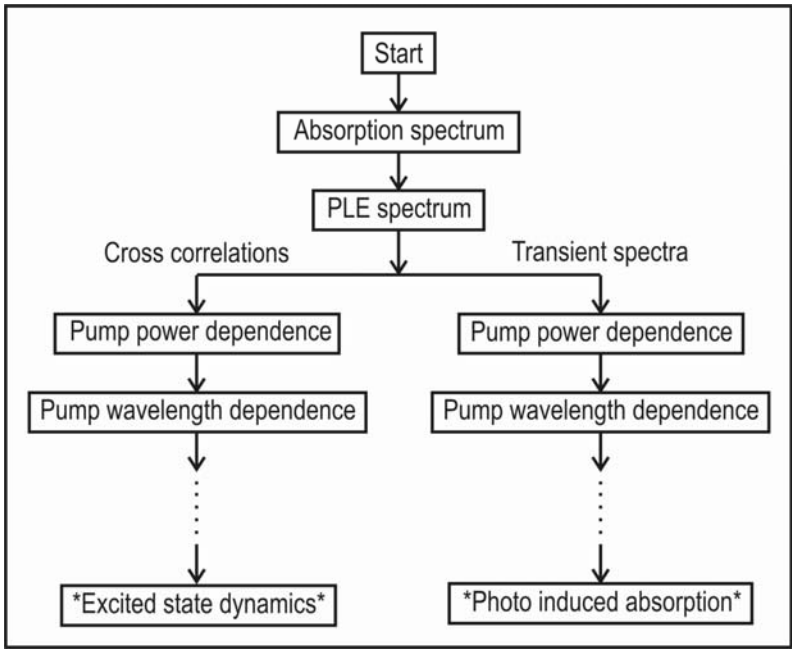

Figure 4.1 General procedure of pump-probe measurements

Figure 4.1 shows our general procedure to carry out the pump-probe experiment on SWNTs. Before the pump-probe experiment, we characterize the sample with the absorption spectrum and PLE spectrum. The absorption spectrum reveals the positions of the exciton states and roughly the relevant concentration of different tube species in the sample. The PLE spectrum reveals the emission variation from semiconducting SWNTs upon different CW excitation wavelengths. Both the absorption spectrum and the PLE spectrum help us to decide the pump-probe scheme (pump and probe wavelengths) in the

experiment. The pump-probe experiment measurement can be arranged into two ramifications: in one, the measurement is mostly the cross correlations that provide the information of carrier relaxation from individual states; in the other, the measurement is more focused on the transient spectra that reveal the spectral response of the sample after excitation. The experiment approaches used in the two ramifications are the same: we may investigate the signal dependences on the pump power, the pump wavelength, the sample temperature, the SWNT length, the SWNT bundle size, the surfactant in the SWNT suspension, the amount of defects in SWNTs etc, as implied by the dotted lines in figure 4.1. The investigation in the cross correlations ramification leads to an interpretation for the excited state dynamics, and the investigation in the transient spectra ramification leads to an explanation for the mechanism of the photoinduced absorption.

Figure 4.1 also serves as a guide for the arrangement of the data presented in this chapter that contains mainly the pump power and pump wavelength dependences investigation. In the first part of this chapter, I present our experiment results on the (6, 5) tube E_{11} state dynamics and introduce a method to separate the excited state dynamics from the ground state dynamics; in the second part, I present our investigation results on the photoinduced absorption feature and discuss some possible mechanisms for its origin.

4.1 Excited state dynamics of the (6, 5) SWNTs in pump-probe spectroscopy

4.1.1 Background

Investigation on the SWNT excited state dynamics is important to the understanding of the electronic structure of SWNTs and to their future application. For example, the low quantum yield of semiconducting SWNTs (~1%) [1, 2] suggests that

most excitons on the E_{11} state decay non-radiatively to the ground state. The study of dynamics may reveal the information on the optical dark states below the E_{11} state and the non-radiative decay channels. Understanding of the carrier relaxation process may lead to some techniques to improve the quantum yield and foster the SWNT application in the future.

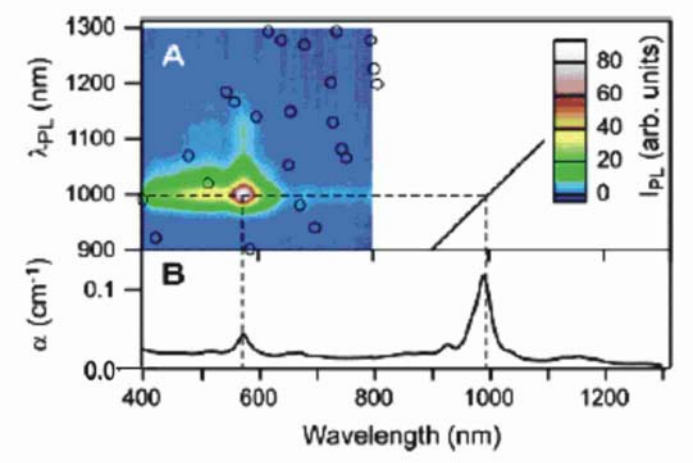

Figure 4.2 (A) Photoluminescence excitation- and (B) ground state absorption-spectra of a (6, 5) enriched nanotube suspension.

A brief introduction of PLE spectra and pump-probe spectra will help to understand the debate in the research field discussed later. Figure 4.2 (A) and (B) show the PLE and the ground state absorption spectra of a fractionation purified (6, 5) enriched sample respectively. The black circles in the top panel indicate the expected positions of spectral features from other tube species. Both the PLE and absorption spectra are dominated by the dipole allowed E_{11} and E_{22} transitions of the (6, 5) tube near 993 nm and 572 nm respectively. Some of the excitons excited to the E_{22} state quickly relax non-radiatively to the E_{11} state and then decay radiatively from the E_{11} to the ground state, the emission of this process is indicated by the bright yellow dot at the intersection of the dashed lines in

the PLE map. The horizontal and vertical streaks from the bright yellow dot are generally considered to be caused by the exciton-phonon interaction. We will discuss these features in more detail in part two of this chapter when we study the transient spectra.

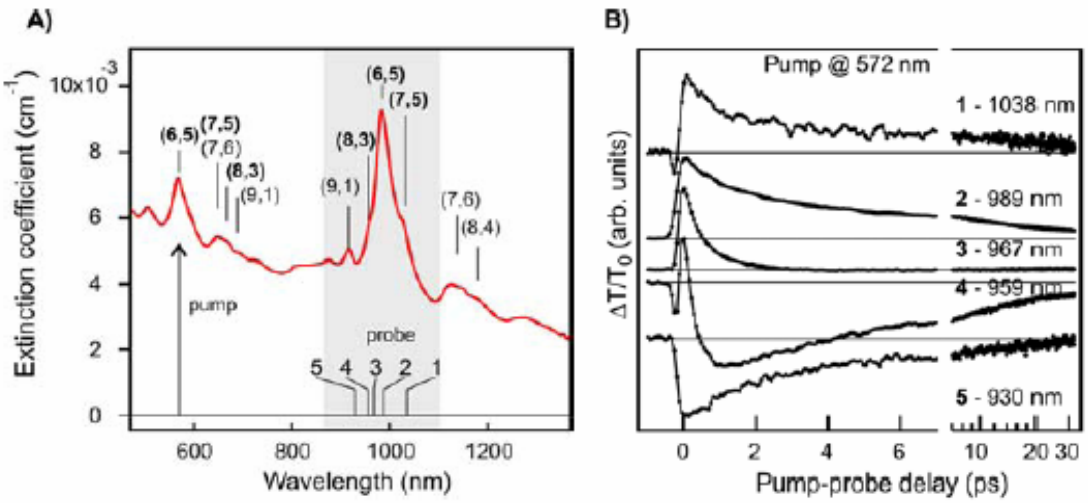

Figure 4.3 (A) Linear absorption spectrum of a CoMoCAT @ SDBS sample. (B) Cross-correlations for resonant excitation of the E_{22} exciton in (6, 5) tubes at 572 nm [3].

Figure 4.3 (A) shows a linear absorption spectrum of a CoMoCAT-SDBS suspension sample and a pump-probe scheme which is to pump on resonance of the E_{22} subband and to probe across the E_{11} subband of the (6, 5) tube. In figure 5.3 (B), the cross-correlations taken at different probe wavelengths exhibit photobleach (PB, positive differential transmission) as well as photoinduced absorption (PA, negative differential transmission) and a superposition effect between the two. The rapid variation of the probe dynamics around the E_{11} state and the carrier relaxation time from the E_{11} state are two essential questions to be answered in this chapter.

Table 4.1 Summary of carrier dynamics in prior reports

Summary of Carrier Dynamics in SWNTs

Referenece	Experiment	Fitting	Time Scale	Publication Date	Note
[4]	PP	mono-exponential	1 ps	2/5/2003	
[5]	PP		<1 ps	1/9/2004	
[6]	PP	bi-exponential	fast: 0.3~1.5ps	3/17/2004	
			slow: 5~20ps		slow component
[7]	PL	mono-exponential	10 ps	4/27/2004	
[1]	PP	bi-exponential	short: 330fs, 2ps	7/1/2004	
			long: 700fs, 120ps		
[11]	PL	mono-exponential	20-200ps	10/31/2005	
[12]	PP	tri-exponential	fast: 0.7ps	11/15/2005	
			int: 2-3ps		phonon
			slow: 50ps		
[13]	PP	tri-exponential		2/9/2006	Auger
[14]	PP	t^(-0.5)		7/26/2006	diffusion
[15]	PL	mono-exponential	20-30ps	12/18/2006	
PP: pump probe; PL: photoluminescence					

Numerous reports on the carrier dynamics in SWNTs can be found and a brief summary of some of them is listed in table 4.1 [1, 4-15]. The review of prior reports will help us to understand what particular aspects we should pay attention to in our investigation. Lauret et al. [4] carried out an early time-resolved study of the carrier dynamics in SWNTs by means of two-color pump-probe experiments and reported a 1 ps time scale for the interband transitions with a mono-exponential fit. Korovyanko et al. also reported a subpicosecond time scale [5]. Shortly after, Ostojic et al. [6] first observed a slow component in the probe signal and extracted the time constants with a bi-exponential fit. The slow component was attributed to the interband recombination and the fast component was explained as intraband carrier relaxation in nonresonantly excited nanotubes. Huang et al. [1] applied a bi-exponential fit in both short (~1 ps) and long time (~50 ps) ranges and obtained two sets of time constants. Chou et al. [12] set the pump wavelength two-phonon energy away from the E_{11} and fit the E_{11} probe signal with a tri-exponential function, the intermediate time constant was attributed to a hot phonon-

absorption process. Huang et al. [13] extracted 3 time constants with 3 exponential functions and emphasized a contribution from an Auger-like exciton-exciton annihilation process in the relaxation dynamics. Russo et al. [14] did a comparison of the fittings from multi-exponential functions and found out that mono-and bi-exponential fittings do not fit the whole range of their signal (~1 ns), a tri-exponential function can fit the whole range of the signal, but the three time constants vary roughly one order of magnitude one after another. They pointed out that it is obvious that a signal can be fitted by using more exponential functions, but such a fitting can unlikely provide physical interpretation in the relaxation process. Instead, Russo et al. found that the signal was fitted very well with a $t^{-0.5}$ function for the whole time range. They attributed this decay to a one-dimensional diffusion limited pair recombination process.

The carrier relaxation dynamics is more consistently revealed from time resolved photoluminescence measurements of semiconducting tubes. Wang et al. [7] reported a 10 ps time scale for the fluorescence emission decay. Hagen et al. [11] found that the lifetime of photoluminescence varies between less than 20 ps to 200 ps from tube to tube and all the signals follow a mono-exponential decay. Hirori et al. [15] reported 20~30 ps lifetime for the fast-decay component of the photoluminescence, and the PL lifetime has a dependence on the local environment surrounding the SWNTs.

The above review of the prior reports shows some debate on the dynamics and time scales on the E_{11} state relaxation, especially in the pump-probe experiments. In the following, we will investigate the carrier relaxation dynamics and time scale of the (6, 5) SWNT with pump-probe experiment and verify some prior interpretations.

4.1.2 Pump power dependence

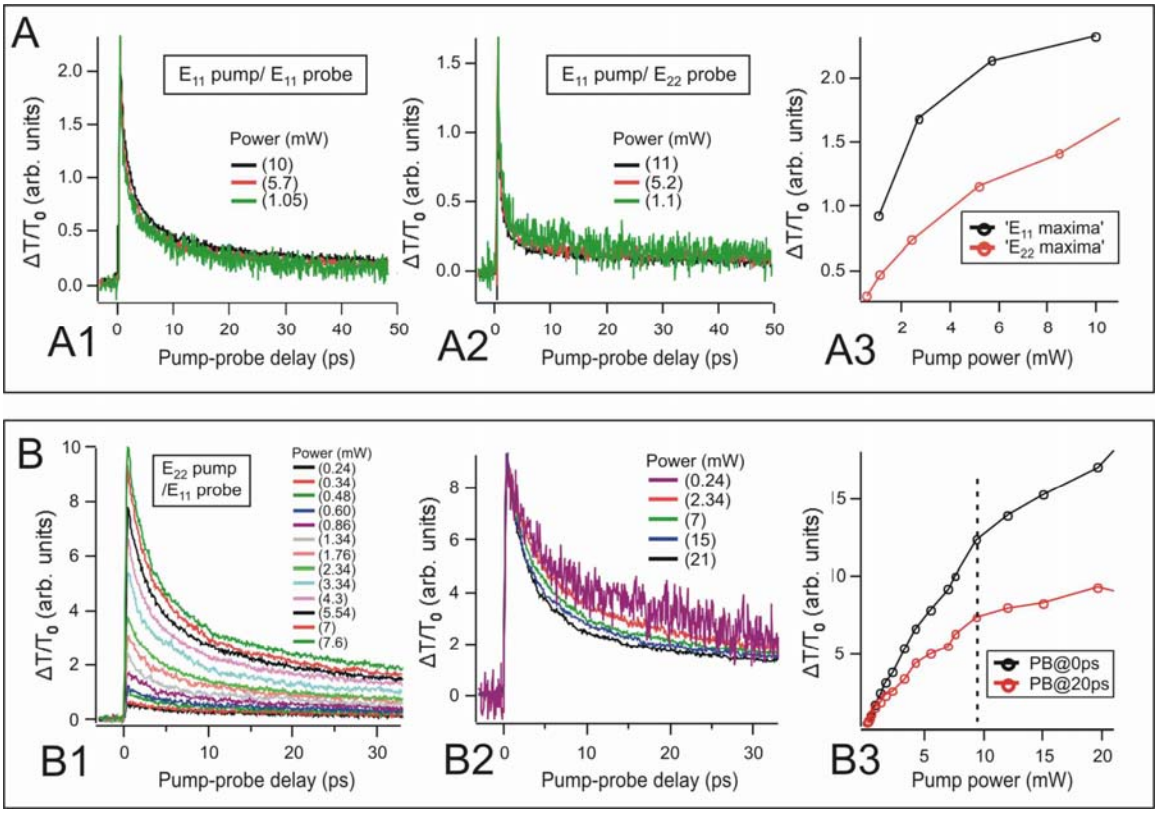

Figure 4.4 Pump power dependence of the E_{11} state relaxation of the (6, 5) tubes. Panel (A) is with the E_{11} excitation. (A1) normalized E_{11} probe signals at different pump powers. (A2) normalized E_{22} probe signals at different pump powers. (A3) dependence of the maximum amplitude of the E_{11} and E_{22} probe cross correlations on pump power. Panel (B) is with the E_{22} excitation. (B1) E_{11} probe signals at different pump powers. (B2) variation of E_{11} probe dynamics with pump power. (B3) pump power dependence of the maximum amplitude at time zero and the amplitude at 20 ps (normalized) of the cross correlations.

Figure 4.4 shows the pump power dependence of the E_{11} and E_{22} probe cross correlations of a (6, 5) SWNT enriched suspension sample. The pump beam was focused to a size of about 100 μm in diameter, with a 250 kHz repetition rate. In panel (A) the pump power of the E_{11} excitation varies by roughly one order of magnitude. The normalized E_{11} and E_{22} cross correlations are closely packed in figure (A1) and (A2), and

the E_{22} relaxation shows a faster decay within the first 10 ps than the E_{11} relaxation. Figure (A3) shows the variation of the maximum amplitudes at time 0 of the E_{11} and E_{22} probe signals with the pump power. The E_{11} probe amplitude shows a clear saturation while the E_{22} probe amplitude is more linear with the power. Figure (A1) and (A2) suggest that the dynamics does not vary much whether the signal is in the saturation region (E_{11} probe) or the linear region (E_{22} probe), with this pump-probe scheme and in this power range.

Panel (B) in figure 4.4 shows the E_{22} pump/E_{11} probe case where the pump power varies by roughly two orders of magnitude. Figure (B1) shows part of the raw data where the signal amplitude continuously increases with the power. Figure (B2) shows the dynamics variation where a trend can be seen that the signal relaxes faster with the pump power. Figure (B3) shows the variation of the cross correlation 0 ps maximum amplitude and the amplitude at 20 ps with the power. For comparison convenience the 20 ps amplitude curve is normalized to overlap with the 0 ps amplitude curve at the lowest pump power. The 20 ps curve saturates quicker than the 0 ps curve, interestingly both curves show a slope change around 10 mW.

A similar trend as that in figure (B2) has also been observed in some prior publications [13] and the fast decay within the first 10 ps was explained partially with an exciton-exciton annihilation mechanism. Although exciton-exciton annihilation may be used to explain some of our observations, for example, that the 0 ps curve saturates later than the 20 ps curve in figure (B3) may due to many particle effect at time zero, the mechanism may not be the dominant factor for the dynamics variation with our purified sample in the above mentioned power range from these observations: first, shown in

figure A, there is no clear trend that the dynamics changes less with power in the saturation region than in the linear region or vice versa; second, shown in figure (A2), when the pump energy (E_{11}) is below the probe energy (E_{22}), we still observe strong signals.

It seems not proper to relate the E_{11} probe signal amplitude directly to the E_{11} state population, because even when the (6, 5) tube is pumped with the E_{11} excitation at very low powers, clear E_{22} probe signals were observed in figure (A2), in this case no population on the E_{22} state should be expected. The signal is later explained to be due to the repopulation of the ground state. But before we get into it, let me present more investigation results on the dynamics with the pump wavelength dependence, which has not been reported in prior publications.

4.1.3 Pump wavelength dependence — pump-probe excitation spectrum

The conventional experiment scheme is to pump and probe resonantly at E_{22} and E_{11} states, as illustrated in figure 4.4 above. Another way to study the dynamics is to pump non-resonantly to see if there is still a probe signal and how the dynamics varies with pump wavelength.

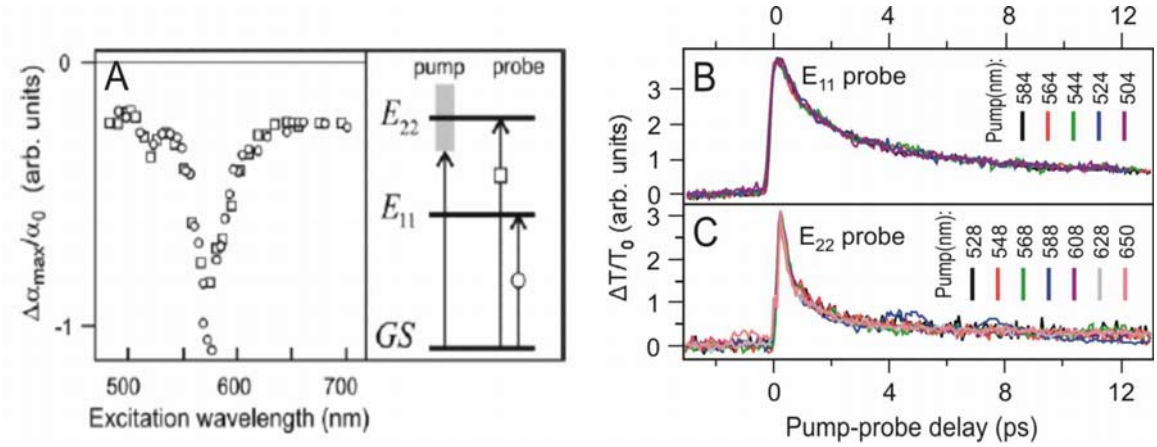

Figure 4.5 Excitation spectroscopy of the (6, 5) SWNT across E_{22} resonance. (A) Dependence of the E_{11} and E_{22} cross-correlation maxima on pump wavelength. (B) and (C) Normalized differential transmissions of the E_{11} and E_{22} cross-correlations with different pump wavelengths respectively.

Figure 4.5 shows the results of pump-probe excitation spectra across the E_{22} resonance of the (6, 5) tube. The experiment scheme is to pump across the E_{22} and to probe at the E_{11} and E_{22} states, shown in the right part of figure 4.5(A). The left part of figure 4.5(A) shows the dependence of the E_{11} and E_{22} cross-correlation $\Delta\alpha_{max}/\alpha_0$ maxima on pump wavelength, where $\Delta\alpha_{max}$ is the maximum amplitude of differential absorbance at time zero. Figure 4.5 (B) shows the normalized E_{11} cross-correlations at different pump wavelengths, figure 4.5 (C) shows the normalized E_{22} cross-correlations at different pump wavelengths, in both figures the signals are plotted as differential transmission.

First we notice that the E_{11} relaxation kinetics is unexpectedly insensitive to the pump wavelengths in the range from 500 nm to 700 nm, as shown in figure 4.5 (B). In some prior reports, the E_{11} probe signal is fitted with a bi-exponential function and the fast exponential decay with a sub-picosecond time constant is attributed to an intraband relaxation [12]. This result suggests that, either the intraband relaxation (from around E_{22}

to E_{11} states) is too fast to be resolved with the time response of our pump-probe setup (~50fs), or the intraband relaxation does not play a big role in the E_{11} probe dynamics.

Second we observe in figure 4.5(C) that when the pump wavelength was tuned to the 650-700 nm range, far below the E_{22} (570 nm) resonance of the (6, 5) tube in energy, strong E_{22} probe signals with the same dynamics were obtained. This result suggests that the probe signal may be dominated by the ground state population instead of the excited state population. When the pump energy is below the probe energy, significantly fewer if not none carrier population should be excited to the probe energy level. Also in figure 4.4 (A2), clear E_{22} probe signals were obtained with the E_{11} pump, but no photo bleach signals were observed at the energy level of the two E_{11} photons, which suggests that exciton-exciton annihilation may not be the dominating factor for the signals with our samples under above mentioned pump fluences. The mostly identical dynamics from on- and off-resonant excitations also suggests that the population on the excited states does not play a significant role in the relaxation of the E_{11} and E_{22} cross correlation signals.

Third we observe that the normalized maxima resonances of the E_{11} and E_{22} probe signals in figure 4.5(A) are quite similar. The E_{11} and E_{22} states are quite different in energy, and the E_{22} probe relaxation is much faster than the E_{11} relaxation, as shown in figure 4.5(B) and 4.5(C). The similarity of the resonances in figure 4.5(A) suggests that the resonance may not directly reflect the nature or dynamics in the E_{11} and E_{22} states, but it may be dominated by some common influence in both the E_{11} and E_{22} cross-correlations. We also notice the small peak around 520 nm in figure 4.5(A), which can be attributed to the phonon G mode of the (6, 5) SWNT from PLE spectra. Exciton-phonon coupling has been observed from the photoluminescence sideband features in the PLE

spectrum [16-18]. Still no pronounced change in the E_{11} or E_{22} relaxation dynamics was observed at this pump wavelength.

The above observations show that to relate the E_{11} or E_{22} probe signal amplitude directly to the exciton population on the E_{11} or E_{22} state is problematic. On the other hand, it is also problematic to simply disconnect the relation between the probe signal amplitude and the excited state population. More investigations are needed to clarify this issue.

The plots in figure 4.5 seem to suggest that the E_{11} or E_{22} relaxation does not change over a 200 nm excitation wavelength range across the E_{22} level. Part of the measurement in figure 4.5 was repeated later with another (6, 5) enriched sample and a slight difference was observed between the dynamics with on and off resonance excitations.

The next step we did was to set the pump at four largely separated wavelengths, 1075 nm, E_{11} resonance (980 nm), E_{22} resonance (570 nm) and 400 nm (close to E_{33} at 350 nm), and to investigate the variation of the E_{11} relaxation in short and long time scales. The results are shown in figure 4.6 below.

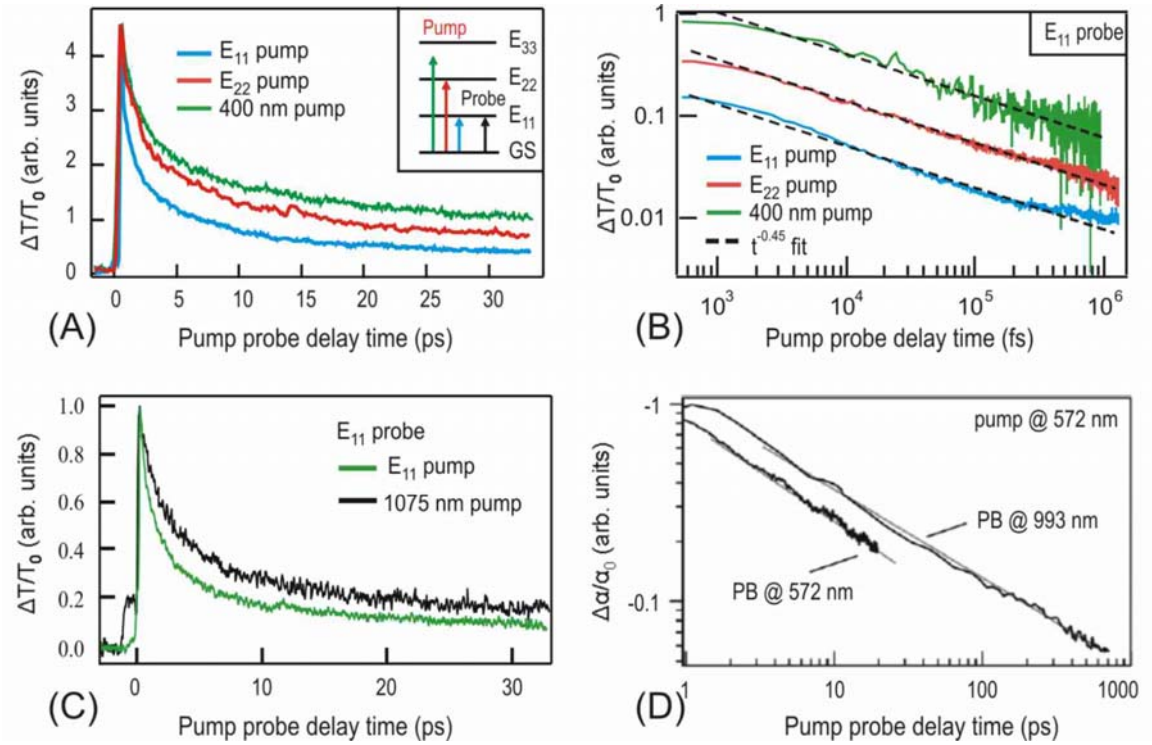

Figure 4.6 Variation of the E_{11} relaxation with largely separated pump wavelengths. (A) Comparison of the E_{11} relaxation from an E_{11} degenerate pump and from an E_{22} and a 400 nm pump in a short time scale. (B) Same as (A) but with a log-log plot in a long time scale, the dashed lines are fittings of a $t^{-0.45}$ function. (C) Comparison of the E_{11} relaxation from an E_{11} degenerate pump and from a 1075 nm pump in a short time scale. (D) Comparison the E_{11} and E_{22} probe dynamics with the E_{22} excitation in a long time scale.

Noticeable difference of the E_{11} relaxation was observed this time. Figure 4.6(A) shows that the initial E_{11} relaxation becomes slower as the pump wavelength was tuned away from the E_{11} resonance to shorter wavelengths. Figure 4.6(B) shows a long time scale relaxation in a log-log plot, in which all the curves are fitted quite well with a $t^{(-0.45)}$ function from a few picoseconds to 200 picoseconds. The deviation of the E_{11} pump/probe signal from the fitting after 200 ps is due to a less perfect alignment of the pump laser beam. Figure 4.6(C) shows that the E_{11} relaxation becomes slower as the

pump was tuned away from the E_{11} to a longer wavelength. Figure 4.6(D) shows that the E_{11} and E_{22} probes follow the same long time relaxation dynamics with the E_{22} excitation.

The long time dynamics in figure 4.6(B) and (D) basically agree with the observation by Russo et al., and was interpreted as the ground state relaxation [14]. The new observation in figure (A) and (C) - the E_{11} relaxation becomes slower as the pump is tuned away from the E_{11} state- has not been reported before. In SWNT pump-probe experiments, the initial motivation to probe an excited state (for example E_{11}) is to get the population information on the excited state. Although the probe dynamics is dominated by the ground state relaxation, the information of the excited state population should be contained in it and it would be nice to separate it form the ground state dynamics. The dynamics variation at the beginning of the signal in figure 4.5 suggests that although the decay is dominated by a diffusion-like process, there may be another mechanism in a short time scale that varies the dynamics, and intuitively this maybe related to the E_{11} state population.

We fitted, as a first approximation, some of the signals in figure 4.6 (fittings not shown here) with two functions, a mono-exponential function with an about 10 ps time constant to take care of the initial variation, plus a $t^{-0.45}$ function that dominates the whole signal. The intuition of this fitting is that we expect the short exponential decay to reflect the dynamics of excitons on the E_{11} state, which has a relaxation time scale of about 10 ps and can be verified by time resolved photoluminescence experiments on the same sample; and we expect the long power law decay to reflect the ground state recovery. The motivation of the fitting is that it may lead to the separation of the two processes from the

cross correlation signals. However, results from data fitting are usually less direct. A more direct method to separate those two processes is discussed in the following section.

4.1.4 Separation of excited state dynamics from ground state dynamics

The experiment scheme in figure 4.4 (A1) and (A2) is to pump at the E_{11} level and to probe at the E_{11} and E_{22} level. Intuitively we notice that the tails of the two probe signals are quite similar while the E_{22} probe signal relaxes noticeably faster than the E_{11} probe signal in the beginning a few ps. As mentioned earlier it is not likely that there are a considerable number of excitons at the E_{22} level in this case, therefore the E_{22} probe signal should reflect the ground state relaxation. The E_{11} probe signal should contain the information of ground state and the E_{11} state population. If we subtract the E_{22} kinetics from the E_{11} kinetics, we may obtain the dynamics of excitons on the E_{11} state.

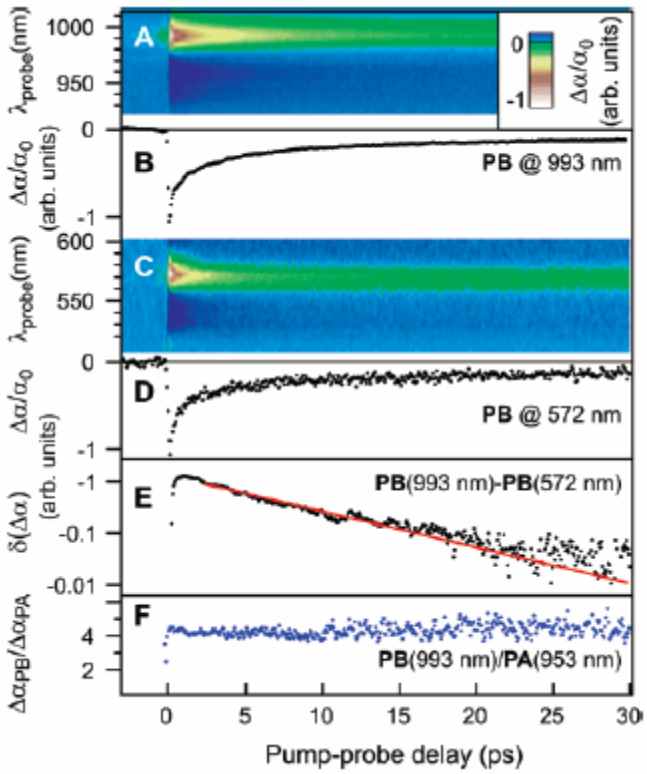

Figure 4.7 Extraction of the E_{11} state dynamics. (A) and (C) spectra transients in the E_{11} and E_{22} wavelength range after resonant excitation of the E_{11} transition. The corresponding on resonant PB dynamics are seen in (B) and (D). (E) The difference of normalized PB transients in (B) and (D) reflects the E_{11} excited state population. (F) The near constant ratio of this transient indicates that recovery of all features is governed by the same mechanism.

Figure 4.7 illustrates the subtraction method and the result. Figure 4.7 (A) and (C) are the spectra transients in the E_{11} and E_{22} regions with the E_{11} excitation of the (6, 5) tube. The probe wavelength was scanned with 4 or 5 nm per step throughout the range. The brown area shows strong photo bleach (PB) signals corresponding to the E_{11} and E_{22} states and the dark blue areas next to the PB features represent photoinduced absorption (PA) signals. Figure 4.7 (B) and (D) show the E_{11} and E_{22} probe dynamics respectively. Figure 4.7 (E) shows the difference of the signals in (B) and (D) when they are normalized at 50 ps. This difference is fitted well by a mono-exponential function with a

6±1 picoseconds time constant. Figure (F) shows the PB to PA ratio in the E_{11} range, in which the PA signal was chosen at the wavelength where it has the maximum amplitude. This mostly constant ratio suggests that the recovery of the both signals is governed by the same mechanism.

The extraction method in figure 4.7 (E) is based on the assumption that almost all the excitons at the E_{11} state are depleted after 50 ps. The E_{11} probe signal after this time delay should reflect the ground state population, not the population at the E_{11}. The E_{22} probe signal reflects the ground state relaxation all the time. The extraction of the E_{22} relaxation from the E_{11} relaxation therefore gets rid of ground state dynamics from the E_{11} probe signal, the difference of the two signals should be a close measurement of the true dynamics of excitons on the E_{11} state.

The time scale of the resulting E_{11} state dynamics agrees with the results from time resolved photoluminescence study of SWNTs [7, 11, 15]. It has been reported that the time resolved photoluminescence (PL) of individual semiconducing SWNTs follows a mono-exponential decay, although the lifetime varies widely from tube to tube [11]. The 6 ps decay time obtained here is close to that obtained from time-resolved PL measurements of SWNT suspension samples [7, 15] where an ensemble-averaged lifetime was revealed.

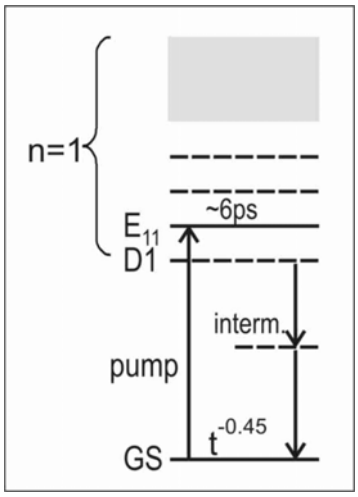

Figure 4.8 Tentative non-radiative relaxation scheme from E_{11} state

Figure 4.8 illustrates a tentative relaxation scheme based on the earlier discussion on the short and long term dynamics. Once excitons are excited to the E_{11} state, most of them decay from the E_{11} state with an about 6 ps time constant. Since the ground state is not recovered with a 6ps time constant, the excitons from the E_{11} state may go to some intermediate states between the E_{11} and the ground state, the relaxation from the intermediate states takes the $t^{-0.45}$ power law, giving rise to the dominant $t^{-0.45}$ ground state recovery dynamics. The possible candidates of the intermediate states are exciton dark states [20-22], defects induced dark states, or phonon coupled states.

There are some possible mechanisms for the power law decay of the probe signal. One mechanism could be a diffusion limited particle-antiparticle annihilation process [19]. The assumption is that, when particles and antiparticles diffuse in a low dimensional system, a particle sweeps out a region of a size proportional to the diffusion length $\sqrt{Dt}$ in time t, meaning that any antiparticle within this region have been probably annihilated. Therefore the volume per particle in d dimension is $(Dt)^{d/2}$, and the particle density is correspondingly $\rho(t) \approx (Dt)^{-d/2}$, for $d \leq 2$ cases. In the semiconducting SWNT

case, two excitons may meet and annihilate each other when they diffuse along the tube. This model predicts the $t^{-1/2}$ decay for the 1D system case.

Another mechanism could be a trapping effect of sub-diffusive particles in one dimension [23]. A standard 1D diffusion process is described with the Fick's second law and the solution shows that the mean square displacement is linear in t, $\langle x^2 \rangle = 4Dt$, where D is the diffusion constant. If there are some trapping centers, the particle's diffusion may be hindered by the trapping centers. We assume that once a particle is trapped, it does not contribute to the particle density any more. In a sub-diffusive process, the mean square displacement is proportional to t^{γ}, where $0<\gamma<1$. The sub-diffusive problem can be described with a fractional diffusion equation and the solution shows that the survival probability (or particle density) is proportional to $t^{-\gamma}$. In the semiconducting SWNT case, defects in the tubes may serve as the trapping centers, and once an exciton is trapped at a defect site, it may decay quickly to the ground state nonradiatively. This model also explains the probe signal power law decay provided γ is equal to 0.45.

A third mechanism for the power law decay of the probe signal could be phonon assisted exciton relaxation, schematically illustrated in figure 4.9. If the electronic states (optical bright or dark alike) are not coupled to the phonon reservoir (thermal bath), the effective life time of the exciton at the E_{11} state may be on the order of 10 nanoseconds at the room temperature [20]. If the electronic states are strongly coupled to the phonon reservoir, as illustrated by the lines connecting the states to the reservoir, then the relaxation of excitons may be coupled to the relaxation of phonons.

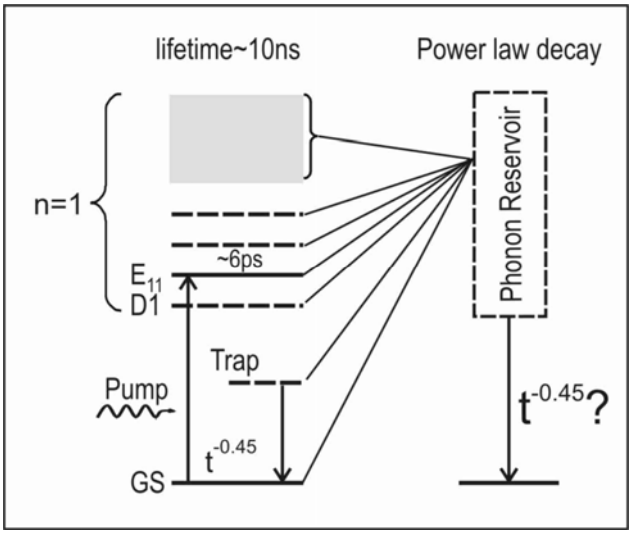

Figure 4.9 Schematic illustration of the influence of exciton-phonon coupling to the carrier relaxation in SWNTs

The idea of phonon assisted exciton relaxation was inspired by the results from a time resolved Raman spectroscopy of thick polymer films, where the Raman mode amplitude decays with a $t^{-0.5}$ power law [24]. It will be very interesting to see if the Raman mode (RBM, G, etc) amplitude of SWNTs decays with the $t^{-0.45}$ power law with our sample or not.

Since the $t^{-0.45}$ kinetics starts very early in our probe signal (see figure 4.6), if the phonon exciton interaction is an important factor in the exciton relaxation, we expect that the generation of phonons in SWNTs is fast. An oscillatory pattern on a photoinduced absorption (PA) cross correlation signal has been observed and explained to be due to the RBM (radial breathing mode) of SWNTs [10]. Because the start of the oscillatory pattern is very early in the PA signal, we estimate that the generation of phonons in SWNTs is almost instantaneous with the excitation of the pump pulse.

A recent theoretical calculation predicts that the multi-phonon decay (MPD) lifetime of localized excitons in SWNTs could be 2~3 orders of magnitude shorter than

the free exciton [36]. An exciton near the E_{11} level may decay non-radiatively to the ground state by simultaneously emitting several optical phonons (G, D modes). Yet the predicted MPD lifetime for small diameter tubes ((6, 5) in our sample) is still too long to explain the very fast relaxation from the E_{11} states. However, the calculation also predicts that the lifetime decreases dramatically as the band gap energy decreases. If the multi-phonon decay is also possible for the phonon modes with smaller energies, like RBM, and the decay may happen between the E_{11} state and some lower exciton dark states [21], the MPD lifetime could be very fast to explain the fast relaxation from the E_{11} state.

The non-radiative decay process in SWNTs is still an unsolved problem so far. All the above mentioned mechanisms need to be verified with further experiments.

In summary, with the two advantages in the SWNT pump-probe spectroscopy - the capability to tune the pump laser wavelength in a wide range and the chirality enriched purified sample, we observe the variation of the E_{11} probe dynamics with different excitation energies, we also observe the dynamics difference between the E_{11} and E_{22} probes with the E_{11} excitation, which was not observed on a polydisperse sample with a similar pump-probe scheme [4]. These new observations inspire us to introduce a method to extract the short time excited state dynamics from the probe signal that is dominated by the long time diffusion dynamics.

4.2 Transient spectra of the (6, 5) SWNTs in pump-probe spectroscopy

4.2.1 Background

The excited state dynamics discussed above studies the system relaxation from dynamics of individual states, while the transient spectrum studies the system relaxation from the dynamics of the whole spectrum. The two approaches have different focuses, yet they combine to produce a whole picture of the one relaxation process.

The pump-probe transient spectrum measures the change of the absorption spectrum when the sample is excited. The most significant change in the SWNT transient spectrum is the photoinduced absorption (PA) features that are not seen in the linear absorption spectrum. The PA feature and its origin is the focus of the debate in the SWNT transient spectrum in recent years. The investigation of PA will provide insights into the carrier-photon interaction in SWNTs and improve our understanding of the photophysics of excitons in quasi 1D material.

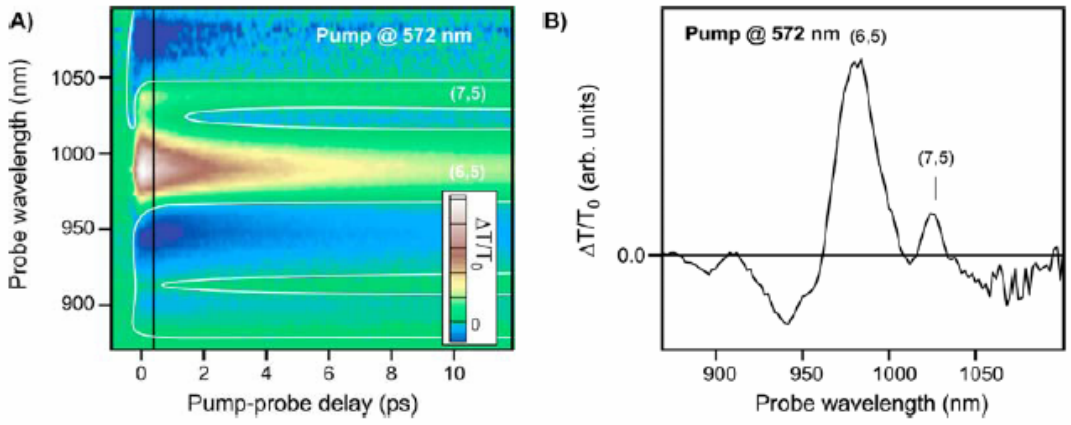

Figure 4.10 (A) False color plot of differential transmission signal as a function of pump-probe delay and probe wavelength of the (6, 5) tube in the E_{11} region for excitation of the E_{22} exciton. (B) Transient spectrum at 0.2 ps pump-probe delay time.

Figure 4.10 shows the typical transient spectrum measurements in our pump-probe experiment. Figure 4.10(A) is a spectrally resolved optical transients, or spectra transients in brief. To record such a spectrum, we set the pump wavelength to 572 nm which is the E_{22} resonance of the (6, 5) tube, and we scan the probe wavelength from about 880 nm to 1100 nm with 5 nm per step. We then integrate the normalized differential transmission cross correlations to make the map. Spectrally resolved optical transients provide a means to visualize the dynamics over a wide range of energies. The brown region has a positive differential transmission and is called photo bleach (PB) signal. The blue region has a negative differential transmission and is called photoinduced absorption (PA) signal. A vertical cut of the map at 0.2 ps gives a transient spectrum shown in figure 4.10(B), which provides a spectrum taken 0.2 ps after the pump pulse excites the sample. The photo bleach peaks of the (6, 5) and the (7, 5) tubes in figure 4.10(B) correspond to their E_{11} peaks in the linear absorption spectrum. Interestingly, there are some valleys or negative transmissions in figure 4.10 (B) too, which are induced absorption signals corresponding to the blue regions in figure 4.10(A). The origin of the induced absorption feature was still in debate by the time I started writing this dissertation.

Table 4.2 Summary of PA observations in prior reports

Summary of Photoinduced absorption observation in SWNTs

Referenece	Observation	Interpretation	Publication Date
[4]	nonresonant probing	globe red shift of π-plasmon resonance	2/5/2003
[5]		transitions between subbands	1/9/2004
[25]	time dependent blue shift		12/18/2004
[28]	theoretical prediction	red-shifted PA peaks due to biexcitons	1/25/2005
[8]		carrier-induced peak broadenings	3/8/2005

Prior investigations on the PA with the pump-probe experiment provide controversial interpretations [4, 5, 8, 25-28], some of them are summarized in table 4.2. Lauret et al. [4] observed the PA at nonresonant probe wavelengths and attributed it to a global redshift of the π-plasmon resonance; Korovyanko et al. [5] attributed the PA to transitions between bright exciton subbands; Styers-Barnett et al. [25] observed a time dependent blue shift of the PB and PA with a film SWNTs sample; Ostojic et al. [8] attributed the PA to the carrier-induced absorption peak broadening after excitation; and Pedersen et al. [28] predicted in a theoretical calculation that there would be a red-shifted PA due to a bi-exciton complex. All of the above mentioned experiments were done with polydisperse SWNT samples. Pedersen et al. [28] explained that there were two considerations that led to their theoretical calculation to predict pump-probe transient spectrum: first, it was not available then to obtain an E_{11} pump with a spectrally resolved probe; second, it was not available to obtain chirality enriched isolated SWNT samples. When we started our investigation, we had both capabilities and expected a better observation.

4.2.2 Pump power and wavelength dependence

The biggest obstacle in studying the transient spectrum of SWNTs in pump-probe spectroscopy from polydisperse samples is the uncertainty of the interferences among features from different tube species. This is perhaps one of the reasons that lead to the debate in the transient spectrum. In some sense, the detail of the observation is limited by the purity of the sample. In this investigation, we mainly use a DNA wrapped and a sodium cholate (SC) dispersed (6, 5) SWNT enriched samples. The preparation of the

DNA wrapped (6, 5) tube sample is presented elsewhere [29, 30]. The SC dispersed sample was prepared following a similar procedure as in reference [29], with CoMoCat soot as the raw material, SC as the surfactant, and iodixanol as the density gradient medium.

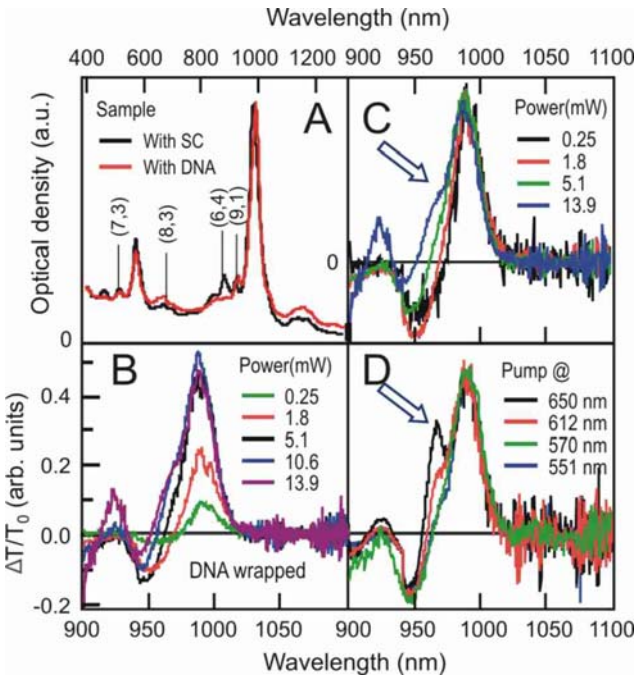

Figure 4.11 Pump power and pump wavelength dependence of transient spectrum in the E_{11} region of the (6, 5) tube. (A) Linear absorption spectra of the DNA wrapped sample and the SC dispersed sample. (B) Pump power dependence of the transient spectrum of the DNA wrapped sample. (C) Normalized spectra of those in (B). (D) Pump wavelength dependence of the transient spectrum of the DNA wrapped sample, spectra are normalized.

The pump power dependence of the transient spectrum of the DNA wrapped sample is shown in figure 4.11. Figure 4.11(A) shows the normalized linear absorption spectra of the two (6, 5) SWNT enriched samples. In both spectra, features from the (6, 5) tube (E_{11} at 990 nm, E_{22} at 570 nm) dominate. The DNA wrapped sample was the most highly enriched sample used for the experiments in this dissertation, however, its optical

density was too low for recording a low noise transient spectrum in the E_{22} region; the SC dispersed sample had a sufficient optical density, but it contained more minority tube species indicated in the figure 4.11 (A).

Figure 4.11(B) shows the pump power dependence of the transient spectrum taken at 1 ps pump-probe delay time, with pump wavelength set at the E_{22} resonance of the (6, 5) tube. The photo bleach (PB) peak is near 990 nm and the induced absorption (PA) valley is around 950 nm. The PB amplitude of the (6, 5) tube saturates at about 5 mW, while the PB of the E_{11} of the (9, 1) tube near 920 nm continues to grow with power and become very pronounced at 13.9 mW.

Figure 4.11(C) shows the normalized spectra. We notice that the position of the PB peak at 990 nm does not move with power. The stability of the PB position under high excitation energies has also been reported with ploydisperse SWNT samples [8]. On the other hand, the position of the PA peak moves to the higher energy side and the PA/PB peak ratio decreases with the power. We tend to attribute these changes to the interference by the PB of the (9, 1) tube at 920 nm. We also notice that there is an abrupt slope change near 960 nm in the transient spectrum at 13.9 mW pump power, which causes the apparent FWHM of the PB peak at 990 nm to increase (blue trace in figure 4.11(C)).

To verify the slope change near 960 nm, we did a pump wavelength dependence of the transient spectrum of the same sample, shown in figure 4.11(D). When the pump wavelength was tuned to 650 nm (near the E_{22} of the (8, 3) tube), a clear PB peak appeared at 960 nm, which corresponds to the E_{11} of the (8, 3) tube. This analysis suggests that the variation of the FWHM of the (6, 5) PB peak is affected by the PB of

different tube species in the sample, and a PB peak in the transient spectrum has a superposition effect of the PBs from several tubes which may saturate successively with pump power. We also notice that the PA position and the PA/PB peak ratio do not vary with pump wavelength as much as with pump power.

In all these measurements the amplitude of the PB is always larger than the amplitude of the PA for the (6, 5) tube, irrespective of pump power and pump wavelength. The analysis from the results in figure 4.11 clearly shows the subtlety to identify and quantitatively evaluate the true features from one tube species even with a purified chirality enriched sample, because the features of minority tube species always interfere with those of the majority species. It suggests that in order to minimize the interferences from minority species, it is necessary to pump on resonance of the exciton states of the majority tube with an appropriate low power. The analysis also serves as a guide to identify features in other energy regions in the transient spectrum.

4.2.3 Spectra transients with resonant excitations of the E_{11} and E_{22} states

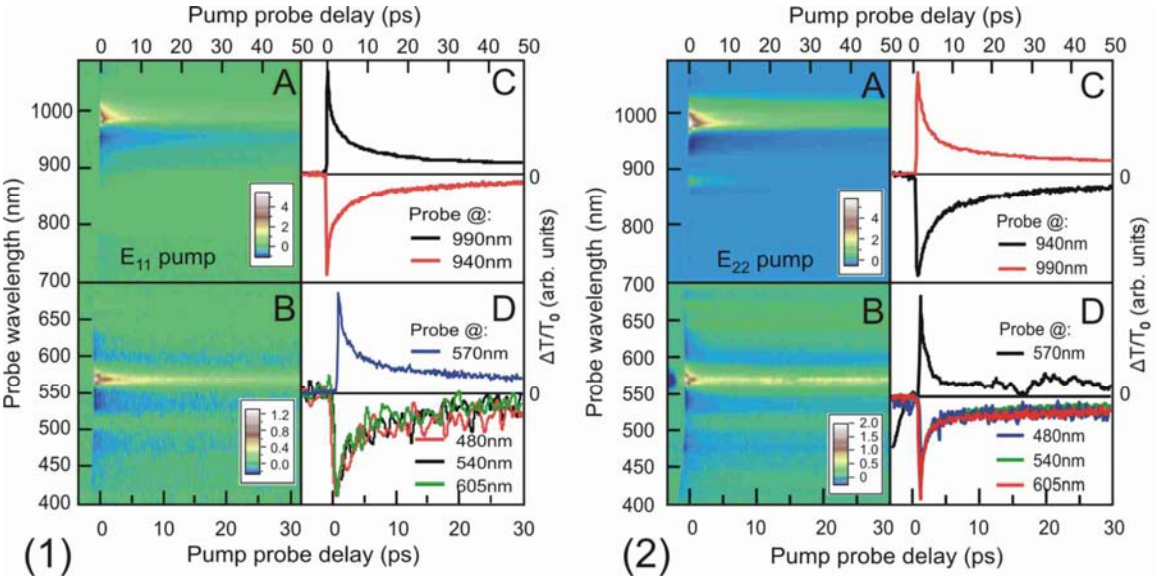

Figure 4.12 Spectra transients with the (1) E_{11} pump and (2) E_{22} pump. In both figures, (A) Probe wavelength scans from 700 nm to near 1100 nm. (B) Probe wavelength scans from 400 nm to 700 nm. (C) Dynamics comparison of PA and PB in the E_{11} region. (D) Dynamics comparison of PA and PB in the E_{22} region.

Encouraged with the observations in the transient spectra in the E_{11} region presented in figure 4.11, we wanted to investigate more features in a wider spectral range. Then we made spectra transients with the SC dispersed sample, shown in figure 4.12 (1) and (2). To make these spectra transients, we developed a Labview VI that can automatically select the probe wavelength through a spectrometer, maintain the transmission signal strength T roughly the same by adjusting the slit width of the spectrometer, and measure and record the probe signal. It greatly reduces the measuring time, the reliance on the stability of the laser system, and the chances for human errors.

Figure 4.12 (1) was made with the pump wavelength tuned to the E_{11} resonance of the (6, 5) tube; figure 4.12 (2) at E_{22} resonance. In both figures the probe wavelength was scanned from 400 nm to near 1100 nm with 5 nm per step. In (A) the cross correlation

runs up to 50 ps, and in (B) up to 30 ps. The color scale shows the relative amplitude of differential transmission in arbitrary units.

Qualitatively the main features in the both spectra transients are similar. In (A) in the E_{11} region, there are a PB feature around 990 nm and a blue shifted PA feature around 940 nm, consistent with our observations in figure 4.11. In (B) in the E_{22} region, there are a PB feature around 570 nm (E_{22} of the (6, 5) tube), a red shifted PA feature around 605 nm, and two blue shifted PA features at 540 nm and 480 nm with a gap at 510 nm. We tend to consider that the PA at 605 nm is associated with the PB at 570 nm, because in thus prepared samples (with density gradients) the PB amplitude may be considerably larger than the amplitude of PA of the same tube species irrespective of pump power and pump wavelength, and there is no large PB amplitude around 605 nm other than the PB at 570 nm. Weak features from minority tube species can also be seen in the both maps, while they are more pronounced with the E_{22} pump than with the E_{11} pump, for example in figure 4.12 (2), two PB features near 650 nm and PB and PA near 880 nm can be identified.

To investigate the association of the PA features and their nearby PB features, we compared the typical dynamics in those regions. By typical I mean the dynamics at the center of the PA and PB regions in the spectra transients. The dynamics varies inside both regions and shows a clear superposition effect during the transition from PB region to PA region, which we will discuss in detail later. As shown in figure 4.12 (1) and (2) (C)s and (D)s, in general the dynamics of the PA features are similar to that of the nearby PB. In figure 4.12 (2) with the E_{22} pump, the probe signal at the E_{22} region (subfigure (D)) relaxes much faster than that near E_{11} region (subfigure (C)), suggesting that many

excitons decay within a very short period of time from the E_{22} state after the excitation. On the contrary, in figure 4.12 (1) with the E_{11} pump, PA and PB dynamics in the E_{11} and E_{22} region are more or less the same. Detailed comparison of the E_{11} and E_{22} PB dynamics with the E_{11} pump and an explanation for the clear photo responses at E_{22} region when pumping at the E_{11}, has been discussed in the first part of this chapter. In brief, the change of probe signal is affected by the change of particle population in the ground state and the excited state that is associated with the probe wavelength. In a textbook two level system, the ground state population changes at the same rate as the excited state population, because particles cannot go anywhere else if we neglect the particle transition time between the two states. But in real systems, for example in a carbon nanotube, several levels with different natures may be involved in the relaxation process. There are cases when charged particles are trapped in some other states, the ground state population is not recovered and yet there is no population at the excited state. In these cases, pumping at a lower level and probing at a higher level, we may still be able to see photo responses due to non-equilibrium ground state population.

None of the previous interpretations on the origin of PA in the pump-probe transient spectrum can very well explain our observations shown in figure 4.12. Lauret et al. [4] attribute the PA to a global redshift of the π-plasmon resonance which should lead to PA only on one side of PB, but we observe PA on both sides of the PB in the E_{22} region. Korovyanko et al. attributed PA to transitions between the bright exciton states [5], however, the transition energies do not match the positions of PA in our data, and the exciton life time at E_{11} state is estimated very short (~30 ps) from time resolved photoluminescence study [7, 15], yet the PA signal lasts for ns in our measurement.

Styers-Barnett et al. observed a time dependent blue shift of PB and PA in a film sample [25], while no noticeable shift of the PA or PB has been found with time with our SWNT suspension samples. Ostojic et al. attributed PA to the broadened absorption spectrum after excitation [8], the assumption does not explain why PAs are found on both sides of the E_{22} but only on one side of the E_{11}, and why blue shifted PAs are far from symmetric around the E_{22}. Pedersen et al. predicted a red shifted PA due to the formation of a biexciton complex [28], but we observed even more pronounced blue shifted PA features. These reports show how different samples and pump-probe schemes lead to varying interpretations of the observed signatures in the transient spectrum.

4.2.4 Origin of the induced absorption-phonon assisted carrier scattering to the E_{ii} states

We were puzzled with the new observations for a while until the features in the PLE map of the sample caught our attention and inspired us for a new interpretation of the origin of the PA- phonon assisted carrier scattering to the E_{11} or E_{22} states.

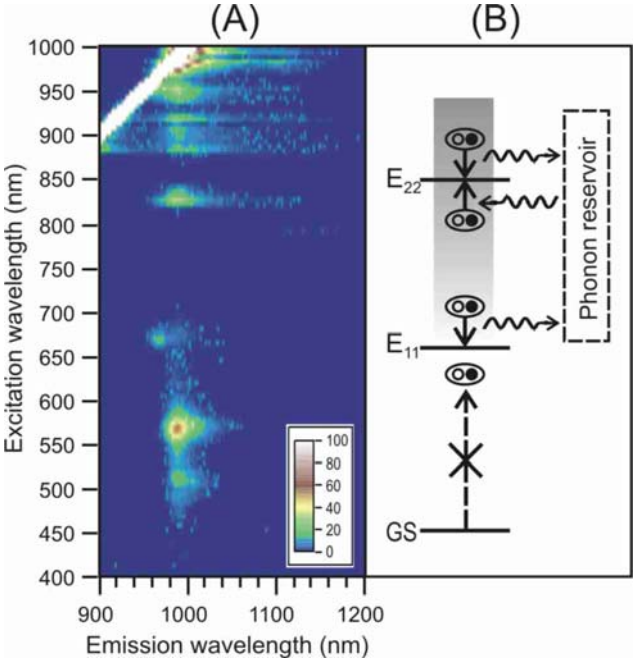

Figure 4.13 (A) PLE map of the SC dispersed sample. (B) Schematic of the mechanism of the PA in the transient spectra.

Figure 4.13 (A) shows the PLE map of the SC dispersed sample that was taken with an FL3-111 spectrophotofluorometer (Jobin Yvon/Horiba Fluorolog-3). The excitation wavelength scans from 400 nm to 1000 nm with 5 nm per step. Pronounced features are shown aside from the dominant features at the E_{11} and E_{22} excitation. These features have been studied in detail and have been explained by phonon assisted processes in previous reports. Chou et al. attributed the strong PL emission spots to one or two phonon modes, the horizontal streaks and vertical stripe of the continuous emission to phonon emission and absorption in thermally excited processes [17]. F. Plentz et al. associated the G band in PLE map to an exciton-phonon bound state, supported by the broad line shape of PLE profile at this energy [18]. H. Htoon et al. studied low temperature, single nanotube PLE spectroscopy, and found combination

modes besides specific phonon modes [16]. All these reports strongly suggest that the sideband features in PLE map are phonon associated.

By comparing figure 4.13 (A) with figure 4.12, we find that the PA features in the spectra transients are in unexpected agreement with the phonon sideband features in the PLE spectrum in terms of position and amplitude. In the E_{11} region, both features extend from the E_{11} to about 900 nm, with the most pronounced amplitude near 950 nm, which corresponds to the radial breathing mode (RBM) of the (6, 5) tube. In the E_{22} region, both features extend on both sides of the E_{22}, and the features on the blue side extend farther. We also notice that there are some discrepancies between the two types of features around 510 nm and 830 nm, where pronounced phonon sideband features appear in the PLE spectrum but no corresponding PA features appear in the spectra transients. By closely examining the absorption spectrum in figure 4.11, we tentatively attribute the vanishing of the PA of the (6, 5) tubes in those two positions to the E_{22} PB of the (7, 3) tubes (~510 nm) and the E_{11} PB of the (5, 4) tubes (~830 nm) contained in the sample.

In figure 4.12 (B)s, the PA feature on the blue side of the E_{22} is more pronounced than that on the red side, this also supports that the PA may be a phonon assisted process, because the general understanding is that it is easier for a charged particle to give off phonons to the lattice than to absorb them from the lattice. However, there is still one puzzle left, which is why there are PAs on both sides of the E_{22} state but only on one side of the E_{11} state. To address this issue, it is helpful to revisit the electronic band structure and density of states of the (6, 5) tube by the tight binding model. We are aware that the tight binding model applies to the one particle picture, and the two photon PLE experiment results suggest the exciton nature of charged particles in SWNTs [31, 32].

The reason we use the tight binding model here is because it is well established, it is easier to use it to illustrate the idea first, and then convert it to the exciton picture.

Shown in the reference figure r1(2) [33], one major difference between the band structures at Van Hove singularities c1 and c2 is that there is no bands below c1, but there are bands and non zero density of states below c2. A simplified band structure is shown in figure r1 (1). Our assumption of the PA process is as follows, first charge carriers as well as phonon modes are excited after the pump pulse hits the sample, the depletion of the carrier from the E_{22} and E_{11} states are fast (<50 ps) but the cooling down of the phonon modes may last long (>1 ns). Then the probe pulse comes, carriers excited by the probe pulse to the bands near c1 and c2 singularities are now easier to be scattered to c1 or c2 due to the existent of phonon modes and the coupling between carriers and phonons. In principle the carriers can also be scattered out of the c1 or c2 if there are sufficient number of carriers in c1 and c2, the fact we don't see PB features around the E_{11} or E_{22} states suggests that the probability for carriers to be scattered out of the E_{11} or E_{22} states are negligible compared to the probability to go into these states, this may due to the huge oscillator strength of the Van Hove singularities and may be a special property of 1D material. Near c2, carriers can be excited to bands below c2 and be scattered to c2 by absorbing a phonon (or phonons), this process is indicated as (B) in the figure which corresponds to the red shifted PA near the E_{22}; carriers can also be excited to bands above c2 and be scattered to c2 by emitting a phonon (or phonons), this process is indicated as (C) in the figure which corresponds to the blue shifted PA near the E_{22}. While near c1, carriers can be excited to bands above c1 and relax to c1 by emitting phonons, this process is indicated as (A) in the figure which corresponds to the blue

shifted PA at the E_{11}. Since there are no bands below c1, the probability for the optical excited carrier to stay and to interact with phonons at a state below c1 is negligible. This may be the reason there is no red shifted PA at the E_{11}. Also in figure r1, band edge transitions indicated by processes (D) and (E) correspond to the E_{11} and E_{22} PBs in the spectra transients.

To convert the above argument to the exciton picture is straightforward. Shown in figure 4.13 (B), the carrier density of states right below and above the E_{22} is not zero, an optical excited carrier can go to the bands below and above the E_{22}, interacts with phonons there, and be scattered to the E_{22}, causing red and blue shifted PAs in the spectra transients respectively. The carrier density of states below the E_{11} is essentially zero. An optical excited carrier can only go above the E_{11} and interact with phonons there. So we don't see red shifted PA near the E_{11}. Theoretical calculation predicts non-zero carrier density of states above the E_{11} in the (8, 0) SWNT [34], which is consistent with this hypothesis.

The above hypothesis suggests that in general electron (exciton)-phonon interaction may not happen in the forbidden band in a semiconductor. The sideband features in the PLE map are due to the interaction between the phonon modes and the existing electronic states. The electronic states exist there irrespective of the existence of phonons. It is not accurate to consider these states anything new or as an outcome of exciton-phonon interaction. It may be just the interaction with pronounced phonon modes that make these states pronounced.

Also according to this hypothesis, the PA and nearby PB share a common decay channel from an E_{ii} state to ground state. We would expect them to have a similar

dynamics, especially when there are no excitons coming from a higher E_{ii} level. However, we found that the dynamics are usually in constant variation in the spectra transients. We compare the dynamics in the E_{11} region in detail in the next section.

4.2.5 Variation of probe dynamics and transient spectrum narrowing effect

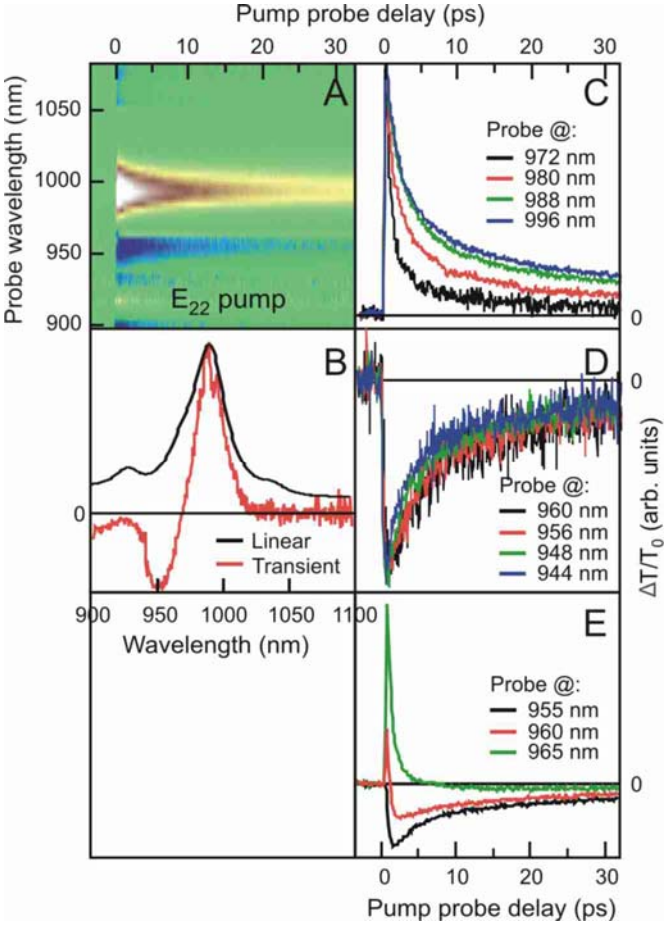

Figure 4.14 Dynamics variation and transient spectrum narrowing effect in the E_{11} region. (A) Spectra transients of the DNA wrapped sample with the E_{22} pump. (B) Comparison of linear absorption- and transient- spectra of the DNA wrapped sample. (C) Variation of dynamics within the PB region in (A). (D) Variation of dynamics within the PA region in (A). (E) Variation of dynamics in the PA to PB transition region from the SC dispersed sample.

Figure 4.14 (A) is the spectra transients of the DNA wrapped sample with the E_{22} pump, the probe wavelength scans with 4 nm per step. The PB and PA features of the (6, 5) tube are similar to that in figure 4.12 (A)s. The PB of the (9, 1) tube at 920 nm can be identified. Figure 4.14 (B) shows that the transient spectrum is clearly narrower than the linear absorption spectrum of the DNA wrapped sample. Figure 4.14 (C) shows the dynamics variation from the center of the PB region towards the spectral range of the PA and PB. A trend can be seen that the signal decays faster as the probe wavelength moves towards the spectral range. Figure 4.14 (D) shows the dynamics variation within the PA region. We notice that it is more stable than that in the PB region. To be more specific, there is no rapid change of the PA dynamics near the spectral range of the PA and PB region. The dynamics variation through the PB to PA transition is shown in figure 4.14 (E) with the SC dispersed sample, because the signals of the DNA wrapped sample were too noisy in this region. Readers may notice that the dynamics of the same probe wavelength do not match in figure 4.14 (D) and (E). The reason is that different surfactants used in the two samples cause the spectra to shift by a few nanometers. Clear superposition effect of the PA and PB can be seen in this region. The 960 nm probe signal shows that the PB takes place shortly before the PA in this case.

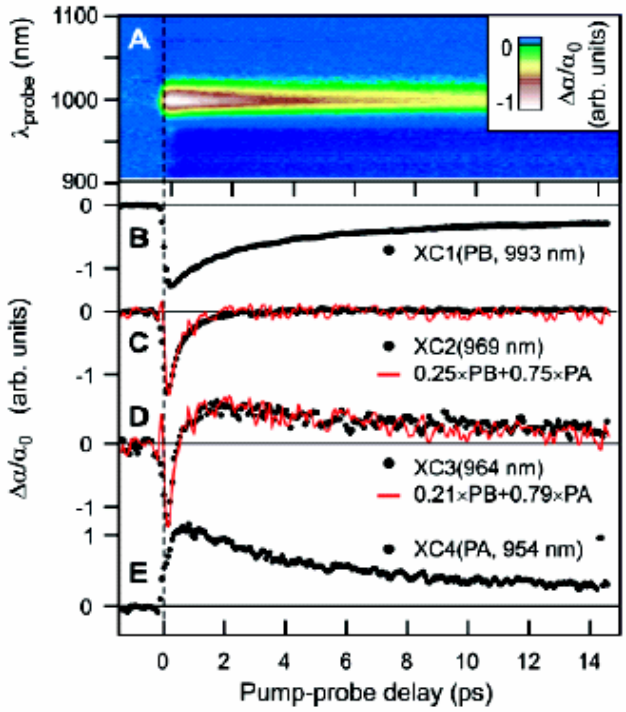

Figure 4.15 (A-E) Wavelength dependence of the E_{11} transients after excitation of the E_{22} exciton. (B-E) Traces at wavelengths intermediate to those at the PB and PA extrema can be described by an incoherent superposition of PB and PA signals.

The superposition effect near the spectral range of the PB and PA is examined in detail in figure 4.15. The signal in figure 4.14 is differential transmission; the signal in figure 4.15 is differential absorption. Nevertheless the dynamics are the same. Cross correlation XC1 in subfigure (B) is the PB signal with the maximum amplitude. Cross correlation XC4 in subfigure (E) is the PA signal with the maximum amplitude. Intermediate cross correlations are fitted well with a superposition of XC1 and XC4 as shown in subfigure (C) and (D). These signals were taken on the DNA wrapped (6, 5) SWNT sample and the cross correlation signal in figure 4.15 (D) is more noisy than that in figure 4.14 (E). Nevertheless, the superposition trend through the PB to PA transition stays the same irrespective of different surfactants used.

In figure 4.14 (E) the 960 nm probe shows that the PA takes over the signal after the PB, which can also be explained with our hypothesis mentioned earlier. If the PA is due to carrier scattering to the E_{11} state by carrier-phonon coupling, then there should be at least two factors that affect this scattering efficiency. One is the population of phonon modes, if there is no phonon then there is no PA. Another is the carrier population on the E_{11} state, if the population on E_{11} state has already reached saturation limit, then there should not be PA either. As for the 960 nm probe in figure 4.14 (E), we can imagine that there is a considerable population on the 960 nm state at the beginning of the relaxation, therefore the scattering efficiency is low and the PB dominate the beginning part of the signal. After a few ps the population decreases significantly, and the scattering efficiency prevails, then the PA takes over. If this is true, then the PB lifetime in the cross correlation trace where PA and PB co-exist may be a rough estimation of the carrier life time on that state. For example the lifetime at 960 nm state should be at least 1.5 ps, and that of the 965 nm state at least 5 ps, measured roughly from figure 4.15.

The PB-PA superposition effect suggests that the two processes compete with each other. One question rises, why does the dynamics vary more rapidly in the PB region than in the PA region in figure 4.14? This has not been reported so far and no current theory can readily explain it.

One possibility is that there are some phonon modes with a less energy than the RBM mode interacting with excitons inside the PB region. At the spectral range of the PA and PB where PB amplitude gets weaker, the PA from these modes gets pronounced and changes the dynamics greatly. While PB signal is centered at the E_{11} and does not extend that much into the PA region, so the superposition effect inside the PA region is

not that pronounced. Phonon density of states of SWNTs has been studied by inelastic neutron scattering method, and considerable density of states below RBM mode energy has been reported [35]. While previous reports on phonon-exciton interaction are more focused on pronounced individual modes or combinations of them [16-18], we estimate that the PA may come from continuous phonon modes in our experiment setup, while pronounced individual modes (RBM, G, etc.) give rise to pronounced PA features in the spectra transients.

The PB-PA superposition effect also helps to explain the narrowing of the transient spectrum in figure 4.14 (B), in which the transient spectrum is narrowed more on the blue side where the PA exists. There may be two effects that contribute to the narrowing. One, the superposition near the spectral range of the PA and PB causes the PB to reduce to zero quicker; the other, the (6, 5) tube E_{11} peak in the linear absorption spectrum maybe broadened by the E_{11} of the (8, 3) tube and other tube species like the (7, 5) tube. When the (6, 5) tube is excited on resonance, the transient spectrum is dominated by the E_{11} PB feature of the (6, 5) tube while the PB features from other tubes are greatly suppressed.

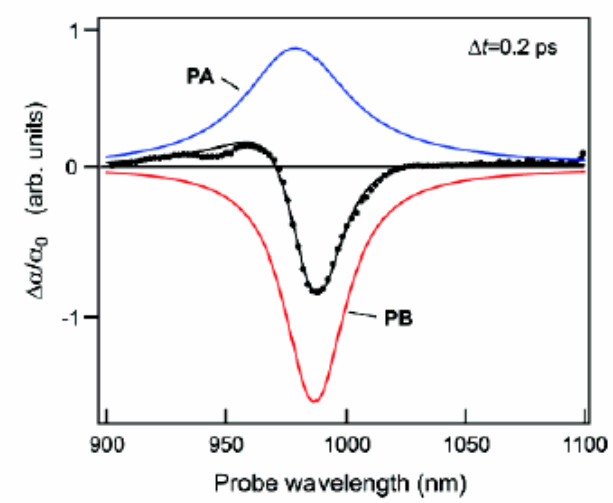

Figure 4.16 Transient spectra can be decomposed into a superposition of a PB and PA Voigt profile.

Last but not least, the assignment of the redshifted PA near the E_{22} state of the (6, 5) tube in figure 4.12 is based on the assumption that the PB amplitude is much larger than the PA for the sample. This has not been carefully verified with that sample due to time constraint. In the next section we will see in some samples the PA has comparable amplitude as the PB. If the PA near the E_{22} is not associated with the E_{22} of the (6, 5), then there exists another possibility that the transient spectrum is a superposition of the PB and an overall PA effect, shown in figure 4.16. The PB profile is centered at 993nm relating to the E_{11} state of the (6, 5) tube. The PA profile is centered at 987nm ± 2nm. The superposition of the two yields a close fit to the transient spectrum. This analysis suggests that the PA signal may come from an optical transition that is blue shifted compared to the E_{11} state. A lot more experiments are needed to verify all the hypotheses proposed in this section.

4.2.6 Investigation on the PA/PB ratio

One good way to verify the above mentioned hypothesis is to investigate the PA/PB amplitude ratio. A pump power dependence shows that the PB and PA amplitudes follow the same trend with the power (data not shown here), and the rough comparison of the PB and PA dynamics in figure 4.12 suggests that they have the same dynamics. A good way to examine the subtle difference between PA and PB is to look at the ratio of them. This investigation is not complete yet due to time constraint but there are already some very interesting results.

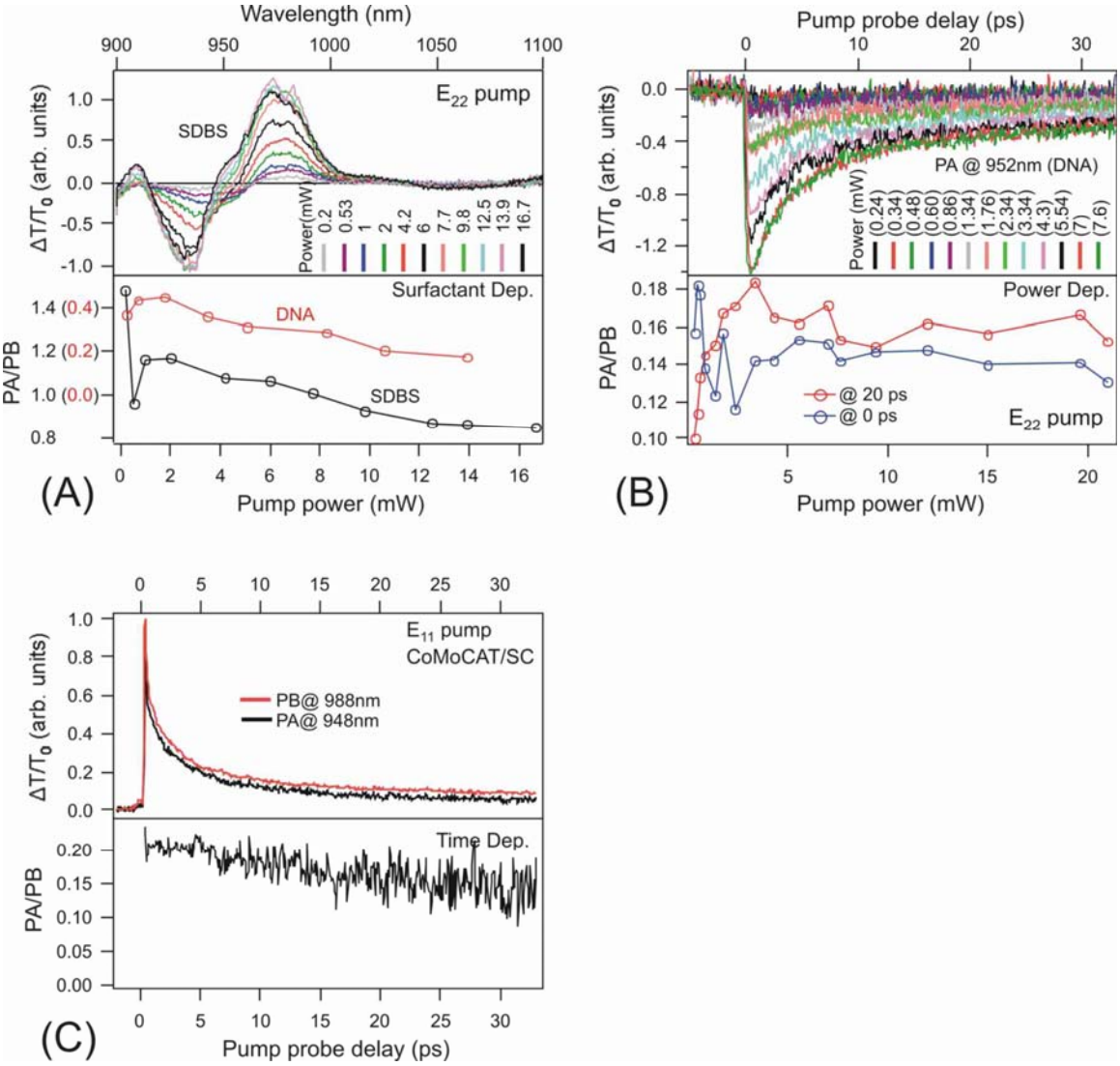

Figure 4.17 Investigation on PA/PB ratio. (A) Comparison of the PA/PB ratio from a SDBS dispersed (6, 5) enriched sample and the DNA wrapped sample. (B) Pump power dependence of the PA/PB ratio of the DNA wrapped sample. (C) Time dependence of the PA/PB ratio from a SC dispersed (6, 5) enriched sample.

Figure 4.17 (A) upper figure shows the pump power dependence of the transient spectra of a SDBS surfactant dispersed (6, 5) SWNT enriched sample with the E_{22} excitation taken at about 1 ps pump-probe delay time, this sample did not go through the density fractionation purification process. The lower figure shows the PA/PB ratio of the SDBS dispersed sample (scale: 0.8~1.4) and the DNA wrapped sample (scale: 0.0~0.4),

the transient spectra of the DNA wrapped sample is shown in figure 4.11 (A). The SDBS dispersed sample has a much higher PA/PB amplitude ratio than the DNA wrapped sample, and at low powers the amplitude of the PA is even bigger than that of the PB in this sample. This may imply that upon same excitation the number of phonons generated is strongly dependent on the environment surrounding the tube.

In figure 4.17(B), the upper figure shows the PA cross correlations at different pump powers on the DNA wrapped sample, the corresponding PB cross correlations are shown in figure 4.4 (B1). The lower figure shows the PA/PB ratio of the 0 ps amplitude and the 20 ps amplitude. The 20 ps trace shows a clear trend that the PA/PB ratio initially increases with power and reach saturation around 3 mW. The slow decrease of the ratio thereafter may due to PB interference from other tubes (for example the (9, 1) tube). This may be explained as that it needs some power to excite the phonon modes and establish the phonon carrier coupling. However, the 0 ps trace shows an opposite trend at the beginning. We are not certain about this difference by now, but we estimate that the 0 ps amplitude is probably affected by a coherent effect which will be shown in chapter 5. Readers may also notice that the PA/PB ratio of the same DNA wrapped sample does not match in figure 4.17(A) and (B), the reason is that the data in figure 4.17(B) were taken roughly two months after the data in figure 4.17(A) were taken, the apparent decrease of the PA/PB ratio may suggest that the formation small bundles in the sample over time impedes the generation of phonons. More experiments can be done to verify these uncertainties.

In figure 4.17(C), the upper figure shows the comparison of the PB and PA dynamics of a SC dispersed (6, 5) enriched sample. Both cross correlations are

normalized at the maximum amplitude and the PA is flipped in sign. The upper figure shows the PA is slightly lower than the PB at the tail but the two tails are almost parallel. The lower figure shows that the PA/ PB ratio consistently decreases with time. Both the PA and PB signals are dominated by the ground state repopulation in this case; this decreasing PA/PB ratio with time may contain the information of phonon relaxation based on our earlier hypothesis. It would be interesting to investigate this ratio over a long time scale (say >1ns) to see if the ratio reaches a constant asymptotically in the long time scale, or if the ratio decays continuously. In the case of continuous decay of the ratio, it suggests that the PA may actually die out earlier than the PB signal in the long time which consequently implies that the carrier life time at the trap state may outlive the phonon lifetime in the semiconducting SWNTs.

Much more experiments can be done on this road. For example, the temperature dependence of the PA/PB ratio is perhaps a more convincing support for the hypothesis. If we set the pump power below the point where the ratio saturates (<3 mW in figure 4.18(B)), we expect that the ratio increases with the temperature. Based on our experience, the investigation of the PA/PB ratio depends greatly on the quality of the PA signal, which consequently depends on the quality of the sample. If the signal is too noisy, the subtle variation of the ratio may not be revealed.

To summarize, two advantages (tuning excitation wavelength to resonance of the E_{11} and E_{22} states and the chirality enriched sample) allowed us to observe transient spectra of one tube species with unprecedented details. In the analysis of the transient spectra we demonstrate the interference from minority tube species to the main tube species through pump power and wavelength dependence. The resemblance between the

PA features in the spectra transients and the phonon sideband features in the PLE spectrum lead us to a new interpretation of the origin of the PA, the phonon assisted carrier scattering to the E_{11} and E_{22} states. This hypothesis helps to explain many subtleties in the transient spectroscopy, such as the variation of the cross correlation dynamics in the PB and PA regions, the narrowing of the transient spectrum with respect to the linear absorption spectrum, and the variation of the PA/PB amplitude ratio. These investigations put insights to the mechanism of the light-carrier interaction in the quasi 1D SWNT material.

To summarize the whole chapter, although numerous ultrafast spectroscopy experiments have been done in last 5 years on the SWNTs, the two fundamental issues (the excited state dynamics and the PA generation) in the pump-probe spectroscopy are still not satisfactorily understood. Our experiments presented in this chapter provide insights into these two issues: for the dynamics we propose that the probe signal is dominated by the ground state dynamics in semiconducting tube case and we propose a method to extract the excited state dynamics from the ground state dynamics; for the PA generation, we propose a new mechanism-the phonon assisted carrier scattering to the E_{11} and E_{22} states, and use it to explain some subtleties in the transient spectra. Compared with prior interpretations, our interpretation emphasizes the role of phonon-exciton interaction in the relaxation process in the system.

References:

[1] L. Huang, H. N. Pedrosa and T. D. Krauss, Phys. Rew. Lett. **93**, 017403 (2004).
[2] J. Crochet, M. Clemens and T. Hertel, J. Am. Chem. S. **129**, 8058 (2007).
[3] T. Hertel, Z. Zhu and J. Crochet et al., Phys. Stat. Sol. (b) **243**, 3186 (2006).
[4] J. S. Lauret, C. Voisin and G. Gassabois et al., Phys. Rev. Lett. **90**, 057404 (2003).
[5] O. J. Korovyanko, C. X. Sheng and Z. V. Vardeny et al., Phys. Rev. Lett. **92**, 017403 (2004).

[6] G. N. Ostojic, S. Zaric and J. Kono et al., Phys. Rev. Lett. **92**, 117402 (2004).
[7] F. Wang, G. Dukovic and L. E. Brus et al., Phys. Rev. Lett. **92**, 177401 (2004).
[8] G. N. Ostojic, S. Zaric and J. Kono et al., Phys. Rev. Lett. **94**, 097401 (2005).
[9] Y. Z. Ma, L. Valkunas and S. L. Dexheimer et al., Phys. Rev. Lett. **94**, 157402 (2005).
[10] C. Manzoni, A. Gambetta and E. Menna et al., Phys. Rev. Lett. **94**, 207401 (2005).
[11] A. Hagen, M. Steiner and M. B. Raschke et al., Phys. Rev. Lett. **95**, 197401 (2005).
[12] S. G. Chou, M. F. Decamp and J. Jiang et al., Phys. Rev. B **72**, 195415 (2005).
[13] L. Huang and T. D. Krauss, Phys. Rev. Lett. **96**, 057407 (2006).
[14] R. M. Russo, E. J. Mele and C. L. Kane et al., Phys. Rev. B **74**, 041405 (R) (2006).
[15] H. Hirori, K. Matsuda and Y. Miyauchi et al., Phys. Rev. Lett. **97**, 257401 (2006).
[16] H. Htoon, M. J. O'Connell and S. K. Doorn et al., Phys. Rev. Lett. **94**, 127403 (2005).
[17] S. G. Chou, F. Plentz and J. Jiang et al., Phys. Rev. Lett. **94**, 127402 (2005).
[18] F. Plentz, H. B. Ribeiro and A. Jorio et al., Phys. Rev. Lett. **95**, 247401 (2005).
[19] D. Toussaint, F. Wiczek, J. Chem. Phys. **78**, 2642 (1983).
[20] C. D. Spataru, S. Ismail-Beigi and R. B. Capaz et al., Phys. Rew. Lett. **95**, 247402 (2005).
[21] T. Ando, J. Phys. Soc. Jpn. **75**, 024707 (2006).
[22] H. Zhao and S. Mazumdar, Phys. Rew. Lett. **93**, 157402 (2004).
[23] S. B. Yuste and L. Acedo, Physica A 336, 334 (2004).
[24] N. Everall, T. Hahn and P. Matousek et al., Appl. Spec. **55**, 1701 (2001).
[25] D. J. Styers-Barnett, S. P. Ellison and C. Park et al., J. phys. Chem. A, **109**, 289 (2005).
[26] I. V. Rubtsov, R. M. Russo and T. Albers et al., Appl. Phys. A, **79**, 1747 (2004).
[27] R. J. Ellingson, C. Engtrakul and M. Jones et al., Phys. Rev. B, **71**, 115444 (2005).
[28] T. G. Pedersen, K.Pedersen and H. D. Cornean et al., Nano Lett. **5**, 291 (2005).
[29] M. S. Arnold, S. I. Stupp and M. C. Hersam, Nano Lett. **5**, 713 (2005).
[30] M. S. Arnold, A. A. Green and J. F. Hulvat et al., Nature **1**, 60 (2006).
[31] F. Wang, G. Dukovic and L. E. Brus et al., Science **308**, 838 (2005).
[32] J. Maultzsch, R. Pomraenke and S. Reich et al., Phys. Rew. B, **72**, 241402 (2005).
[33] (1) (A) PLE spectrum of a (6, 5) enriched sample. (B) A schematic band structure illustrating optical transitions near the E_{22} and E_{11} states. (2) Schematic of the band structure and the density of states (with arbitrary units) of the (6, 5) tube from a tight binding calculation.

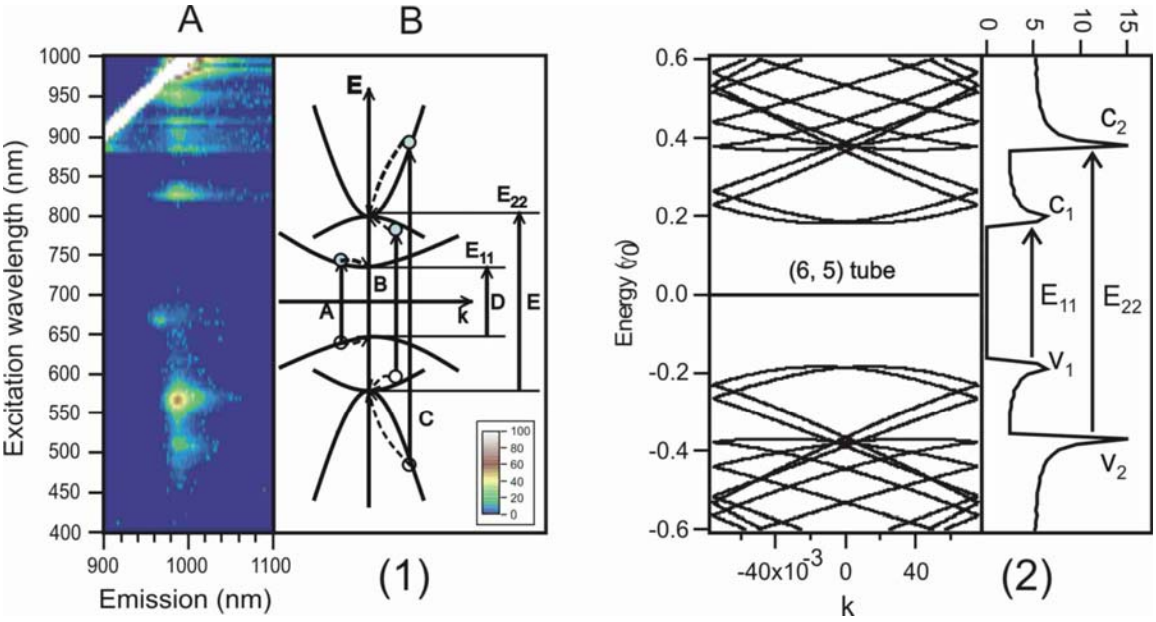

Figure r1

[34] C. D. Spataru, S. Ismail-Beigi and L. X. Benedict et al., Appl. Phys. A **78**, 1129 (2004).
[35] S. Rols, Z. Benes and E. Anglaret et al., Phys. Rev. Lett. **85**, 5222 (2000).
[36] V. Perebeinos and P. Avouris, arXiv:0804.0767v2 [cond-mat.str-el] 8 Apr 2008.

CHAPTER V

PRELIMINARY INVESTIGATION ON ULTRAFAST SPECTROSCOPY OF METALLIC SWNTS

5.1 Metallic tube ultrafast spectroscopy

Metallic SWNTs, like semiconducting SWNTs, are also an important family of carbon nanotubes and may hold promises in the future application [1]. The investigation on metallic SWNT ultrafast spectroscopy has been rare compared with that on semiconducting SWNTs, mainly due to the difficulty to separate metallic tubes from semiconducting tubes in commercially available SWNT products. Among the available reports on the pump-probe spectroscopy of metallic SWNTs, one experiment was carried out with a polydisperse sample where features from semiconducting tubes compete with those from metallic tubes [2], and another was done with a film sample containing SWNT bundles with diameters from 5 to 15 nm [3]. Great achievement on SWNT sample preparation has been made in recent years by Arnold et al., who produced bulk quantities of SWNTs of predominantly only metallic type SWNTs by using competing mixtures of surfactants [4]. In this chapter we report the first pump-probe measurements on a such-prepared metallic SWNT suspension sample. Although only a few preliminary results are obtained due to the time constraint of this study, a comparison of the spectroscopy of the metallic tube and the (6, 5) semiconducting tube shows interesting similarities and differences.

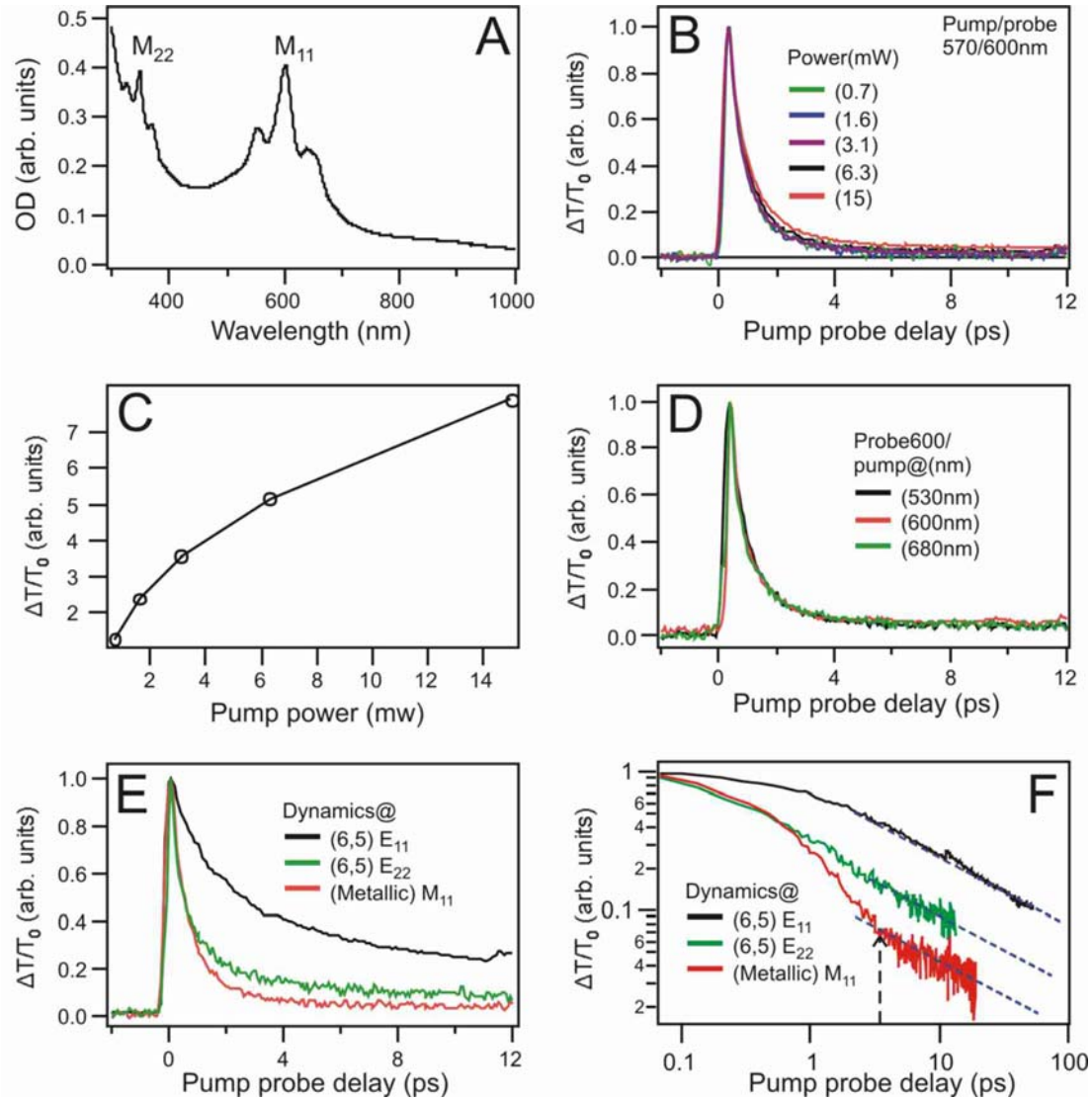

Figure 5.1 Dynamics investigation of the metallic SWNT

Figure 5.1 shows the results on the dynamics analysis with mainly cross correlation measurements. Figure (A) shows the absorption spectrum of the purified metallic SWNT sample used in the experiment. The most pronounced feature at 606 nm is denoted as M_{11}, on both sides of it are weaker features from probably two other metallic tube species. Interestingly a similar combination of absorption peak features appears around 350 nm; we temporarily assign the middle absorption peak to the M_{22} of the main

metallic tube species without verification. Compared with the (6, 5) tube absorption spectrum, the metallic tube absorption spectrum has a rapid increase of the background with energy which may be attributed to the continuous bands in metallic SWNTs.

Figure 5.1 (B) shows the pump power dependence of the dynamics with a 570 nm pump/600 nm probe scheme. The reason we did not use a degenerate 600 nm pump-probe scheme is because the signal was too noisy from degenerate measurements in this case, and based on our experience gained from the (6, 5) tube, the excited state dynamics does not change much with pump wavelength. The dynamics does not change much when the pump power is varied by roughly one order of magnitude in figure 5.1 (B). This similar trend is also observed in the (6, 5) tube case in figure 4.4 with an E_{11} degenerate pump-probe scheme.

Figure 5.1(C) shows that the maximum amplitude of the cross correlations in figure 5.1(B) increases roughly linearly with power in this pump power region. Figure 5.1(D) shows that the M_{11} state dynamics does not change much with the pump wavelength. This trend is similar to what we observed in the excitation spectroscopy of the (6, 5) tube in figure 4.5.

Figure 5.1(E) shows a comparison of the (6, 5) tube E_{11}, E_{22} and the metallic tube M_{11} probe dynamics in a shot time scale. The M_{11} trace almost overlaps with the E_{22} trace in the beginning, while it clearly decays faster than the E_{22} trace after 1ps.

Figure 5.1 (F) shows a comparison of the E_{11}, E_{22} and M_{11} probe dynamics in a logarithmic scale. The E_{22} and the M_{11} probe signals follow roughly the same dynamics from 0.1 to 0.5ps, and the M_{11} signal apparently decays faster from 0.5ps to about 5ps. Interestingly after 5 ps the M_{11} trace seems to follow the same long time dynamics as the

E_{22} and E_{11} traces, illustrated by the dashed lines of the $t^{-0.45}$ power lower fittings. The E_{11} trace is not fitted very well in this time region probably because there are still carriers on the E_{11} state around 10 ps decay time and the signal is not totally from the ground state relaxation. The same power law decays in figure 5.1(F) suggest that the ground state dynamics may be the same in metallic tubes and in semiconducting tubes, and there may also exists long lived defect induced dark states in metallic tubes. A mono-exponential fit of the beginning part of the M_{11} signal in figure 5.1(F) yields a 750 fs time constant (fitting not shown here).

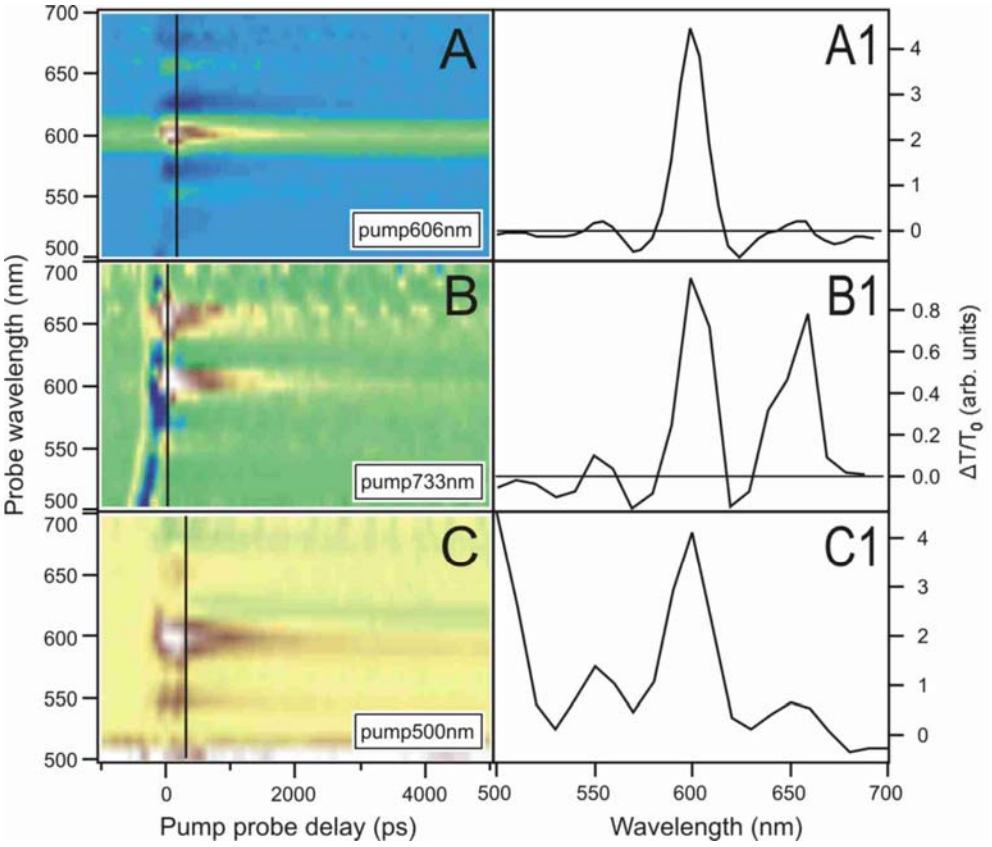

Figure 5.2 Spectra transients of the metallic SWNT sample

To study the spectral response of the metallic tube, we made some spectra transients with different excitation wavelengths, shown in figure 5.2. Figure 5.2(A) shows the spectra transients with a 606 nm pump corresponding to the M_{11} state of the main tube species. The PB features are found to correspond to the peaks in the absorption spectrum, and the PA features seem to be everywhere else. Based on our experience on the (6, 5) tube, the PA amplitude is usually much smaller than the PB amplitude for the density fractionation purified SWNT samples, we consider the strong PA on both sides of the PB at 606 nm to be mainly associated with it. The red shifted PA at M_{11} is more pronounced compared with that in the (6, 5) tube spectra transients in the E_{22} region (figure 4.13). The ratio of the main metallic peak amplitude to the minority tubes amplitudes in the absorption spectrum (figure 5.1 A) is much smaller than that of the (6, 5) tube peak amplitude to the minority tubes amplitudes (figure 4.12), which implies that the PA of the main metallic tube should be even more pronounced because they are superposed with stronger PB from minority metallic tubes. This enhancement of the PA in the metallic tube case may partly due to the considerably more density of states around the M_{11} state than around the E_{22} of the (6, 5) tube. Based on our hypothesis on the PA origin in chapter 4, because there is no density of states below the E_{11} so there is no PA below the E_{11} of the (6, 5) tube; on the other hand, because there are more density of states around the M_{11} so there may be more probabilities for carriers to reach states around the M_{11}, to interact with phonons near the M_{11}, and to be scattered to the M_{11} state, causing more pronounced PA features around the M_{11}.

Figure 5.2(A1) shows the transient spectrum at about 400 fs from a vertical cut in the map in figure 5.2(A), the PB amplitude at 600 nm should be around 3 due to the

uncorrected background scattering light. The small PA/PB ratio at the M_{11} may partly due to the relative high pump power used in the measurement.

Figure 5.2(B) shows the spectra transients with a 733 nm pump which is far below all the three PB features around 600 nm. Compared with figure 5.2(A1), the PB at 650 nm in figure 5.2(B1) is greatly enhanced while the PB at 550 nm is not, which may imply that the absorption peak at 650 nm may be broad. Yet the PA and PB positions are rough the same as they are in figure 5.2(A1).

In figure 5.2(C) the spectra transients is taken with a 500 nm pump, which is above all PB features around 600 nm. Both the PBs at 550 nm and 650 nm are enhanced and the PA around the M_{11} is not seen in the transient spectrum in figure 5.2(C1). The FWHM of the PB peak at 600 nm is broadened compared with those in figure 5.2(A1) and (B1). This also supports our hypothesis in chapter 5 about the PA origin that the PA features narrow the PB peak in the transient spectrum.

In summary, we did a brief investigation on the pump-probe spectroscopy of a purified metallic tube sample. Most observations are consistent with our observations in the spectroscopy of the semiconducting (6, 5) tube. For the dynamics, we observed a very fast initial decay with an about 750 fs time constant and a slow decay which follows the power law of $t^{-0.45}$ after 5 ps. For the transient spectra, we observed the PA feature at both sides of the M_{11} state. By varying the excitation wavelength in the spectra transients, we observed a clear trend of the superposition effect of the PA and PB signals and the broadening of the PB due to the vanishing of the PA.

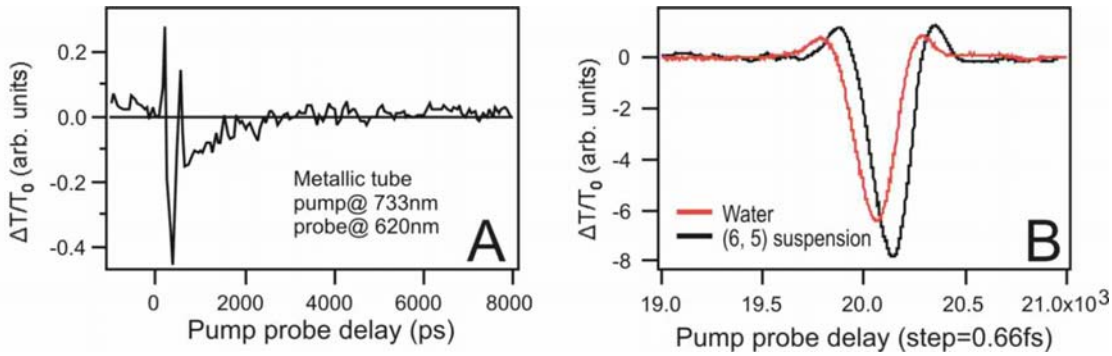

Figure 5.3 Noises in the cross correlation signals from coherent effect.

The signal quality of the pump-probe cross correlations is important for the dynamics and transient spectrum analyses, especially for the investigation on the subtleties of the PA/PB ratio discussed in section 4.2.6. In this last section, we like to point out a tricky thing that may affect the pump-probe signals.

Figure 5.3(A) is a cross correlation taken from the spectra transients in figure 5.2(A) of the metallic tube sample, which shows a strong spike before a weak PA signal. The spike comes from a coherent effect and is not associated with the SWNTs. The spike happens at almost every probe wavelength in the spectra transients in figure 5.2(A) that results in a vertical stripe of PA near time zero in the spectra transients. When the signal from the SWNTs is strong, this spike is not pronounced and not PA stripe is seen in figure 5.2(A). The overlap of the spike with the PA signal alters the PA amplitude of the SWNTs near time zero.

If we optimize the amplitude of the spike by adjusting the pump and probe beam overlap, we may get rid of the PA signal from the SWNTs and only keep the spike. In figure 5.3(B), the spikes obtained from a (6, 5) tube suspension and pure water have the

same behavior, which shows that the spike is not associated with SWNTs. The width of the spike is about 500 steps of the delay stage, equivalent to 300 fs. This implies that the cross correlations in the beginning 300 fs may be affected by this coherent effect especially when the signal from SWNTs is weak. The way to avoid this artifact is to shift the pump beam focus slightly away from the probe beam focus, in doing so we avoid this artifact by compromising the signal strength from SWNTs. But when the signal from SWNTs is too weak and we can not compromise much, this artifact gets pronounced.

Reference:

[1] P. G. Collins and P. Avouris, Scientific American, p62-69, December 2000.
[2] R. J. Ellingson, C. Engtrakul and M. Jones et al., Phys. Rev. B **71**, 115444 (2005).
[3] Y. Hashimoto, Y. Murakami and S. Maruyama et al., Phys. Rev. B **75**, 245708 (2007).
[4] M. S. Arnold, A. A. Green and J. F. Hulvat et al., Nature **1**, 60 (2006).

CHAPTER VI

SUMMARY

This study has been focused on the ultrafast spectroscopy of SWNTs, especially the (6, 5) semiconducting SWNT. The many new observations and analyses achieved in this intensive investigation contribute to a better understanding of the special spectroscopic properties of these extraordinary quasi 1D materials.

Due to the intrinsic connection between the ultrafast spectroscopy signal of SWNTs and their electronic and physical structures, it is necessary to understand the fundamental physical and electronic structures of SWNTs in order to better understand their complicated behavior in the ultrafast spectroscopy. In chapter 2, we discussed the physical structure of SWNTs and illustrated the SWNTs band structure with a simple tight binding approximation (TBA) calculation, which serves as a foundation of the more current theories of the electronic structure of SWNTs that favor the exciton picture with an emphasis on the dark exciton states. The fundamental and most current theories on the SWNT electronic structures provide us a foundation with which our ultrafast spectroscopy is explained.

The understanding of the function of the instrumentation of the experiment is also important in order to obtain correct and reasonable high quality signals. Noisy signals or false interpretation of the signals may lead to misunderstanding of the SWNT ultrafast spectroscopy. In chapter 3, we introduced the configuration of our ultrafast laser system, and discussed in detail the function of the two components (RegA and Vitesse) in the

system. We also discussed the density fractionation purification method used to obtain highly purified SWNT samples, which played a key role in eliminating the signal interference from minority tubes to the main tube species in the ultrafast spectroscopy.

The most important component in the laser system is the OPA, although none of other components is dispensable. This is because we vary the excitation wavelength continuously in making the pump-probe excitation spectroscopy. Also in chapter 3, we discuss in detail the principle and function of the OPA, and the method we upgraded it to tune wavelength automatically. The upgraded OPA becomes a power tool in studying the complicated excited state dynamics of SWNTs.

The main part of this dissertation – the pump-probe spectroscopy of the (6, 5) semiconducting SWNT, is presented in chapter 4. We focused on two fundamental aspects in the spectroscopy: the excited state dynamics and the transient spectrum. In the dynamics investigation, the pump power and wavelength dependences suggest that the amplitude of the cross correlations does not reflect the excited state dynamics as expected, and the probe signal relaxation is dominated by the ground state recovery. Thanks to the high quality of our cross correlation signals, we were able to distinguish the small difference between the E_{11} and E_{22} probe kinetics with the E_{11} excitation and consequently, extracted the E_{11} state dynamics by subtracting the E_{22} probe kinetics from E_{11} probe kinetics. In the transient spectrum investigation, we first verified the interference between signals of different tube species by pump power dependence and pump wavelength dependence, in which we paid attention to the PB FWHM and the PA position and the PA/PB amplitude ratio associated with the (6, 5) tube. Then we compared the spectra transients obtained with the E_{11} and E_{22} excitation and the PLE map

of the (6, 5) tube sample, and found that the PA features in the spectra transients and the phonon sideband features in the PLE map are in reasonable good agreement, which prompted us for a new hypothesis for the origin of the PA – the phonon assisted carrier scattering to the E_{ii} states. Finally we used the hypothesis to interpret some subtleties in the pump-probe transient spectrum, including the spectrum narrowing effect and PA/PB ratio variation.

We briefly investigated the ultrafast spectroscopy of a purified metallic SWNT sample in chapter 5, and showed some interesting similarities and differences between the spectroscopy of the metallic SWNTs and that of the (6, 5) semiconducting SWNTs. On the exited state dynamics we observed a very fast initial relaxation in the metallic SWNTs followed by a weak power law decay. On the transient spectrum, we observed that the PAs were on both sides of the PB from the same metallic tube species. We also pointed out an important artifact in the pump-probe signals that may interfere with the true signal from SWNTs.

In summary, based on the observations from an intensive investigation of the pump-probe spectroscopy of the highly purified (6, 5) chirality enriched SWNT samples, we proposed new interpretations for the two essential issues in the SWNT ultrafast spectroscopy, i.e., the long time dynamics of the probe signal follows a power law decay and the real excited state dynamics is contained in the beginning part of the signal, and the PA features may due to phonon assisted carrier scattering to the E_{ii} states. We also investigated the pump-probe spectroscopy of a highly purified metallic tube sample, which provides useful information for further studies on the metallic SWNTs.

CONCLUSION

We recapitulate what might be the contributions we made in this study to the research field.

First, the method to upgrade the OPA to automatic wavelength tuning is a useful piece of information to those who want to upgrade their existing OPA and to do pump-probe excitation spectroscopy. From our observation, although there have been a lot of experiments on the pump-probe spectroscopy of SWNTs in the last five years, the pump-probe excitation spectroscopy has basically not been done before. The excitation spectroscopy is very important in studying the dynamics, and the result of our SWNT excitation spectroscopy is used as a solid support for our interpretation of the excited state dynamics. The apparent lack of excitation spectroscopy investigation may partly due to the inconvenience of tuning the OPA wavelength manually. The upgrading method introduced in this dissertation may help other spectroscopists to upgrade their OPA.

Second, we conclude in the SWNT pump-probe spectroscopy, the cross correlation signal can be roughly decomposed to a short dynamics that monitors the excited state relaxation and a long time dynamics that monitors the relaxation of some long lived trap states. Depending on the speed of the initial relaxation compared to the power law decay of $t^{-0.45}$, the short time dynamics can be very pronounced in the metallic tube case or very hidden in the (6, 5) semiconducting tube case. Much more experiments are needed to unveil the mystery of the carrier relaxation channels and optical dark states in SWNTs, but the concept achieved here that the excited state dynamics and the ground state dynamics may not be the same and the probe signal is always more or less affected by the

ground state recovery is important in examining the excited state dynamics in the SWNTs as well as in other materials.

Third, we proposed a new mechanism for the origin of the PA feature in the SWNT transient spectrum – phonon assisted carrier scattering to the E_{ii} states, based on the similarities of the PA features in the spectra transients and the phonon sideband features in the PLE map. This mechanism is strongly supported by the current belief that the sideband features in the PLE map are mostly phonon assisted, and it helps to explain a lot of subtle but important observations in the transient spectrum. This hypothesis opens a window to a potential wealth of information about the carrier phonon interaction and its influence to the excited state relaxation process in the SWNT pump-probe spectroscopy.